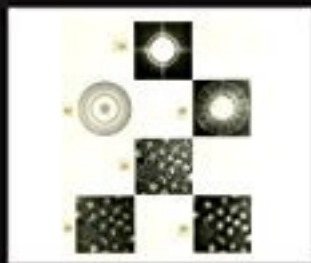# Advances in
IMAGING and ELECTRON PHYSICS

Volume 191

EDITED BY
PETER W. HAWKES

Femtosecond Electron Imaging and Spectroscopy

Proceedings of the Conference on Femtosecond Electron Imaging and Spectroscopy, FEIS 2013, December 9–12, 2013, Key West, FL, USA

Martin Berz, Philip M. Duxbury, Kyoko Makino[1], Chong-Yu Ruan
Michigan State University, East Lansing MI 48824, USA
[1]Corresponding author: e-mail address: makino@msu.edu

1. INTRODUCTION

We are witnessing tremendous opportunities in ultrafast sciences with the development of extremely bright radiation sources to investigate the structure and spectroscopy of matter with atomistic space and femtosecond time resolution. While generally a strong focus has been on X–ray sources—notably free electron laser (FEL) sources—the use of femtosecond electron pulses has also shown enormous promise in the last decade, especially in the investigation of materials from the sub-micrometer down to the angstrom scale, facilitated by the high sensitivity of electron scattering and the relative ease in designing electron optics for imaging and diffraction from nanomaterials. Moreover, important innovations have been achieved by incorporating ultrafast photoemission sources into various electron microscope setups. Most recently, a new trend of integrating the FEL high-brightness electron beam concept into the ultrafast electron diffraction and microscope system design is likely to open up new prospects and applications of femtosecond diffraction, imaging, and spectroscopy with high throughput.

The conference on Femtosecond Electron Imaging and Spectroscopy (FEIS 2013) was held on December 9–12, 2013 in Key West, Florida. FEIS 2013 built on the potential synergy between related technology developments and various emerging scientific opportunities and brought together

leaders engaged in cutting-edge development of high-brightness electron and X-ray beam systems and their applications to frontier science problems. FEIS 2013, the first in this series, was organized with the goal of initiating conversation between different communities with the following objectives in mind: (1) to review the current state-of-the-art development and open issues of ultrafast electron imaging technologies; (2) to discuss emerging scientific opportunities enabled by ultrafast imaging and spectroscopy; (3) to identify the key technical challenges in the design and applications of ultrafast electron imaging systems; and (4) to forge cross-fertilization between the electron microscopy, accelerator and beam physics, and ultrafast communities, and to have experimentalists and theorists address common challenges and promote synergistic developments.

1.1 Synopsis of FEIS 2013

1.1.1 Current Status of Ultrafast Imaging and Spectroscopy

Functional imaging and spectroscopy at the local level with atomic, electronic, and magnetic sensitivity are highly desirable for understanding structure-property relationships at the nanometer-length scale and in complex materials. Y. Zhu (page 26) presented an overview of the broad scientific opportunities accessible by utilizing high-energy electrons, including atomic imaging, quantitative electron diffraction, energy-loss spectroscopy, and Lorentz and in situ microscopy, with an emphasis on understanding the materials' functionality through correlative studies. A community that incorporates electronic, magnetic, thermal, and optical excitations into conventional high-resolution electron microscopes for in situ imaging and spectroscopy studies is rapidly developing. In particular, optical excitations can now routinely be employed on the femtosecond timescale, presenting an opportunity for unique photonic control and potentially imaging at high temporal resolution. Ultrafast electron imaging and spectroscopy represents a natural next step of modern electron microscope development.

To form a diffraction pattern or image, typically 10^5 to 10^7 electrons are required. In time-resolved electron microscopy, diffraction, and spectroscopy systems, the electron sources are triggered by pulsed lasers, so the electron beams are delivered in discrete bunches, rather than a steady, diluted stream. So-called space charge effects emerge due to the strong electron-electron interaction within a single photoelectron bunch, which may manifest itself in different forms (i.e., virtual cathode, defocusing, and stochastic blur, as discussed later). Several active technologies cleverly circumvent space charge effects and have achieved significant improvements in temporal

resolution using electron microscopy, diffraction, and spectroscopy. G. H. Campbell (page 15) presented the dynamic transmission electron microscope (DTEM) project at Lawrence Livermore National Laboratory using the single-shot approach. By initiating intense photoelectron pulses using a 10-ns laser, the average distance between electrons, even at the 10^8 electron per pulse level, is more than $100\,\mu$m apart, suffering nearly no space charge effect except at the acceleration stage and near the focal plane. Single-shot imaging of microstructure formation, including the kinetics of nucleation and phase transitions in semiconductors, phase change materials, and intermetallic compounds at combined $\sim$10 ns–10 nm spatiotemporal resolution, have been achieved using the DTEM.

In contrast, by operating at a high repetition rate ($\sim$100 MHz), as presented by S. T. Park (page 21), near-single-electron-pulse ultrafast electron microscopes (UEMs) developed at California Institute of Technology are used to study highly reproducible site-specific events, such as dynamical modes of nanomechanical systems and surface plasmons. The fs single-electron pulses, initiated on a LaB_6 filament, are fully compatible with the existing electron optical system in a TEM, largely preserving its high spatial resolution and achieving in practical implementations an impressive sub-ps-nm resolution in a stroboscopic setup, where hundreds of thousands or more diffraction data sets are collected at each delay time. The concurrence of ultrashort electron probing and fs laser excitation also enables a new modality of imaging, termed photon–induced near field electron microscopy (PINEM), that has been used to map the optically driven charge density distribution of nanoparticle plasmons. The mechanism and implications of such studies were discussed by S. T. Park's and in the talk by B. Barwick's (page 14). Both approaches are operated by modifying a conventional 100–200 keV TEM, maintaining the capability to retrieve local information.

So far, the most widely employed fs imaging protocol is the diffraction mode. This ultrafast electron diffraction (UED) method initiated the field of electron-based ultrafast imaging; it was introduced in the 1990s first in gas-phase studies of chemical reactions and nonequilibrium molecular dynamics, not long after the development of the largely optical spectroscopy–based fs-chemistry. The timely development of single-electron-sensitive CCDs equipped with pixilated electron amplification and Ti-Sapphire amplified laser systems helped to make robust UED systems available for a range of relatively routine applications. There were, however, earlier efforts in time-resolved electron diffraction and microscopy using nanosecond laser systems. The history of these earlier and ongoing developments of

time-resolved diffraction and microscopy has recently been reviewed (Ischenko & Aseyev, 2014). In striving to move from stroboscopic UED to single-shot UED for studying irreversible processes, R. J. D. Miller's group pioneered the short source-to-sample diffractometer configuration to overcome excessive space charge effects. The associated development in characterizing short electron pulses and many impressive recent applications can be found in a review article (Sciaini & Miller, 2011).

A more recent update on fs electron diffraction was presented by M. Hada (page 19), who used single-shot electron diffraction to show the photo-induced cold ablation process of alkali halide crystals through electronically induced disorder, which leads to the ejection of materials at optical energy densities below the threshold for melting of the alkali halide crystals.

C. Gerbig (page 18) presented another short distance design where the sample was buried within the electron lens where very high temporal resolution ($\sim$150 fs) was recorded through the characterization of the coherent acoustic modes in few layer graphite samples. J. Cao (page 16) presented work studying the coherent acoustic modes in metal films driven by impulsive electronic heating, in a scenario where a magnetic coupling into the spin dynamics can be examined by tracking the transient electronic heat capacity using the UED approach. F. Carbone (page 17) presented a discussion of photonic tuning in combination with ultrafast microscopy, diffraction, and EELS to address specific questions about complex solids.

Another approach to mitigate the space charge effect in single shot UED or UEM is to operate at MeV energy ranges using RF guns where the relativistic time-dilation freezes out the electron-electron interaction. X. J. Wang (page 25) reported the latest progress of a BNL 2.8-MeV relativistic UED system in delivering $\sim$10^5 e within a single $\sim$200-fs electron bunch, sufficient to form diffraction patterns capturing atomic scale processes at subpicosecond timescales. Alternatively, S. Sakabe (page 23) discussed an intense fs laser-accelerated electron source as a viable beamline for single-shot electron diffraction. N. Matlis (page 20) described laser-plasma electron accelerators as emerging tools for ultrafast science, including the possibility of providing tunable electron sources (from MeV to GeV), X-ray sources (UV to keV) and THz radiation that are intrinsically synchronized to the drive laser system. Another intriguing realization of electron imaging utilizes the electronic coherence in the nonlinear photoemission process. Also operated at near the single-electron emission limit at a high repetition rate, H. Petek (page 22) recorded movies of surface plasmon-polariton propagation with 50-nm spatial and 330-attosecond temporal

resolution by utilizing the interferometric effect in the two-photon photo-emission process. Related ultrafast photoemission spectroscopy developments (see N. Gedik, page 30, and M. Murnane, page 31) use higher-energy photons or X-rays and emphasize momentum and spectroscopic resolution to probe the electron dynamics in solids.

1.1.2 Emerging Opportunities

Nonequilibrium quantum dynamics and control of phase transitions via optical tuning in complex materials are emerging areas discussed in FEIS 2013. Moreover, correlated electron materials have been considered as alternative electronic materials beyond semiconductors. Due to fundamentally different governing mechanisms, phase transitions in correlated electron materials are frequently strongly first order and highly sensitive to temperature, pressure, or charge carrier doping effects. All of these control parameters may be tuned by selective photoexcitation. The significant progress in the last few years on laser- and X-ray-based time-resolved photoemission spectroscopy to directly inspect the quantum dynamics of the electronic degrees of freedom has stimulated significant interest in the condensed matter physics and materials communities. This development is highly synergistic to ultrafast electron-based imaging and spectroscopy. In particular, the control side of ultrafast pump-probe technologies is especially relevant in the discussion of the possible selection of modes, new states or macroscopic orders directly induced via ultrafast photonic tuning. Along these lines, N. Gedik (page 30) discussed the first observation of Floquet–Bloch states in a topological insulator initiated by mid-infrared circularly polarized pulses that were tuned to be below the optical gap of a topological insulator, observed by angle-resolved photoemission.

M. Murnane (page 31) reported on the latest progress in generation of coherent X-ray pulses using high harmonic methods, enabling study of electron dynamics in molecules, quantum dots, and solids with higher momentum resolution than laser-based photoemission methods. Combining electron spectroscopy and diffraction, L. Piazza (page 35) described results of correlated structural and electronic dynamics in manganite, probed by ultrafast diffraction and EELS, suggesting structural and electronic changes induced by tuning of lattice strain induced by a fs laser-induced pressure wave. Z. Tao (page 38) reported on mapping the charge and structural orders during the metal–insulator transition of VO_2 and of TaS_2 using UED with temperature and photonic tuning. The prospects of high-fidelity high-turn around characterization of 2D electronic crystals using

microbeam electron diffraction in a high-brightness beam setup were discussed. Utilizing the high surface sensitivity of low-energy electrons, S. Schweda (page 37) reported on studies of polymer superstructures on graphene surfaces in an ultrafast low-energy electron diffraction (LEED) setup. A. Paarmann (page 33) presented another fs LEED setup with photoemission triggered on a nanotip and accelerated to 50–1000 eV. The setup was employed to investigate the transient electric field and charge distribution in photoexcited nanostructures based on point-projection imaging.

The multimodality of electron imaging and spectroscopy may effectively decode the intertwined correlations between different degrees of freedom, which are a hallmark of correlated electron materials. S. Ramanathan (page 36) outlined the opportunities for controlling the ultrafast phase transition in correlated oxides for advanced electronics. On the theory side, description of the ultrafast response of complex materials requires methods to calculate the nonequilibrium quantum dynamics of correlated systems. To provide a solid basis for understanding of physical processes, and as a check on computational methods for correlated systems, J. K. Freericks (page 29) and T. P. Devereaux (page 28) introduced models without electronic correlations to capture phenomena such as transient photoemission response, transient melting of a CDW, and generation of a transient topological insulator in graphene. K. Nasu (page 32) examined subtle relaxation processes of collective optical excitation of valence electrons into an empty conduction band that show two time regions (avalanching and critical slowdown) mediated by electron–electron and electron–phonon interactions. K. Nasu also discussed the nature of long-lived electronic excitations.

1.1.3 High-Brightness Technologies for the Next Generation Ultrafast Electron Microscopes

The development of the next generation ultrafast electron imaging and spectroscopy technologies to implement true multimodality (diffraction, microscopy, and spectroscopy) with ultrafast time-resolution requires a significant boost of the six-dimensional (6D) beam brightness. Improvement in transverse beam brightness (4D brightness) from the employment of the field emission gun (FEG) has led to progress in pushing aberration-corrected and monochromatic TEM resolution into the sub-angstrom range, with sub-100-meV energy resolution. Unlike in high-brilliance X-ray generation, which drives the success of FEL, the Fermionic nature of electrons prevents the packing of electrons beyond the Pauli limit. Nonetheless, the required electron beam brightness is still orders of magnitude away from this

fundamental limit (Portman et al., 2013). Therefore, the current UEM and UED spatiotemporal-energy resolutions are largely limited by practical limitations, particularly the inability to achieve full control of the dynamical phase space to optimize the performance for either the diffraction, microscopy, or spectroscopy mode of operation. FEIS 2013 examined the conditions for high-brightness beam generation and various technologies for preserving the initial brightness and control of the beam optical properties for realizing the next-generation, high-brightness UEMs.

P. Musumeci (page 44) presented an overview of high-brightness beam science, as well as cases of diffraction and microscopy employing pancake and cigar beam aspect ratio photoelectron bunches initiated in an MeV RF gun. J. Yang (page 45) presented the first implementation of an RF gun-based MeV UEM. Using a pancake beam delivered to the sample at $\sim$100 fs and transverse emittance of 0.2 mm–mrad, as well as an energy spread of 10^{-4}, an excellent quality of diffraction pattern can be acquired with 10^6 electrons in a single shot. Images can be acquired with a magnification of 3000. However, the electron dose at the samples was diluted due to strong defocusing and only the stroboscopic mode is feasible at the present time. J. Frisch (page 42) discussed various protocols for implementing laser/RF synchronization, which is currently the limiting factor for achieving pulsewidth-limited temporal resolution. Despite the fact that very short electron pulses have been generated ($<$100 fs), robust pump-probe studies are now limited to several hundred fs due to shot-to-shot instability that can be traced to the phase noise between the laser and RF signals.

A phase drift in the RF gun (or cavity) can lead to a change in acceleration field, varying the arrival time of the electron pulse at the sample. V. Dolgashev (page 40) discussed high-fidelity electron pulse characterization using X-band RF deflectors, with a temporal resolution of the order of 10 fs. D. Filippetto (page 41) presented a MHz repetition rate RF gun (APEX) operating at $\sim$1 MeV for high-flux UED experiments. The APEX system differs from conventional RF guns in its higher repetition rate (the repetition rate in conventional RF guns is typically less than 1 kHz), which yields a high average current despite a lower charge density ($\sim$10^6 per pulse). Such a system has a better time resolution ($<$100 fs) and less emittance, well suited for UED experiments that do not require a large number of electrons. R. Li (page 43) discussed a feasibility study of a single-shot ps TEM with a nm spatial resolution currently in the planning stage. The microscope will employ cigar aspect ratio photoelectron initiation to generate a 1–pC ($\sim$6 × 10^8 electrons) charge with nm transverse emittance,

in combination with RF curvature regulation using an additional RF cavity downstream to compensate the energy spread induced in the long cigar pulse by the RF gun.

1.1.4 Beam Dynamics and Optics

The fundamental challenge in designing any high-brightness beam system for femtosecond electron imaging and spectroscopy is the proper treatment of the space charge effects. Whereas the collective effects, such as virtual cathode and beam defocusing, may be mitigated by employing high-gradient photoguns and refocusing optics, such as RF compressors, the stochastic effect, which leads to irreversible emittance growth, fundamentally limits the resolution. Without going to great numerical details, H. Rose (page 52) outlined the fundamental limitations of resolution in UEMs caused by Coulomb interaction on an analytical basis. Since the stochastic interaction becomes more significant at lower energies, a relativistic beam energy is preferred, although focusing a high-energy beam is significantly more challenging. Meanwhile, from the imaging contrast point of view, for imaging thin amorphous objects, it is more efficient to use low-energy beams due to the larger fraction of scattered electrons. Dark field imaging with subrelativistic electrons using hollow-cone illumination with an annular aperture or cathode was proposed as an alternative.

Current common practice to compress the space charge dominated beam is to employ an RF cavity, which unavoidably is limited by the precision of laser/RF synchronization. W. Wan (page 55) presented another approach to bunch compression using electrostatic or magnetic fields in an achromatic beam transport line, completely avoiding RF jitter issues. R. Janzen (page 48) presented intriguing approaches to perform energy compression of beams without filtering based on intricate arrangements of circular deflection due to circularly polarized fields in a cavity.

B. W. Reed (page 51) examined the physical laws that govern space charge effects, stochastic blur, and electron-sample interactions, and characterized the performance in practical DTEM, UED, and UEM using the brightness in 6D phase space as a unifying concept. E. Kieft (page 50) presented simulation data for two aspects of operation in the first commercialized UEM, operating in "stroboscopic" or "single-shot" mode. From a practical perspective, it was found that the highest brightness is not always the best solution for pulsed imaging.

Depending on the applications, matched electron sources and other beam parameters (emittance, applicable pulsed numbers) are all integral parts

of the design which may be guided by simulation. To this end, M. Berz (page 47) presented a unified framework to determine high-order spatio-temporal aberrations under the presence of nonlinear space charge by combining differential algebra (DA)–based fast multipole methods (FMMs) for the treatment of space charge with the conventional DA-based computation of high-order transfer maps. H. Zhang, Z. Tao, C.-Y. Ruan, and M. Berz (page 56) discuss the DA–based FMM approach in dealing with space charge effects for arbitrary arrangements of charges independent of computational grids. Building on the rapid decrease of space charge forces with distance, the influence of faraway particles is combined into multipoles instead of treating particles directly, where the regions that can be combined increase with distance. Combining with local expansion techniques, it is possible to achieve a computational cost that is linear in the number of particles. The method was used to examine the key space charge dominated behavior, which is central to the design of high-brightness beam formation, such as virtual cathode formation, and onsets of turbulent and laminar flow under different photoemission conditions (acceleration field and surface charge distribution), leading to emittance growth.

1.1.5 Synergistic Development and Further Discussion

F. E. Merrill (page 116) presented a planned multi-GeV beam facility at Los Alamos National Laboratory for studies of materials and radiation in the extremes. The goal is to measure fast dynamic material properties with spatial resolution of less than 1 µm and temporal resolution of less than 1 ps. D. J. Flannigan (page 81) discussed practical technical considerations limiting the combination of ultrafast spectroscopy and imaging capabilities in a UEM besides the intrinsic space charge limit. The environmental and specimen stability are central, especially when stroboscopic ultrafast images with multiple time sequences may take longer to acquire, where it is necessary to deconvolute inevitable artifacts from the intrinsic dynamics. W.-X. Tang (page 131) presented an ultrafast spin–polarized low-energy electron microscope (LEEM) based on a commercially designed spin-polarized LEEM. The objective is to study low-dimensional spin dynamics and ultrafast surface dynamics. O. J. Luiten (page 115) presented a new class of electron sources based on photoionization of laser-cooled, trapped rubidium atoms. By optical tuning at near-threshold and polarization effects, the photoionized electrons from a low-temperature source may carry a high level coherence to form ps-coherent beams for nano-diffraction.

Emerging opportunities for studying the structural dynamics of liquid and gaseous systems were described. Major advances in direct structural studies of solvation dynamics and solvent-solute interaction using optical pump and X-ray probe at synchrotron facilities, were presented by H. Ihee (page 96). Similar strategies may be incorporated into ultrafast electron beamlines through liquid jets, in situ stages, or full environmental microscopes. D.-S. Yang (page 132) presented initial results from an ultrafast environment scanning electron microscope (SEM), where a subtle photo-assisted secondary electron emission yield can be used to track the local potential and the solvation dynamics at a surface. Benefiting from the rapid development of MEMS technology that has recently made liquid encapsulated TEM environmental cells feasible, N. D. Browning (page 68) presented work and prospects of direct imaging of oxidation and reduction in metals, ceramics, and catalytic systems including imaging of nucleation and growth mechanisms of nanostructures in solution.

These proceedings also include several invited papers that examine in further detail some of the open questions from the conference. R. F. Egerton, T. Konstantinova, and Y. Zhu (page 70) elaborate on R. F. Egerton's FEIS 2013 presentation and look into the radiation effects induced by X-ray and electron beams, with an emphasis on organic materials. For such radiation-sensitive specimens, radiation damage imposes a more severe limit, known as the *dose-limited resolution*. It is intriguing to note that the damage dose for electrons with a resolution of 1 nm, sufficient for imaging large biological molecules, is at $\sim 10^7$ Gray or $1 - 10 \, \mathrm{e \, nm}^{-2}$, which is within reach if the target time resolution is set at 1 ps, as demonstrated by recent source-limited performance calculations (see J. Portman et al., page 117). Further improvement in time resolution may come through improving the source brightness through techniques such as laser pulse shaping or tuning of the driving photons to threshold energy from a high-efficiency cathode; and it may make ps-macromolecular imaging feasible without the need to outrun the radiation damage effects, as required in the case of imaging using X-rays.

In considering the proper energy scale, C. Limborg-Deprey et al. (page 98) report an X-band photoelectron RF gun operated at a very high-gradient field (200 MeV/m), to deliver extremely high-peak brightness. Such a high-performance MeV scale system may deliver ultrashort pulses (down to 25 fs) or high-bunch charges (up to 100 pC), or can be optimized for low emittance beams. Due to the strong knock-on effects associated with high-energy beams, MeV UED or UEM systems are better suited

to the study of inorganic materials. In contrast, the lower-energy beam delivered by DC guns at the 100-keV level may deliver stable, tightly focused, or monochromatic beams at the expense of achieving a high dose sufficient for fs single-shot imaging. In particular, meV-scale ultrafast electron spectroscopy may be possible for lower-energy beams.

J. Portman et al. (page 117) in further quantitative detail address the source-limited performance of ultrafast electron imaging and spectroscopy systems under various acceleration fields and photoelectron pulse aspect ratios (namely, the so-called pancake and cigar scenarios). The simulation results point to the interesting finding that a ps cigar beam indeed excels in coherence length—up to 20 nm with 10^4 electrons and $\sim$1 nm with 10^8 electrons—however, the high-acceleration field also increases its energy spread, whereas the energy spread of cigar-shaped beams is quite unaffected. Overall, the fs pancake beam has significantly smaller longitudinal emittance (ε_z) up to the virtual cathode limit, and is more suited for high combined temporal-spectral resolution UEDs, whereas the cigar beam may be suited for ps imaging, close to the single-shot limit.

J. K. Freericks, K. Najafi, A. F. Kemper, and T. P. Devereaux (page 83) describe methods to check the validity of large-scale computational methods that are essential in the study of the nonequilibrium quantum dynamics of electron systems that are correlated to the lattice degrees of freedom. Non-equilibrium identities, or sum rules, for an important model system (the Holstein model) are derived, and exact results are presented for the atomic limit.

1.2 Summary

The conference provided a fruitful exchange of ideas. It seemed clear at the end of the conference that significant improvement of the currently active DTEM, UEM, and UED systems is on the horizon, through the various mechanisms of increasing source brightness and incorporating static or dynamic pulse compression schemes to correct the space charge led to a defocusing effect, as proposed by many different groups. An emerging consensus is that different fs imaging and spectroscopy systems may be developed to target different scientific questions, requiring the choice of beam energy, flux, and spatial, temporal, and spectral resolution as appropriate for the physical processes under consideration. See the *DOE Report of the Basic Energy Sciences Workshop on Future of Electron Scattering and Diffraction*

(2014), cochaired by E. Hall, S. Stemmer, H. Zheng, and Y. Zhu. *February 25–26, 2014 in Rockville, Maryland.*

Driven by the natural synergy between the electron microscopy, ultrafast laser, X-ray and accelerator communities, the momentum promoted by FEIS 2013 continues to grow, and a second FEIS conference is scheduled to take place in Michigan in May 2015. The conference series will then move on to Eindhoven, the Netherlands in 2016 and China in 2017.

REFERENCES

Ischenko, A. A., & Aseyev, S. A., Eds. (2014). Time-resolved electron diffraction for chemistry, biology and materials science. Vol. 184 of *Advances in imaging and electron physics.* Amsterdam: Elsevier.

Portman, J., Zhang, H., Tao, Z., Makino, K., Berz, M., Duxbury, P. M., & Ruan, C.-Y. (2013). Computational and experimental characterization of high-brightness beams for femtosecond electron imaging and spectroscopy. *Applied Physics Letters, 103*, 253115.

Sciaini, G., & Miller, R. J. D. (2011). Femtosecond electron diffraction: Heralding the era of atomically resolved dynamics. *Reports on Progress in Physics, 74*, 096101.

Current Status of Ultrafast Imaging and Spectroscopy

Imaging at the nm and fs Scales with Ultrafast Electron Microscopy (UEM)

B. Barwick
Trinity College, Connecticut, USA

Investigating ultrafast phenomena with femtosecond $(10^{-15}\,\text{s})$ and attosecond $(10^{-18}\,\text{s})$ temporal resolution is pivotal to understanding the dynamic processes that atomic, molecular and condensed matter systems undergo. The timescale for dynamics, at the atomic length scale, ranges from picoseconds to attoseconds for processes such as the heating of a thin metallic crystal and the motion of plasmons in metals. In this talk, I will describe ultrafast imaging using single–electron packets as applied to several different nanoscale ultrafast processes. In particular, I will describe a new imaging method that exploits the fact that free electrons (when near a third body) can absorb and emit multiple photons. The physics describing the absorption and emission of photon quanta by free electrons is well known in AMO physics as a free-free transition and is manifested in the laser–assisted photo-emission effect. We form images by using only electrons that have absorbed photons; allowing us to observe the evanescent electric field created by plasmons that have been excited by an intense ultrafast optical pulse. In describing this imaging technique, dubbed *photon-induced near-field electron microscopy (PINEM),* I will also discuss future plans to extend the temporal resolution to tens of femtoseconds, and possibly even the attosecond regime.

Quantitative Measures of Phase Transformation Kinetics with the Dynamic Transmission Electron Microscope

G.H. Campbell, T. LaGrange, B.W. Reed, M.K. Santala, J.T. McKeown
Lawrence Livermore National Laboratory, California, USA

Time-resolved transmission electron microscopy in situ observations of phase transformations in materials gives unique quantitative insights into the operative physics and kinetics of transformation process. We have developed a single-shot instrument (see the companion presentation by Bryan Reed) that allows us to observe the details of individual transformation events with temporal resolution as short as 15 ns and spatial resolution better than 10 nm. We have applied the technique to studies of rapid solidification in aluminum alloys, in which the speed of the liquid/solid interface and the composition of the alloy have strong effects on microstructure formation in the alloy system. We have also studied phase change materials to measure nucleation rates in nucleation–dominated systems such as $Ge_2Sb_2Te_5$ and to measure the growth rate in growth–dominated systems such as GeTe. These measurements have been made with high accuracy in the regimes that these materials are actually used in their technological applications. Similarly, we have studied the complicated growth morphology of explosively crystallized Ge. Finally, we will show results from the intermixing of pure Al and pure Ni across interfaces and the rate of intermetallic phase formation. All of these studies are based on measurements that are possible by no other technique than the dynamic transmission electron microscope (DTEM).

Ultrafast Structure Dynamics in Metal Films

J. Cao
Florida State University, Florida, USA

Ultrafast electron diffraction is a rapid–advancing technique capable of revealing the atomic–detail structural dynamics in real time. Over the past few years, this technique has been used to revolve structure dynamics in a variety of systems, such as phase transitions in physics and materials science and reactions in chemistry and biology. In this talk, I will focus on its application in probing ultrafast structure dynamics in metal films. The topics will cover the mechanism of coherent phonon generation under the non-equilibrium condition and ultrafast photo–induced demagnetization in ferromagnetic materials.

Time-Domain Observation of Coherent Phenomena in Solids and Nano Structures

F. Carbone
École Polytechnique Fédérale de Lausanne, Lausanne, Switzerland

Recent advances in ultrafast technology allow both the study and the control of material's properties thanks to the ability to record high temporal resolution movies of their transformations, or the ability to generate new states of matter by selecting ad hoc the excitation that drives a system out of equilibrium. The holy grail of this type of experiments is to combine a high tuneability of the excitation with a wide observation window. In solids, information on the structural degrees of freedom can be obtained in a very direct way via diffraction, while the accompanying dynamics of the electronic structure can be followed by fs optics (at $q=0$), electron energy loss spectroscopy (as a function of momentum q), or photoemission (also a momentum-resolved probe, but capable of accessing the very-low-energy states close to the Fermi level). In addition, modern time-resolved microscopy also delivers information about the real space morphology of the materials as well as the spatial distribution of charge and spin patterns and domains. In this seminar, we will review the way in which a combination of these tools is used in our laboratory (LUMES, Laboratory for Ultrafast Microscopy and Electron Scattering, at the EPFL) to address specific questions about high-temperature superconductivity, order–disorder transitions, and charge/orbital ordering phenomena in solids.

Resolution Studies on a Compact Femtosecond Transmission Electron Diffractometer and Phonon Decay in Single Crystalline Graphite

C. Gerbig, S. Morgenstern, C. Sarpe, A. Senftleben, M. Wollenhaupt, T. Baumert
Universität Kassel, Institute of Physics and Center for Interdisciplinary Nanostructure Science and Technology (CINSaT), Kassel, Germany

Time-resolved diffraction, using X-ray or electron probes, has become a promising technique to directly provide insights into dynamics at the molecular level with ultrafast precision (Chergui & Zewail, 2009, Sciaini & Miller, 2011). We study dynamical processes in single crystalline graphite by means of ultrafast electron diffraction in order to expand the understanding of phonon generation and decay mechanisms being essential for future carbon based electronic devices (Kampfrath et al., 2005; Schäfer et al., 2011). Our highly compact DC electron diffractometer is fully characterized by experiments and N-body simulations. The temporal profile of electron pulses is determined by grating enhanced ponderomotive scattering (Sciaini & Miller, 2011) at multiple charge densities. Spatial resolution and diffraction efficiency analyses are performed for selected electron source sizes. We demonstrate electron pulse durations below 150 fs and a transversal coherence length above 20 nm. At balanced conditions, a temporal resolution of 200 fs, along with high-definition diffraction, is achieved for dynamical studies on graphite single crystals in a maintainable measurement time (Gerbig et al., 2014). We further present generation and decay processes of incoherent as well as coherent phonons in graphite as a function of film thickness down to few-layer graphene (Gerbig et al., 2015).

REFERENCES

Chergui, M., & Zewail, A. H. (2009). Electron and x-ray methods of ultrafast structural dynamics: Advances and applications. *ChemPhysChem, 10*, 28–43.

Gerbig, C., Senftleben, A., Morgenstern, S., Sarpe, C., & Baumert, T. (2014). Submitted.

Gerbig, C., Senftleben, A., Morgenstern, S., Sarpe, C., & Baumert, T. (2015). In preparation.

Kampfrath, T., Perfetti, L., Schapper, F., Frischkorn, C., & Wolf, M. (2005). Strongly coupled optical phonons in the ultrafast dynamics of the electronic energy and current relaxation in graphite. *Physical Review Letters, 95*, 187403.

Schäfer, S., Liang, W., & Zewail, A. H. (2011). Primary structural dynamics in graphite. *New Journal of Physics, 13*, 063030.

Sciaini, G., & Miller, R. J. D. (2011). Femtosecond electron diffraction: Heralding the era of atomically resolved dynamics. *Reports on Progress in Physics, 74*, 096101.

Cold Ablation Driven By Localized Forces: A Femtosecond Electron Diffraction Study

M. Hada, R.J.D. Miller
Max Planck Institute for the Structure and Dynamics of Matter, Hamburg, Germany

We will present some results obtained with newly developed femtosecond electron diffraction (FED) setups at Max Planck Institute for the Structure and Dynamics of Matter, Hamburg. The first FED study involves the structural evolution of alkali halide crystals under fs–ultraviolet–laser excitation. Single-shot time-resolved FED, optical reflectivity, and ion detection experiments were applied to study the evolution of the ablation process that follows photoexcitation in crystalline NaCl, CsI, and KI. The results reveal fast optical and structural changes associated with the development of disordering and electronic stress that would lead to ejection of material (large clusters, fragments, or both) and the formation of micron-deep craters. We found evidence for a cold ablation explosion that occurs well below the threshold for plasma formation and the melting point of alkali halides, reflecting the very nature of electron correlations lying right at the onset of the Pauli repulsion well. The second study focuses on the photo-induced structural dynamics associated to charge transfer processes in a large-unit-cell quasi–two–dimensional strongly correlated materials. The development of FED setups has reached the point where structural studies of protein dynamics are possible.

Compact Laser-Plasma Accelerators for Ultrafast Electrons, X-rays and THz

N. Matlis, J. van Tilborg, G.R. Plateau, A.J. Gonsalves, S.V. Steinke, C.G.R. Geddes, C.B. Schroeder, E. Esarey, C. Toth, B. Shaw, S. Shiraishi, W.P. Leemans
Lawrence Berkeley National Laboratory, California, USA

Laser–plasma electron accelerators (LPAs) are emerging as promising tools for ultrafast science due to their ability to simultaneously produce in a compact format a plurality of ultrashort radiation sources, including electrons (from MeV to GeV), X-rays (UV to keV) and THz radiation that are intrinsically synchronized to the drive laser system. This diversity of well-timed radiation sources offers new possibilities in ultrafast imaging and probing in a format that is accessible to a wide range of studies. State-of-the-art research in LPAs is aimed at improving control and stability of the accelerator performance to enhance their viability for applications. We discuss generation of electrons, X-rays, and THz radiation from an LPA system and present recent results in using control of electron-injection in LPAs to improve the energy spread and stability of the accelerator. Electron pulses with percent-level energy spread in the 200–300-MeV energy range from a 2-mm accelerator using a sub-10-TW laser are demonstrated. We also introduce a new method for single-shot tomographic imaging that is ideally suited to ultrafast pump-probe experiments using multiple radiation modalities (in particular, broadband betatron X-rays) and demonstrate its use in the measurement of density profiles of multiple-filament plasma targets.

Plasmon Charge Density Probed by Ultrafast Electron Microscopy

S.T. Park, A.H. Zewail
California Institute of Technology, California, USA

Ultrafast electron microscopy in space and time domain utilizes an electron pulse to directly probe structural dynamics of nanomaterial, initiated by an optical pump pulse, in imaging, diffraction, spectroscopy, and their combinations. It has demonstrated its capability in the studies of phase transition, mechanical vibration, and chemical reaction. Moreover, electrons can directly interact with photons via near–field components of light scattering by nanostructure and either gain or lose light quanta discretely in energy. By energetically selecting those electrons that exchanged photon energies, one can image the photon–electron interaction and is termed *photon-induced near field electron microscopy (PINEM).* Here, we reexamine the physical meaning of the electron–photon interaction and show that the PINEM image directly maps the optically driven charge density distribution of nanoparticle plasmons. This insight is applied to various nanostructures, and the nature of their plasmon modes is discussed.

Ultrafast Photoemission Electron Microscopy: Imaging Nonlinear Plasmonic Phenomena on the Femto/Nano Scale

H. Petek
University of Pittsburgh, Pennsylvania, USA

Light interacting with a metal surface can excite both single-particle (e-h pair) and collective (plasmon) excitations. By angle-resolved photoemission spectroscopy and photoemission electron microscopy, we investigate the coherent ultrafast dynamical processes in interaction of light with silver metal surfaces. We employ the two photon photoemission process to image plasmonic phenomena in Ag metal films. By means of interferometric time-resolved photoemission electron microscopy (ITR-PEEM), we can create spatial maps of two-photon photoemission excited in nanostructured Ag films. We fabricate specific nanoscale structures for the coupling of surface plasmon polaritons (SPPs), the electromagnetic modes of a metal/dielectric interface, and we image their effect on the coupling, propagation, interference, and focusing of SPP waves. By advancing the delay between identical and collinear pump and probe pulses with interferometric precision, we are able to record movies of SPP wave propagation, and nonlinear interactions with 50 nm of spatial resolution and 330 attoseconds/frame temporal precision. Based on simple theoretical models, we discuss the imaging process, the optics of SPP wave packets, and the prospects of ultrafast microscopy of plasmonic phenomena.

Intense Femtosecond Laser Accelerated Electron Pulses for Single-Shot Ultrafast Electron Diffraction and Electron Deflectometry

S. Sakabe, M. Hashida, S. Tokita, S. Inoue
Institute for Chemical Research, Kyoto University, Uji, Kyoto, Japan

To observe ultrafast changes of atomic-scale structure in matters and electromagnetic fields near matters during phenomena, time-resolved electron diffraction and electron deflectometry using femtosecond electron pulses are useful, respectively. The key issue to realize single-shot ultrafast electron diffraction (UED) or electron deflectometry is to develop intense, short electron–pulse sources. With conventional UED instruments, an electron pulse is generated at a photocathode irradiated by a femtosecond laser pulse and accelerated in an additional external static electric field. The amount of electrons in the pulse is limited because the electron pulse expands during its flight by space-charge forces in the pulse. Electrons accelerated by intense femtosecond laser pulses have potential for intense electron pulse sources. It is featured by pulse, point source, rather broad momentum, unnecessity of external accelerators, and perfect synchronization with other radiation (X-ray, ions, white light, THz, etc.) generated by the same laser pulse. We have been studying the physics of electron emission during and after laser–plasma interaction to develop higher-intensity electron pulses. Using the characteristics of broad momentum, we have demonstrated femtosecond pulse compression of a laser-accelerated electron beam with energy of around 350 keV (Tokita et al., 2009, 2010). The electron pulses are generated by irradiating a tightly focused terawatt femtosecond laser pulse on a polyethylene foil target; then, the pulse is compressed with an achromatic bending magnet system. It has been demonstrated to take a single-shot diffraction pattern using these femtosecond electron pulses. For an aluminum foil target, many more electrons are emitted than for the polyethylene foil target, but the electrons are emitted along the target surface while in the laser direction for the polyethylene foil target. Using these characteristics, it has been demonstrated to guide electrons along a metal wire target, resulting in directional emission with several tens higher intensity than metal foil target. To observe the electric fields near the laser plasma produced by the

interaction of intense femtosecond laser pulse with a solid target, we have made the electron deflectometry using laser accelerated electron pulses with an electron lens (Inoue et al., 2010, 2011, 2012). Using femtosecond electron deflectometry with electron pulses accelerated by intense laser pulses mentioned previously, it has been successfully demonstrated to observe the electromagnetic surface (Sommerfeld) wave propagating along a metal wire irradiated by an intense femtosecond laser pulse (Tokita et al., 2011; Nakajima et al., 2013).

REFERENCES

Inoue, S., Tokita, S., Nishoji, T., Masuno, S., Otani, K., Hashida, M., & Sakabe, S. (2010). Single-shot microscopic electron imaging of intense femtosecond laser-produced plasmas. *Review of Scientific Instruments, 81*, 123302.

Inoue, S., Tokita, S., Otani, K., Hashida, M., Hata, M., Sakagami, H., et al. (2012). Auto-correlation measurement of fast electron pulses emitted through the interaction of femtosecond laser pulses with a solid target. *Physical Review Letters, 109*, 185001.

Inoue, S., Tokita, S., Otani, K., Hashida, M., & Sakabe, S. (2011). Femtosecond electron deflectometry for measuring transient fields generated by laser-accelerated fast electrons. *Applied Physics Letters, 99*, 031501.

Nakajima, H., Tokita, S., Inoue, S., Hashida, M., & Sakabe, S. (2013). Divergence-free transport of laser-produced fast electrons along a meter-long wire target. *Physical Review Letters, 110*, 155001.

Tokita, S., Hashida, M., Inoue, S., Nishoji, T., Otani, K., & Sakabe, S. (2010). Single-shot femtosecond electron diffraction with laser-accelerated electrons: Experimental demonstration of electron pulse compression. *Physical Review Letters, 105*, 215004.

Tokita, S., Inoue, S., Masuno, S., Hashida, M., & Sakabe, S. (2009). Single-shot ultrafast electron diffraction with a laser-accelerated sub-MeV electron pulse. *Applied Physics Letters, 95*, 111911.

Tokita, S., Otani, K., Nishoji, T., Inoue, S., Hashida, M., & Sakabe, S. (2011). Collimated fast electron emission from long wires irradiated by intense femtosecond laser pulses. *Physical Review Letters, 106*, 255001.

MeV Electron Beam for Ultrafast Electron Diffraction and Imaging

X.J. Wang
Brookhaven National Laboratory, New York, USA

In recent years, we have witnessed tremendous progress in our understanding of the ultrafast and ultrasmall world, thanks to the X-ray free electron laser (XFEL). The development of photoelectron sources directly led to the success of XFEL; at the same time, such high-brightness electron sources could also open the door to the next generation of electron scattering instrumentation: MeV ultrafast electron diffraction (UED) and ultrafast electron imaging (UEM) (Wang et al., 2003). MeV UED and UEM not only have the potential of higher temporal resolution (Wang et al., 1996), but also has a larger scattering signal and less sample damage. After a brief review of the history of MeV UED and UEM, I will discuss the latest developments and technical challenges in MeV UED and UEM. I will also discuss the potential scientific opportunities enabled by MeV UED and UEM.

REFERENCES

Wang, X. J., Qiu, X., & Ben-Zvi, I. (1996). Experimental observation of high-brightness microbunching in a photocathode RF electron gun. *Physical Review E, 54R*, 3121–3124.

Wang, X. J., Wu, Z., & Ihee, H. (2003), Femto-seconds electron beam diffraction using photocathode RF gun. In *Proceedings of 2003 Particle Accelerator Conference: Vol. 1* (pp. 420–422). Portland, Oregon, USA: IEEE. May 12–16, 2003.

Probing Materials Behavior Using Ultrafast Electrons

Y. Zhu
Brookhaven National Laboratory, New York, USA

In this presentation, I will give a brief overview of the frontiers of electron microscopy, including atomic imaging, quantitative electron diffraction, energy-loss spectroscopy, off-axis electron holography, and in situ microscopy in order to understand materials functionalities. Examples of various probing methods will be given to reveal the behavior of electrons, spins, orbitals and lattice and their correlations. The advantages and drawbacks of the methods and their limitation on spatial and time resolution will be deliberated. Challenges and future opportunities for electron scattering will be discussed.
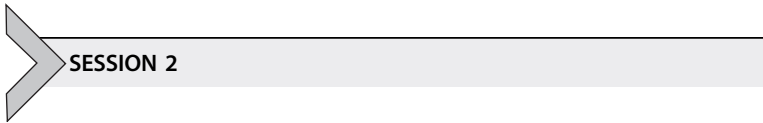
Emerging Opportunities

Theoretical Understanding of Ultrafast Electron Dynamics in Model Systems

T.P. Devereaux
SLAC National Accelerator Laboratory/Stanford University, California, USA

In this talk, I present the results from three separate model systems for pump–probe spectroscopy with the goal of understanding a language for non-equilibrium, driven electronic systems. Specifically, I will discuss results for pump–probe photoemission across a metal–insulator transition, a coupled electron–lattice system, and driven graphene in an effort to generate a non-equilibrium topological insulator.

Exact Theoretical Description of Pump/Probe Experiments in Charge Density Wave Insulators

J.K. Freericks
Georgetown University, Washington D.C., USA

In this talk, I will describe a range of different theoretical results for the simplest model of a charge-density-wave insulator, which can be solved exactly in nonequilibrium. I will look at the behavior of the "nonequilibrium melting" of a CDW as seen in time-resolved photoemission spectroscopy experiments. I will examine the behavior of quantum excitation and how it changes from frequency driven to amplitude driven. Finally, I will examine the behavior of high harmonic generation from the solid state. I will discuss how these results compare with those from different experiments, where available, and will also describe what kinds of experiments are interesting to examine in the future. As theoretical treatments of nonequilibrium phenomena develop, we will be able to help understand current experiments and propose new ones.

Observation of Floquet-Bloch States in Topological Insulators

N. Gedik
Massachusetts Institute of Technology, Massachusetts, USA

The topological insulator (TI) is a new phase of matter that exhibits quantum–Hall–like properties, even in the absence of an external magnetic field. Understanding and characterizing unique properties of these materials can lead to many novel applications, such as current induced magnetization or extremely robust quantum memory bits. In this talk, I will discuss recent experiments in which we used novel time and angle-resolved photoemission spectroscopy (ARPES) to directly probe and control properties of Dirac fermions. The unique electronic properties of the surface electrons in a topological insulator are protected by time–reversal symmetry. Breaking such symmetry without the presence of any magnetic ordering may lead to an exotic surface quantum Hall state without Landau levels. Circularly polarized light naturally breaks time-reversal symmetry, but achieving coherent coupling with the surface states is challenging because optical dipole transitions generally dominate. Using time- and angle-resolved photoemission spectroscopy, we show that an intense, ultrashort, mid-infrared pulse with energy below the bulk band gap hybridizes with the surface Dirac fermions of a topological insulator to form Floquet-Bloch bands. The photon-dressed surface band structure is composed of a manifold of Dirac cones evenly spaced by the photon energy and exhibits polarization–dependent band gaps at the avoided crossings of the Dirac cones. Circularly polarized photons induce an additional gap at the Dirac point, which is a signature of broken time-reversal symmetry on the surface. These observations establish the Floquet-Bloch bands in solids experimentally and pave the way for optical manipulation of topological quantum states of matter.

Probing Electron Dynamics in Molecules, Quantum Dots and Materials at the Space-Time Limits Using Coherent Tabletop High-Harmonic X-Rays

M. Murnane

University of Colorado Boulder, Colorado, USA

Advances in extreme nonlinear optics now make it possible to efficiently upshift femtosecond lasers into the ultraviolet (EUV) and soft X-ray regions of the spectrum, to wavelengths as short as 8 Å. In an optimized geometry, the resultant high harmonics (HHG) emerge as fully spatially coherent beams, with ultrabroad bandwidths supporting few-fs to attosecond pulses. This unique light source is ideally suited for capturing and controlling all dynamics relevant to function, from the attosecond timescales characteristic of electrons, to fs timescales characteristic of vibrations and dissociation, to ps timescales characteristic of rotations in molecules. Applications of tabletop ultrafast laser and X-ray sources in materials, molecular, and nanosystems will be presented. In recent work, we performed the first photoelectron spectroscopy of quantum dots in the gas phase and extracted how far the evanescent electron wavefunction extends from different-sized dots. This is a key property in understanding electronic coupling of nanoscale systems to their environment. We also probed the fastest phase transitions and spin transport in materials using ultrafast HHG X-rays. Finally, we implemented the first reflection-mode, full-field, tabletop, coherent diffraction X-ray microscope.

How Much Time Is Necessary to Photogenerate Fermi Surfaces from a True Electron Vacuum?

K. Nasu
Institute of Material Structure Science (IMSS), High Energy Accelerator Research Organization (KEK), Tsukuba, Japan

Rapid relaxation dynamics of optically excited electrons in metallic systems has already been widely investigated. In most cases, however, only a few electrons are optically excited, while the main part of electrons is still in the ground state and works as an infinite heat reservoir, resulting in quite rapid relaxation of newly given energy and momentum.

What occurs if a macroscopic number of electrons are excited into a truly vacant conduction band without an electronic heat reservoir at absolute zero? Two successive laser pulse excitations of GaAs, and subsequent time-resolved photoemission spectrum measurement on the conduction band electrons by Kanazaki–Tanimura can partly answer this very simple, but ultimate photo-induced phase transition problem.

Coulombic inter-electron scatterings within the conduction band, being completely elastic, can give no net energy relaxation. Meanwhile, the phonon relaxation, according to the Luttinger theorem, becomes infinitely slow as the system approaches the complete Fermi degeneracy; hence, it never terminates.

Femtosecond Low-Energy Diffraction and Imaging

A. Paarmann, M. Müller, S. Lüneburg, R. Ernstorfer
Fritz-Haber-Institut der Max-Planck-Gesellschaft, Berlin, Germany

The recent development of femtosecond electron and X-ray diffraction and imaging techniques allows for the direct observation of structural dynamics in the course of photo-induced chemical or physical processes with atomic spatial and femtosecond temporal resolution. Photo-induced structural dynamics are governed by the interplay of electronic and nuclear degrees of freedom, which depend on the dimensionality of the system. While so far these techniques have been predominantly applied to crystalline samples, we aim for the investigation of ultrafast dynamics in low-dimensional systems, such as two-dimensional materials, surfaces, and nanostructures, which ask for a time-resolved technique with a maximal scattering cross section. Expanding ultrafast electron diffraction to low electron energies in the sub-kV range will combine femtosecond temporal resolution with high surface sensitivity. We developed a novel setup for femtosecond low-energy electron diffraction (fsLEED) and imaging in the energy range of 50–1000 eV based on a laser-triggered metal nanotip. Owing to the confined emission area due to field enhancement, nanotips are nearly ideal point sources delivering highly coherent ultrashort electron pulses. Besides using single electron pulses at high repetition rates to eliminate space charge effects, femtosecond time resolution is achieved by using a compact geometry with sub-mm propagation distances, which minimizes dispersive temporal broadening of the electron wave packets (Paarmann et al., 2012). The instrument is designed for two operation modes: (i) point-projection imaging and (ii) fsLEED, the latter either in transmission or reflection geometry. Time-resolved point projection microscopy utilizes the high sensitivity of low-energy electrons to weak electric fields, in order to map transient electric fields and charge distributions in photoexcited nanostructures. Specifically, we investigate charge carrier separation upon above-bandgap excitation in axially doped InP nanowires. This experiment provides a unique possibility to directly image ultrafast currents with nanometer resolution. The diffraction studies, on the other hand, require a collimated electron beam. In order to maintain the short propagation distances in fsLEED

experiments, we developed a compact microlens coated directly onto the shaft of the nanotip to collimate the intrinsically divergent electron beam without any optics between tip and sample (Lüneburg et al., 2013). We first present experimental data on transmission LEED of free-standing monolayer graphene using our compact approach.

REFERENCES

Lüneburg, S., Müller, M., Paarmann, A., & Ernstorfer, R. (2013). Microelectrode for energy and current control of nanotip field electron emitters. *Applied Physics Letters, 103*, 213506.

Paarmann, A., Gulde, M., Müller, M., Schäfer, S., Schweda, S., Maiti, M., et al. (2012). Coherent femtosecond low-energy single-electron pulses for time-resolved diffraction and imaging: A numerical study. *Journal of Applied Physics, 112*, 113109.

Ultrafast Structural and Electronic Dynamics of the Metallic Phase in a Layered Manganite

L. Piazza, C. Ma, H. Yang, A. Mann, J. Li, F. Carbone
Laboratory for Ultrafast Microscopy and Electron Scattering, Institute of Condensed Matter Physics (ICMP), Lausanne, Switzerland

The transition between different states in manganites can be driven by various external parameters. Controlling these transitions with light opens the possibility to investigate the microscopic path through which they evolve. We performed femtosecond transmission electron microscopy on a bi–layered manganite to study its response to ultrafast photoexcitation. We show that a photo–induced temperature jump launches a pressure wave that provokes coherent oscillations of the lattice parameters, detected via ultrafast electron diffraction. Their impact on the electronic structure are monitored via broadband ultrafast electron energy loss spectroscopy (EELS), revealing the dynamics of the different orbitals in response to specific structural distortions.

Ultrafast Phase Transitions in Correlated Oxides and Electronics

S. Ramanathan
Harvard University, Massachusetts, USA

I will discuss our ongoing efforts in understanding metal–insulator transitions in correlated oxides in the rutile and perovksite structures (e.g., VO_2 and $SmNiO_3$, respectively). The transition can be in ps-ns timescales depending on the triggering mechanism. Scientific questions pertain to the nature of the transition mechanism (i.e., electronic versus structural), and whether the components can be decoupled during actuation. There are a few ways to study this problem from a device physics perspective that I will elaborate on in the presentation—namely, two- and three-terminal devices that allow dynamic modulation of conductivity, gating the resistance without introducing joule heating. Complexities arise in interpretation that is due to our limited understanding of the nature of electrically active defects at the correlated oxide interfaces. I will give representative examples of high-performance solid state devices that we have realized with such ultrafast phase transitions. Finally, I will point out some open questions in the field that could be worth visiting in a collaborative setting with this group of researchers.

Polymer Superstructure Dynamics on Graphene Probed by Ultrafast Low-Energy Electron Diffraction

S. Schweda, M. Gulde, M. Maiti, S. Schäfer, C. Ropers
IV. Physical Institute, University of Göttingen, Göttingen, Germany

Atomic-scale microscopy and diffraction techniques with high temporal resolution are of particular interest for the understanding of fundamental transient phenomena such as structural reorganizations and phase transitions. Past years have shown a substantial development in the time-resolved analysis of bulk media utilizing ultrashort X-ray or electron probes. However, the time-resolved investigation of structural dynamics at surfaces remains challenging, despite recent accomplishments (e.g., in ultrafast reflection high-energy electron diffraction). Implementing low-energy electron diffraction (LEED) with ultrafast temporal resolution in an optical pump/electron probe scheme is a natural approach to observing surface structures due to the high surface sensitivity of slow electrons. So far, ultrafast LEED (ULEED) has not been demonstrated owing to technical difficulties in realizing suitable pulsed low-energy electron sources. In particular, in this regime, electron pulses are very sensitive to spatiotemporal broadening due to Coulomb repulsion and velocity dispersion. In this contribution, we present the implementation of ULEED based on a nanometric photocathode, achieving a temporal resolution of few picoseconds. The setup allows us to investigate the structural dynamics of an ultrathin bilayer consisting of an ordered polymethylmethacrylate (PMMA) layer on free-standing, single-layer graphene. Specifically, we temporally resolve the ultrafast melting of a stripe-like PMMA superstructure and the formation of a disordered expanded phase. Our experiments illustrate the potential of time-resolved, low-energy electron diffraction as a powerful tool to study ultrafast atomic-scale phenomena at surfaces.

Ultrafast Metal-Insulator and Charge-Ordering Transitions in Correlated Transition Metal Compounds

Z. Tao[1], T.-R.T. Han[1], K. Chang[1], F. Zhou[1], J. Portman[1], K. Wang[2], J. Wu[2], C.D. Malliakas[3], M.G. Kanatzidis[3], D. Torres[1], N. Sepulveda[1], S.D. Mahanti[1], P.M. Duxbury[1], C.-Y. Ruan[1]

[1]Michigan State University, Michigan, USA
[2]University of California, Berkeley, California, USA
[3]Northwestern University, Illinois, USA

Competitions between lattice, spin, and charge-ordered states in correlated transition metal compounds can lead to phase transitions that are highly tunable by applying heat, temperature, electrical, and optical excitations. These attributes are ideal for constructing electronic and photonic devices promising ultrafast high-fidelity switching with less energy than the conventional semiconductor-based devices. Nonetheless, the successful implementation of these devices is hindered by our current lack of understanding in key phase transition mechanisms under strong electron–electron correlation and electron–phonon coupling. Here, using optical reflectivity, TEM, and ultrafast electron crystallography, we investigate vanadium dioxide (VO_2) and tantalum disulfide ($1T-TaS_2$), which are two prototypical correlated electron systems exhibiting strongly first-order metal-insulator transitions due to subtle interplay between the underlying Mott and Peierls physics. In the VO_2 case, we find that for single-crystal nanobeams gently placed on substrates the structural and metal-insulator transitions can be tuned from cooperative to non-cooperative conditions by simply changing the substrates from insulating to metallic. In contrast, for polycrystalline thin film influenced by the inter-domain strain fields, the phase transitions are often cooperative at steady states, but exhibit stepwise atomic movements and strong anisotropic lattice responses under ultrafast perturbations. These clear-cut nonequilibrium features can be attributed to the competitive Mott and Peierls physics in directing the phase transitions. In the $1T-TaS_2$ case, the relevant Mott and Peierls-driven processes are displayed in the distinct charge-ordering and domain dynamics revealed at the ultrafast timescales. We will describe the various collective state switching phenomena from both the steady-state and ultrafast perspectives, and discuss the prospects of advancing such studies with the development of an RF-enabled UEM system at MSU.

High-Brightness Technologies for the Next Generation Ultrafast Electron Microscopes

X-Band Deflectors for Femtosecond Diagnostics of Electron Beams

V. Dolgashev
SLAC National Accelerator Laboratory, California, USA

Modern tendency to study ultrafast physical process has led to experimental methods and devices that utilize extremely short, subpicosecond electron bunches. Examples of such devices are X-ray free electron lasers, RF guns for relativistic electron diffraction, and advanced-accelerator test facilities. Electron energy in such devices varies for a few MeV in RF-electron guns to 20 GeV in SLAC's Facility for Advanced Accelerator Experimental Tests (FACET). Optimization and control of the longitudinal distribution of bunch parameters require diagnostics that have temporal resolution in the order of 10 fs. This presentation is a review of practical implementations of such diagnostics based on X-band deflecting cavities and waveguides.

High-Flux Ultrafast Electron Diffraction Development

D. Filippetto, W. Wan
Lawrence Berkeley National Laboratory, California, USA

The APEX gun is a high-brightness, high-repetition rate electron source under commissioning at LBNL. It delivers MeV electron pulses at a MHz repetition rate, with the transverse brightness needed for driving an FEL. We are investigating the possibility to build a side beamline for high-flux UED experiments. The first simulations show that sub-100-fs beams with 10^6 particles per bunch and nanometer emittance are achievable. Jitter characterization is underway, with the goal to minimize energy, pointing and time jitters, and the final goal of pump-to-probe time jitters below 100 fs. Possible proof of principle experiments are being investigated, which will be performed within the next year.

Laser RF Synchronization

J. Frisch

SLAC National Accelerator Laboratory, California, USA

Studies of ultrafast phenomena require synchronization of electron beams and experiment lasers at the subpicosecond level. Similar synchronization is required for photocathode drive lasers relative to the RF fields in electron guns. Synchronization is frequently performed by using RF techniques to measure the relative phase of the mode-locked laser oscillator and the RF reference that is used to drive the accelerator, and then feeding back on the phase of the laser oscillator. It is also possible to measure the relative timing with electro–optical techniques, or to treat the laser source as the master oscillator and lock the accelerator RF phase. We discuss the design and engineering issues involved in these locking systems.

Single-Shot Picosecond Temporal Resolution Transmission Electron Microscopy

R. Li, P. Musumeci
University of California, Los Angeles, California, USA

An active research area to further enhance the capability of state–of–the–art transmission electron microscopies is to dramatically improve their temporal resolving power, which will enable us to visualize in real time many ultrafast dynamic processes in biology, chemistry, and material science. Progress in this direction critically depends on the generation, precise control and advanced diagnosis of electron beams with unprecedented brightness, including ultrasmall emittance, ultralow–energy spread, and high–beam current. Here, we present the feasibility study of a single–shot ultrafast transmission electron microscopy using high–brightness electron beams from a high–gradient photocathode radio–frequency electron gun aiming at a few picoseconds temporal resolution and a few tens of nanometers spatial resolution. We will discuss several key technical innovations optimized to address the challenging demand on beam quality, including the generation of pico–Coulomb charge ultralow–emittance beam in the cigar–aspect–ratio regime, the RF curvature regulation technique to greatly reduce the beam energy spread, and strong electron optics using permanent quadrupole magnets or nano–fabricated microquadrupoles. Effects of collective space charge forces and stochastic Coulomb scattering on the achievable spatial resolution will also be discussed.

High-Brightness Beam Science

P. Musumeci
University of California, Los Angeles, California, USA

In this talk, I will review recent results in the physics of high-brightness electron beams with relevance to the generation of ultrafast electron scattering probes. Starting with a definition of brightness bridging the accelerator and microscopy community, I'll discuss the different regimes of pancake and cigar beam aspect ratio and show how they respond to the different requirements of ultrafast electron diffraction and time resolved microscopy. The roles of the cathode photoemission properties and injection electric field will be clarified. I will then talk in detail about one particular kind of high-brightness electron source, the RF photoinjector, and how it enabled the application of MeV electron beams to ultrafast electron diffraction. To conclude, I'll present an overview of our recent efforts to improve the instrument and expand its capabilities to include imaging mode.

RF Gun–based MeV Transmission Electron Microscope

J. Yang
Osaka University, Osaka, Japan

The first prototype of RF gun–based relativistic-energy electron microscopy has been constructed at Osaka University to study ultrafast structural dynamic processes in matter. The RF gun, driven by a femtosecond laser, has generated a 100-fs-pulse MeV electron beam with emittance of 0.2 mm-mrad and energy spread of 10^{-4}. Both the electron diffraction and image measurements have been succeeded in the prototype using the femtosecond electron beam. In the diffraction measurement, an excellent quality of diffraction pattern was acquired, with an electron number of 10^6. The single-shot measurement is available in the prototype. In the image measurement, the TEM image was acquired with a total electron number of 10^8. The magnification was 3000 times. In the next step, we will reduce further the emittance to increase the beam brightness on the sample, and then improve the spatial resolution to less than 10 nm.
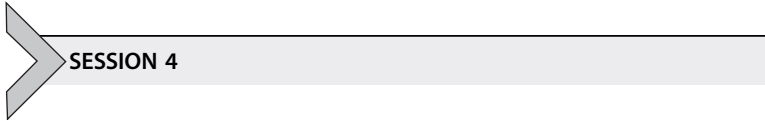
Beam Dynamics and Optics

High-Order Spatiotemporal Aberrations Under Presence of Space Charge

M. Berz, K. Makino
Michigan State University, Michigan, USA

We review modern differential algebraic (DA) methods for the computation of high-order aberrations of electron microscopes, and extend these to systems with time dependent accelerating fields. Since the aberrations are driven by high-order derivatives of on-axis or midplane fields, care has to be taken when the fields arise from numerical computations or measurements. In this case, they are best described by data on a closed surface via the Helmholtz theorem, which leads to infinitely often differentiable and fully Maxwellian fields, thus preserving all Hamiltonian invariants of the motion, and that are furthermore smoothed if measurement or computational errors are present.

The methods are then combined with special versions of the fast multipole method (FMM) for efficient computation of space charge effects. In the collisionless setting with smoothing by suitable wavelets, the results of the additional nonlinearities arising from space charge are thus combined with the ones due to external fields in a natural way. As a result, DA based, high-order, time stepping schemes originally developed for the computations of aberrations alone are seamlessly enhanced to incorporate space charge fields as well. In terms of the conventional FMM methods, this provides an additional enhancement that goes beyond their acclaimed $O(N)$ behavior resulting from local multipole expansions of the fields, even providing flow expansions in time and thus resulting in more efficient particle pushing.

Monochromatizing Without Filtering Using Dynamic Fields Without Bunching—A New Concept for D-TEM Illumination

R. Janzen

Johannes Gutenberg Universität Mainz, Mainz, Germany

Commonly used monochromators are energy filters. The majority of the particles with undesired energies is removed. Thus, the output current diminishes with increasing monochromatization rate. Monochromators in the original meaning of the word that would affect the energy of the particles by an energy selective acceleration can be realized only by the use of dynamic fields. All dynamic field applications, without exception, involve a condition between the phase of the dynamic field and the entrance point of time of the particle into the field. If this condition is fulfilled, the dynamic field application works exactly. Unfortunately, the width of the time interval where the condition is fulfilled is mathematically zero. Thus, up to now, dynamic field applications in charged particle optics limit themselves to a small time interval around the periodically recurring point of optimum phase, where the condition is fulfilled to a good approximation.

For that purpose, bunches are formed around the optimum phase point. Unfortunately, bunch forming suffers from Liouville's theorem: The product of the bunch length and the energy spread within it is a constant. In this work, a concept is presented that circumvents this problem. A circularly polarized standing wave deflects the charged particle beam to a rotating orbital, feeding the particles into a propagating wave that rotates within a toroidal wave guide. The circular deflection supplies a time coding. The entrance point of time of any particle is locked into its azimuthal position. Provided that the deflecting field and the rotating propagating wave (denoted by the term *working field* in the following) are synchronized correctly the optimum phase condition is fulfilled exactly and constantly. Time uncertainty vanishes within the limits of technical and practical implementing of the concept. The working field may be cascaded. It can be used for a large variety of applications, such as monochromatizing, accelerating, spread inversion, and time focusing. A monochromator based on circular deflection was demonstrated to work by computer simulation. The energy spread

vanishes within the limits of technical and practical implementing of the concept without any loss of current. As a second key aspect in my talk, I will present a vision of a dynamic TEM illumination column based on circular deflection that yields equidistant monochromatic one-electron pulses. The latter concept makes use of plasmonic field emitters synchronized to the deflection and working fields.

Optimization of Pulsed Photoemission TEM

E. Kieft

FEI Company, Eindhoven, The Netherlands

Defining, and optimizing, the performance of a pulsed transmission electron microscope (TEM) operating on femtosecond-to-nanosecond timescales, is an entirely different situation from normal, continuous operation. We will look at two aspects. First, pulsed operation, be it in "stroboscopic" or "single-shot" mode, necessitates the use of high peak current values. As a consequence, stochastic blur, which is the result of microscopic electron-electron interactions in the imaging section of the column, becomes a limiting factor to image resolution in all but the single–electron–pulse cases. As such, one needs to take it into account when considering the beam parameters (brightness, emittance, and number of pulses, if applicable) for a given experiment. To this end, particle-tracking simulations that include mutual particle interactions have been performed on a simplified optical system. The results can be fitted to two different power laws for the blur-limited imaging resolution – one each for the so-called Pencil beam and Holtzmark regimes of stochastic blur. These fits can be combined with other scaling laws in order to guide optimization of the overall resolution (or info limit) as a function of, among other things, pulse duration, field of view size, and image contrast type. Note that, contrary to conventional wisdom, it is found that the highest brightness is not necessarily always best in pulsed imaging. Second, the electron source needs to be matched to the desired beam parameters as well as possible. It is advantageous to have an electron gun that can be easily modified and optimized for a given task. Again, particle tracking simulations can be employed to provide guidance on optimization of the electron gun. The method is applied to the photoemission gun of the newly introduced Tecnai Femto UEM, a versatile instrument based on the UEM-1 and UEM-2 prototypes at Caltech. Its design is based on a standard LaB6-gun with a Wehnelt electrode. Parameter scans show how a few simple degrees of freedom can be exploited to tune performance of the gun and optimize it for varying types of experiments.

Electron Beam Physics and the Limits of Instrument Performance

B.W. Reed, T.B. LaGrange, W.J. DeHope, G. Huete, J.T. McKeown, M.K. Santala
Lawrence Livermore National Laboratory, California, USA

Short–pulse electron probe instruments, including dynamic transmission electron microscopes (DTEMs) and various flavors of ultrafast electron diffraction and microscopy (UED/UEM) systems, cover a wide range of operating parameters, but they have one thing in common: They all aim to use electrons to extract information from a small volume of material in as short a time as possible. While some scientific problems can be studied in the limit of a single electron per pulse, in all other cases, we must contend with electron beams with beam currents orders of magnitude higher than is normal for a conventional electron microscope. This introduces unique problems, including space charge effects, stochastic blur, and complex electron-sample interactions, but it also forces us to make the best possible use of the limited brightness of our electron sources. This talk will discuss the physical laws that govern electron beams as they relate to practical applications in DTEM, UED, and UEM, using six-dimensional phase space as a unifying concept. The technology is reaching the point where substantial performance improvements beyond the current state of the art can be achieved only by dramatically reducing the entropy of the electron beam at the source.

Effect of Coulomb Interactions on Resolution in Ultrafast Electron Microscopy

H. Rose
Central Facility of Electron Microscopy, Universität Ulm, Ulm, Germany

Pulsed electron beams are increasingly applied in dynamic electron microscopy for visualizing fast processes such as local changes of magnetization, phase transformations and chemical reactions. Photoemission electron microscopy with pulsed excitation sources like lasers or synchrotron radiation has been evolved as a standard method for observing dynamic processes on surfaces (Bostanjoglo & Weingärtner 1997; Krasyuk et al., 2003). Recently, it has been suggested to employ high-intensity ultrashort electron beams for recording single-shot diffraction patterns or images of radiation-sensitive biological objects (King et al., 2005).

Periodic processes can be observed with low-current densities by means of stroboscopic techniques, which are mainly employed for investigating oscillating currents, voltages, and magnetic domains in microelectronic devices. However, these techniques cannot be used for visualizing non-periodic processes or for obtaining a single-shot diffraction pattern or image, respectively. In order to achieve high spatial resolution, the pulse must contain as many electrons as possible. However, due to the repulsive Coulomb interaction between electrons, it is not possible to confine a very large number of electrons in a very small volume. Moreover, these interactions broaden the energy width of the image-forming beam and change the direction of flight of the electrons. As a result, the image spot will be broadened even if chromatic aberration has been corrected (Weidenhausen et al., 1985). This loss of resolution will also arise for the diffraction pattern.

The mean space charge acts like a change of the focal length and of the aberrations of the electron lenses. Therefore, this stationary effect can be compensated for in an aberration-corrected microscope. Unfortunately, this correction is not possible for the effects resulting from the stochastic interactions. Ray deflections arising within the lenses from stochastic interactions are most deleterious, because even small angular deviations may result in appreciable displacements at the image plane owing to the large distance between the lenses and the image plane. This deleterious effect also prevails for a lens-less system, which reduces the resolution of the diffraction pattern.

The broadening of the diffraction or image spots resulting from stochastic interactions is inversely proportional to $U^{*3/4}$. Here, $U^* = U(1 + eU/2E_e)$ defines the relativistic modified acceleration voltage, and $E_e \approx 0.51$ MeV is the rest energy of the electron. Hence, the resolution increases significantly by going to higher voltages if the geometry of the system remains fixed. However, this condition cannot be met for an imaging system because the focal length of the magnetic lenses increases in proportion to U^* whenever their magnetic field has reached its maximum. Therefore, going to high voltages will only improve the resolution limited by stochastic interactions if superconducting lenses with short focal lengths are employed. Projector systems composed of quadrupoles are another alternative because quadrupoles are strong-focusing elements and can form astigmatic intermediate images of the source, thus reducing the current density and the resulting stochastic ray deflections.

Single elastic scattering prevails in amorphous objects whose thickness t is smaller than the elastic mean free path length. For simplicity, we assume that the object is composed of atoms with the same atomic number Z. In this case the relation $l_{el} = 1/n_A\sigma_{el}$ holds. Here, n_A is the atom density of the object and $\sigma_{el} \approx (E_e/eU^*)(1 + eU/E_e)^2 Z^{4/3}$ pm the elastic scattering cross section of the atom. This cross section is inversely proportional to U in the nonrelativistic regime and adopts the constant value $2Z^{4/3}$ pm^2 in the relativistic case $U >> 2E_e \approx 1$ MeV. For imaging thin ($t < l_{el}$) amorphous objects, it is advantageous to operate at lower voltages due to the larger fraction of scattered electrons. In addition, one can reduce the number of interactions in the regime between object and image by removing the non-scattered electrons in the back-focal plane of the objective lens by means of a beam stop. Two modes of dark-field imaging exist, of which the first mode uses parallel illumination and a central beam stop, while the other uses hollow cone illumination and a circular aperture. Compared to parallel illumination, this mode reduces the effect of the Coulomb interactions due to the large angles of illumination, which shorten the regions of high current density.

Instead of employing an annular aperture and a standard cathode for producing hollow cone illumination, it may be possible to develop a pulsed, high-intensity annular cathode. We achieve hollow-cone Koehler illumination by imaging this cathode into the back-focal plane of the objective lens. In order to minimize the Coulomb interactions and to utilize as many scattered electrons as possible large usable angles are required for the illumination hollow cone and the objective aperture. Such angles can be realized only by correcting the resolution-limiting aberrations.

REFERENCES

Bostanjoglo, O., & Weingärtner, M. (1997). Pulsed photoelectron microscope for imaging laser–induced nanosecond processes. *Review of Scientific Instruments, 68,* 2456.

King, W. E., Campbell, G. H., Frank, A., Reed, B., Schmerge, J. F., Siwick, B. J., et al. (2005). Ultrafast electron microscopy in materials science, biology, and chemistry. *Journal of Applied Physics, 9*7, 111101.

Krasyuk, A., Oelsner, A., Nepijko, S. A., Kuksov, A., Schneider, C. M., & Schönhense, G. (2003). Time-resolved photoemission electron microscopy of magnetic field and magnetisation changes. *Applied Physics A, 76,* 863–868.

Weidenhausen, A., Spehr, R., & Rose, H. (1985). Stochastic ray deflections in focused charged particle beams. *Optik, 69,* 126–134.

Electron Bunch Compression Using Static Fields

W. Wan
Lawrence Berkeley National Laboratory, California, USA

It is well known that a short electron bunch (e.g., 100 fs) with reasonably high charge (e.g., 10,000 electrons), would quickly expands to a few and, eventually, to hundreds of picoseconds due to space charges. In addition to limiting the number of electrons per bunch to the single digit, an RF cavity has been used to successfully compress high-charge electron bunches (0.2 pC) to about 0.5 ps. Another possible way of bunch compression that may potentially simplify the technology and improve stability is using static electrostatic or magnetic fields. The idea is that an achromatic beam transport line with positive R56 can make the head of the bunch, which is more energetic due to space charge, to travel a longer distance thus compressing the bunch. This talk will review the ideas that have been proposed and discuss the effect of Coulomb scattering on the final bunch length.

Space Charge Simulations of Photoemission Using the Differential Algebra–based Multiple-Level Fast Multipole Algorithm

H. Zhang[1], Z. Tao[2], C.-Y. Ruan[2], M. Berz[2]
[1]Thomas Jefferson National Accelerator Facility, Virginia, USA
[2]Michigan State University, Michigan, USA

Abstract

A grid-free algorithm based on the multiple-level fast multipole algorithm and differential algebra (DA) has been developed to calculate the electrostatic field of an ensemble of charged particles and its high-order derivatives. The efficiency of the algorithm scales linearly with the number of particles for any arbitrary distribution. The algorithm is parallelized to further improve its efficiency. Simulation results on the photoemission process using this algorithm are presented.

Keywords: Space charge effect, fast multipole method, differential algebra (DA), photoemission

1. INTRODUCTION

Collective effects have become more and more important with the need for beams of higher and higher intensity. Numerical simulation is a very useful tool for the study of collective effects, and it is inevitable when the collective effect is strong and highly nonlinear. A new algorithm was developed to calculate the electrostatic field between charged particles. The algorithm combines the multiple level fast multipole algorithm (MLFMA) with differential algebraic (DA) tools (Berz, 1999). The MLFMA has an efficiency of $O(n)$ for n charged particles. Furthermore, it is grid-free; hence, any arbitrary charge distribution can be treated in a natural way. Using DA, we considerably simplify the mathematics, represent the potential as Taylor expansions in the Cartesian coordinates, and calculate not only the field but also its high–order derivatives.

1.1 The Strategy of the Multiple-Level Fast Multipole Algorithm (MLFMA)

In order to evaluate the electrostatic field due to an arbitrary distribution of charges, we divide the charges into groups and evaluate the interactions between the groups far enough away by multipole expansions, and calculate

the interactions between nearby particles directly. The domain containing charged particles is divided into boxes of different sizes according to the charge density in order to keep a roughly equal amount of particles inside each box.

The relation between boxes can be represented as a hierarchical tree. Small boxes generated by splitting a large box are called the *child boxes* of the large box, and the large box is called the *parent box* of the small ones. The boxes that have no child boxes are called *childless boxes*. If the distance between box A and box B is larger than the side length of A, then we can represent the contribution from the charges inside A to the potential in B by a multipole expansion. Also, we can represent the contribution from the charges inside B to the potential inside A by a local expansion.

For a childless box, the multipole expansion is calculated from the charges inside, while for a parent box, the multipole expansion is calculated from the multipole expansions of its child boxes. The local expansion can be calculated from the charges inside a childless box that is far enough away, or from the multipole expansion of a parent box that is far enough away. Child boxes also inherit the local expansions from their parent boxes. The general strategy is to calculate the multipole expansions for all the boxes from the finest level to the coarsest level going upward, and then calculate the local expansions for all the boxes from the coarsest level to the finest level going downward. Once the expansions in all the boxes are calculated, the field on each particle can be calculated separately by two parts. The part due to the particles nearby is calculated using the Coulomb formula directly, while the field due to the particles far away is calculated from the multipole expansions, the local expansions, or both. A detailed description of the MLFMA can be found in reference (Carrier et al., 1988).

1.2 Differential Algebras and COSY INFINITY

In the vector space of the infinitely differentiable functions $C^\infty(R^v)$, we define an equivalence relation "$=_p$" between two functions $a, b \in C^\infty(R^v)$ via $a =_p b$ if $a(0) = b(0)$ and if all the partial derivatives of a and b at 0 agree up to the order p. Note that the point 0 is selected for convenience, and any other point could be chosen as well. The set of all b that satisfies $b =_p a$ is called the *equivalence class* of a, which is denoted by $[a]_p$. We denote all the equivalence classes with respect to $=_p$ on $C^\infty(R^v)$ as ${}_pD_v$. The addition, scalar multiplication, multiplication, and the derivation operator ∂_v can be defined on ${}_pD_v$ as

$$[a]_p + [b]_p := [a+b]_p, \quad c \cdot [a]_p := [c \cdot a]_p,$$
$$[a]_p \cdot [b]_p := [a \cdot b]_p, \quad \partial_v[a]_p := [\partial a/\partial x_v]_{p-1},$$

where x_v is the vth variable of the function a, and the operator ∂_v satisfies $\partial_v([a] \cdot [b]) = [a] \cdot (\partial_v[b]) + (\partial_v[a]) \cdot [b]$. Hence $_pD_v$ is a differential algebra (DA) (Berz, 1999). There are v special classes $d_v = [x_v]$, whose elements are all infinitely small. If a function a in $_pD_v$ has all the derivatives $c_{J_1,...,J_v} = \partial^{J_1 + \cdots + J_v} a/\partial x_1^{J_1} \cdots \partial x_v^{J_v}$, and then $[a]$ can be written as $[a] = \sum c_{J_1,...,J_v} \cdot d_1^{J_1} \cdots d_v^{J_v}$. Thus, $d_1^{J_1} \cdots d_v^{J_v}$ is a basis of the vector space of $_pD_v$.

COSY INFINITY (Berz & Makino, 2013) is a program developed for high-performance modern scientific computing, which supports DA as an advanced data type. By evaluating a function f in DA data type in COSY, one can get its Taylor expansion f_T, represented by a DA vector, up to an arbitrary predetermined order p automatically. If we consider two functions $f, g \in {}_pD_v$ which can also be viewed as two maps M_f and M_g, the function $f(g)$—i.e., the composition of the two maps $M_f \circ M_g$—can be easily calculated by the command POLVAL in COSY (Berz & Makino, 2013). For more details about DA, refer to Berz (1999).

2. EXPANSIONS IN THE DA FRAMEWORK

Here, we present a summary of the fast multipole method in the DA framework. For full details, we refer to Zhang (2013) and Zhang and Berz (2011).

2.1 The Far Multipole Expansion from the Charges

Suppose that n particles with charge q_i located at $\vec{r}_i(x_i, y_i, z_i)$, with $r_i < a$, then the electrostatic potential at a point $\vec{r}\,(x, y, z)$, with $r > a$ expressed as

$$\phi = \sum_{i=1}^{n} \frac{q_i}{|\vec{r}_i - \vec{r}|} = d \cdot \overline{\phi}_M, \tag{1}$$

where

$$\overline{\phi}_M = \sum_{i=1}^{n} \left\{ \frac{q_i}{\sqrt{1 + r_i^2 d^2 + 2\vec{r}_i \cdot \vec{d}}} \right\}, \quad \vec{d} = \frac{\vec{r}}{r^2}, \quad d = \left|\vec{d}\right|.$$

If we choose d_x, d_y, and d_z, the components of $\vec{d}$, as DA variables, $\overline{\phi}_M$ can be expressed as a DA vector, which can be considered as the Taylor expansion of $\overline{\phi}_M$ with respect to d_x, d_y, and d_z at infinity. If we calculate the DA vector up to order p, the error of approximating ϕ by its expansion can be estimated as

$$|\epsilon| \leq C \cdot \left(\frac{a}{r}\right)^{p+1} \cdot \frac{1}{r-a}, \quad \text{with} \quad C = \sum_{i=1}^{n} |q_i|. \tag{2}$$

2.2 The Translation of the Far Multipole Expansion

The potential ϕ at $\vec{r}(x, y, z)$ of a far multipole expansion at the origin $\vec{O}(0,0,0)$ can be translated into another far multipole expansion at the point $\vec{r}'_o(x'_o, y'_o, z'_o)$. The new DA variables can be chosen as

$$\vec{d}' = \frac{\vec{r} - \vec{r}'_o}{r'^2} = \frac{\vec{r}'}{r'^2}.$$

With some direct algebra, one can find the relation between the new DA variables $\vec{d}'$ and the old DA variables $\vec{d}$ as

$$\vec{d} = \left(\vec{d}' + d'^2 \cdot \vec{r}'_o\right) \cdot R, \tag{3}$$

with $R = 1/\left(1 + r'^2_o d'^2 + 2\vec{r}'_o \cdot \vec{d}'\right)$. Eq. (3) can be considered the map between the new DA variables and the old DA variables, which we refer to as M_1. If we translate $\overline{\phi}_M$ in the old frame into $\widetilde{\phi}_M$ in the new frame by

$$\widetilde{\phi}_M = \overline{\phi}_M \circ M_1,$$

the potential in the new frame can be written as

$$\phi' = \widetilde{\phi}_M \cdot d' \cdot \sqrt{R} = d' \cdot \overline{\phi}'_M, \tag{4}$$

knowing that d in the old frame can be translated into the new frame as $d = d' \cdot \sqrt{R}$. The error of the DA expression for ϕ' has the same expression with Eq. (2) with r and a defined in the new frame.

2.3 The Local Expansion from the Charges

Consider an observer point $\vec{r}\,(x, y, z)$ within a spherical region of the radius b centered at $\vec{r}'_o(x'_o, y'_o, z'_o)$, then the electrostatic potential on the observer from n particles outside the spherical region can be expressed as a local expansion at $\vec{r}'_o(x'_o, y'_o, z'_o)$. We choose the DA variables as

$$\vec{d}' = \vec{r} - \vec{r}'_o = \vec{r}'. \tag{5}$$

Assuming the ith source particle has charge q_i and located at $\vec{r}_i\,(x_i, y_i, z_i)$, the local expansion of the potential is

$$\phi_L = \sum_{i=1}^{n} \frac{q_i}{\left|\vec{r} - \vec{r}_i\right|} = \sum_{i=1}^{n} \frac{q_i}{\left|\vec{r}'_o - \vec{r}_i + \vec{d}'\right|}. \tag{6}$$

The error of the DA expression of ϕ_L up to order p can be estimated as

$$|\epsilon| \leq C \cdot \left(\frac{r'}{b}\right)^{p+1} \cdot \frac{1}{b - r'} \quad \text{with} \quad C = \sum_{i=1}^{n} |q_i|. \tag{7}$$

2.4 The Conversion of the Far Multipole Expansion into a Local Expansion

Given a far multipole expansion at the origin $\vec{O}\,(0,0,0)$, a local expansion at $\vec{r}'_o(x'_o, y'_o, z'_o)$, which creates the same potential on the observers, can be found. It is called *local* because $\vec{r}'_o(x'_o, y'_o, z'_o)$ is close to the observer $\vec{r}\,(x, y, z)$. So it is natural to choose the new DA variables as

$$\vec{d}' = \vec{r} - \vec{r}'_o = \vec{r}' \tag{8}$$

where $\vec{r}'(x', y', z')$ are the new coordinates of the observer $\vec{r}\,(x, y, z)$ if we shift the origin to $\vec{r}'_o(x'_o, y'_o, z'_o)$. The old and the new DA variables have the relation

$$\vec{d} = \frac{\vec{r}}{r^2} = \left(\vec{r}'_o + \vec{d}'\right) \cdot R, \tag{9}$$

where $R = 1/\left|\vec{r}'_o + \vec{d}'\right|^2$. We note Eq. (9) as M_2. To convert the far multipole expansion in Eq. (4) into a local expansion, we need to work on the two parts separately. The $\overline{\phi}'_M$ can be converted into $\widetilde{\phi}_L$ in the new frame as

$$\widetilde{\phi}_{\mathrm{L}} = \overline{\phi}'_{\mathrm{M}} \circ M_2,$$

and d' can be converted into $\sqrt{R}$ in the new frame. Therefore, we have the local expansion as

$$\phi_{\mathrm{L}} = \widetilde{\phi}_{\mathrm{M}} \cdot \sqrt{R}. \tag{10}$$

Note that by now we obtained the expansion of the potential, not just a component of it, as a DA vector. The error of a local expansion up to order p converted from a far multipole expansion is

$$|\epsilon| \le C \cdot \left(\frac{a}{r'_o}\right)^{p+1} \cdot \frac{1}{r'_o - a} + C \cdot \left(\frac{r'}{b}\right)^{p+1} \cdot \frac{1}{b - r'}, \tag{11}$$

where a, b, and C have the same meaning as in Eqs. (2) and (7).

2.5 The Translation of the Local Expansion

A local expansion at the origin $\vec{O}(0, 0, 0)$ can be translated to $\vec{r}'_o(x'_o, y'_o, z'_o)$, assuming that both points are close to the observer $\vec{r}\,(x, y, z)$. Choosing the new DA variable as the same as Eq. (5), the relation between the old and the new DA variables is just a linear shift:

$$\vec{d} = \vec{r}'_o + \vec{d}'. \tag{12}$$

We call Eq. (12) the map M_3, and then the new local expansion can be calculated by

$$\phi'_{\mathrm{L}} = \phi_{\mathrm{L}} \circ M_3. \tag{13}$$

This linear translation does not bring any additional error.

2.6 The Calculation of the Potential and the Field from the Expansions

It is straightforward to calculate the potential from a local expansion or a multipole expansion. Since we have the potential expressed as a pth order polynomial, we only need to plug in the value of (d_x, d_y, d_z) for each particle to obtain the potential for it.

The local expansion of the potential is a polynomial of the observer's coordinates. Taking the derivative of the potential with respect to a coordinate, one can obtain the $(p-1)$th-order polynomial for the field on the respective direction.

The DA variables in the multipole expansions are analytical functions of the coordinates. To calculate the field by the multipole expansion, we take the derivative with respect to the coordinates by the chain rule, and we obtain the expression of the field as

$$E_x = \left\{ -\frac{\partial \overline{\phi}}{\partial d_x} \cdot \left(d^2 - 2d_x^2 \right) + 2\frac{\partial \overline{\phi}}{\partial d_y} \cdot d_x d_y + 2\frac{\partial \overline{\phi}}{\partial d_z} \cdot d_x d_z + \overline{\phi} \cdot d_x \right\} \cdot d,$$

$$E_y = \left\{ 2\frac{\partial \overline{\phi}}{\partial d_x} \cdot d_y d_x - \frac{\partial \overline{\phi}}{\partial d_y} \cdot \left(d^2 - 2d_y^2 \right) + 2\frac{\partial \overline{\phi}}{\partial d_z} \cdot d_y d_z + \overline{\phi} \cdot d_y \right\} \cdot d, \quad (14)$$

$$E_z = \left\{ 2\frac{\partial \overline{\phi}}{\partial d_x} \cdot d_z d_x + 2\frac{\partial \overline{\phi}}{\partial d_y} \cdot d_z d_y - \frac{\partial \overline{\phi}}{\partial d_z} \cdot \left(d^2 - 2d_z^2 \right) + \overline{\phi} \cdot d_z \right\} \cdot d.$$

3. RESULTS OF NUMERICAL EXPERIMENTS

We now present some results of numerical experiments. In Figure 1, we compare the DA-based MLFMA with direct calculation using the Coulomb formula. The computational expense as a function of particles can be fitted by a straight line in a logarithmic representation for both cases. The slope for the direct Coulomb formula calculation is 2, reflecting the fact that for n charged particles, the computation time is proportional to n^2. The slope of the DA-based MLFMA is 1.073, which is very close to linear scaling with a slope of 1. Also, we can see that when $n > 1000$, the DA-based MLFMA outperforms the Coulomb formula in speed. Here, the DA-based MLFMA is conducted with DA in the fifth-order, while having a relative error less than 0.001.
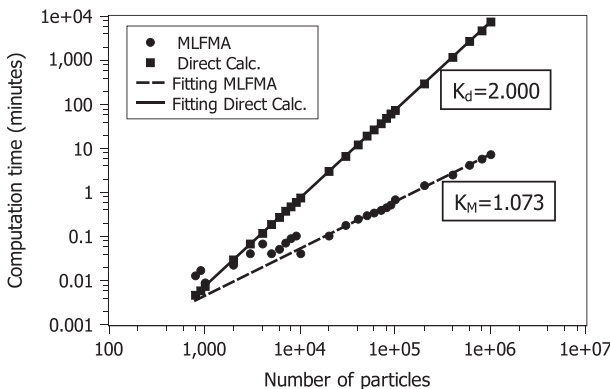
Figure 1 Efficiency of the DA-based MLFMA versus the Coulomb formula.
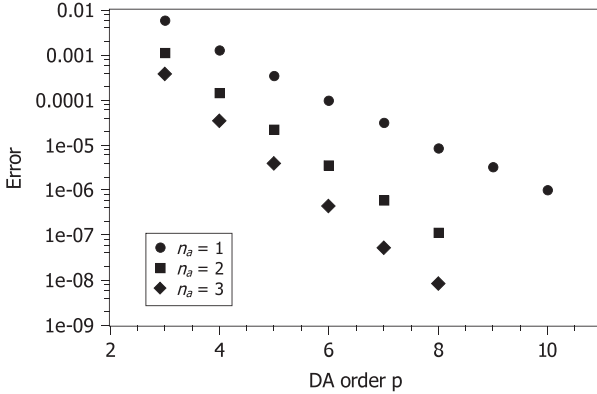
Figure 2 Error decreases as p and n_a increase (Zhang, 2013).

There are two ways to increase the accuracy. One is to increase the order of the DA calculations. The other is to increase the distance between two boxes whose interaction can be represented by expansions. As defined previously, expansions are used to represent the contribution of box A to the field in box B, when their distance is equal to or larger than the side length of A. To increase the accuracy, one can increase the distance to n_a times the side length of A, with $n_a \geq 1$. As shown in Figure 2, when p, the order of DA, increases, the error decreases. And for the same p, when n_a increases, the error decreases. We also notice that for a larger n_a, the error decreases faster (larger slope) with the increase of p. If one wants to calculate the field with a very high precision, it is better to increase n_a as well rather than merely increasing the DA order.

4. SPACE CHARGE SIMULATIONS OF PHOTOEMISSION AND COMPARISON WITH EXPERIMENTAL MEASUREMENTS

We have performed experiments to measure the ultrafast electron pulse dynamics immediately following photoemission (Tao et al., 2012) using a point projection imaging technique (Raman et al., 2009). A 50-fs laser pulse is applied to the gold photo cathode surface with an incidence of 45 deg to trigger the photoemission. The laser has a Gaussian profile with an elliptical cross section having $\sigma_x = 115$ μm and $\sigma_y = 81$ μm, which would generate a pancake-shaped electron bunch. A constant longitudinal extracting field perpendicular to the cathode surface is also applied. In simulations, instead of assuming an initial distribution, we generate the electrons

by groups following the three–step model (Jensen et al., 2010). The number of electrons in each group is in proportion to the laser pulse strength at the respective time slot. Once generated, the electrons move under the influence of the extraction field, the space charge field and the field of the image charge on the surface. The space charge field is calculated by the DA-based MLFMA. Based on COSY's MPI support, a parallel version of the algorithm is developed that allows the use of millions of macroparticles in our simulations.

The number of surviving electrons depends on the total amount of electrons generated and the strength of the extracting field. In Figure 3, we plot
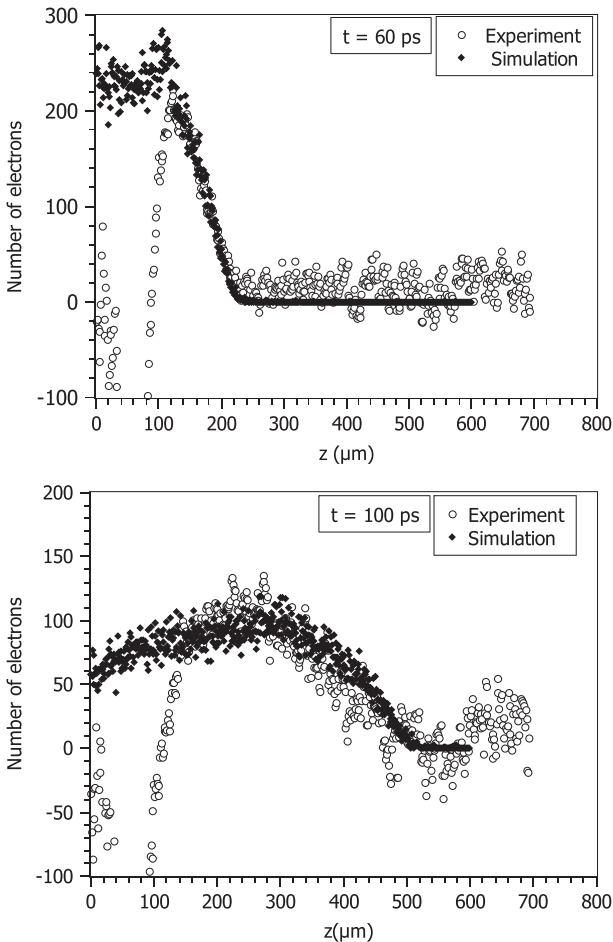
Figure 3 Longitudinal charge distribution of the electron bunch.
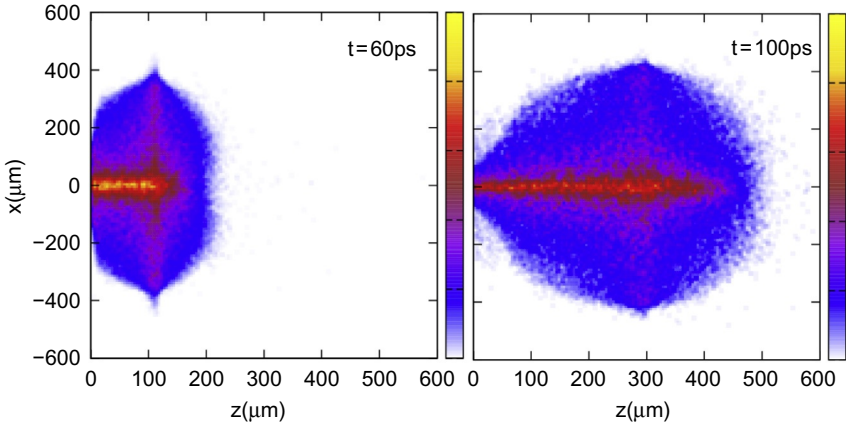
Figure 4 Charge distribution in *x-z* phase space (Zhang, 2013).

the longitudinal distribution of surviving electrons at 60 ps and 100 ps. The cathode surface is on the plane of $z = 0$, and the extracting field is in the z-direction. Ignoring the experimental data close to the surface, the simulation and the experiment agree well for the peak position and the bunch shape. Figure 4 shows the charge density on the *x-z* plane at 60 ps and 100 ps, with x representing any transverse direction. These figures show the microstructure of the bunch and help us to understand the microdynamics of the space charge effect in the photoemission process. More simulations and discussions on our photoemission experiments can be found in Portman et al. (2013, 2015).

5. CONCLUSION

We have developed the DA-based MLFMA, which allows the calculation of the electrostatic field of an ensemble of charged particles in any arbitrary distribution with an efficiency that scales linearly with the number of particles. A parallel code for distributed structure cluster machines is also developed. In practice, we can simulate millions of particles in a reasonable time, and we have successfully applied this algorithm in the simulation of the photoemission process. The simulation results agree well with the experiments and reveal some information that is difficult to measure directly in experiments.

ACKNOWLEDGMENTS

REFERENCES

Berz, M. (1999), *Modern map methods in particle beam physics*, San Diego: Academic Press.

Berz, M., & Makino, K. (2013). *COSY INFINITY version 9.1 programmer's manual, Technical Report MSUHEP-101214-rev,* Department of Physics and Astronomy, Michigan State University, East Lansing, MI. See also http://cosyinfinity.org.

Carrier, J., Greengard, L., & Rokhlin, V. (1988). A fast adaptive multipole algorithm for particle simulations. *SIAM Journal on Scientific and Statistical Computing 9*, 669–686.

Jensen, K., O'Shea, P., Feldman, D., & Shaw, J. (2010). Emittance of a field emission electron source. *Journal of Applied Physics, 107*(1), 014903, 1–14. http://dx.doi.org/10.1063/1.3267288.

Portman, J., Zhang, H., Makino, K., Ruan, C.-Y., Berz, M., & Duxbury, P. M. (2015), Multiscale modeling of the ultrafast electron microscope: From the photocathode to the sample. In *Proceedings of the Conference on Femtosecond Electron Imaging and Spectroscopy, FEIS 2013.* 117–130.

Portman, J., Zhang, H., Tao, Z., Makino, K., Berz, M., Duxbury, P. M., & Ruan, C.-Y. (2013). Computational and experimental characterization of high-brightness beams for femtosecond electron imaging and spectroscopy. *Applied Physics Letters, 103*(25), 253115, 1–5.

Raman, R., Tao, Z., Han, T., & Ruan, C.-Y. (2009). Ultrafast imaging of photoelectron packets generated from graphite surface. *Applied Physics Letters, 95*(18), 181108, 1–3.

Tao, Z., Zhang, H., Duxbury, P. M., Berz, M., & Ruan, C.-Y. (2012). Space charge effects in ultrafast electron diffraction and imaging. *Journal of Applied Physics, 111*(4), 044316, 1–10.

Zhang, H. (2013). The fast multipole method in the differential algebra framework for the calculation of 3D space charge fields, Ph.D. thesis, Michigan State University, East Lansing.

Zhang, H., & Berz, M. (2011). The fast multipole method in the differential algebra framework. *Nuclear Instruments and Methods A 645*, 338–344.

Synergistic Development and Further Discussion

Development and Application of In Situ Gas and Liquid Stages for Quantified TEM, STEM, and DTEM Observations

N.D. Browning[1], P. Abellan[1], I. Arslan[1], J.E. Evans[1], M. Gu[1], L. Mehdi[1], C. Park[2], L.R. Parent[3], W.D. Ristenpart[3], C. Wang[1], D. Welch[3], T.J. Woehl[3], H. Yang[3]

[1]Pacific Northwest National Laboratory, Washington, USA
[2]Florida A&M University – Florida State University College of Engineering, Florida, USA
[3]University of California, Davis, California, USA

The last 10 years have seen a paradigm change in (scanning) transmission electron microscopy ((S)TEM) with unprecedented improvements in spatial, spectroscopic, and temporal resolution being realized by aberration correctors, monochromators, and pulsed photoemission sources. Spatial resolution now extends to the sub-angstrom level, spectroscopic resolution into the sub-100-meV regime, and temporal resolution for single-shot imaging with dynamic transmission electron microscopy (DTEM) is now on the nanosecond timescale (stroboscopic imaging extends this even further, to femtoseconds). The challenge now in performing experiments in an (S/D)TEM is to implement the in situ capabilities that will allow both engineering and biological systems to be studied under realistic environmental conditions. Performing experiments using in situ stages or full environmental microscopes presents numerous challenges to the traditional means of analyzing samples in an electron microscope we are now dealing with the variability of dynamic process rather than a more straightforward static structure. In this presentation, I will discuss the recent developments in the design and implementation of in situ stages being pursued at the Pacific Northwest National Laboratory (PNNL). Examples of the use of these capabilities for the direct imaging of oxidation and reduction in metals, ceramics and catalytic systems and to identify the fundamental processes involved in nucleation and growth of nanostructures from solution will be presented. As the in situ stages have been designed to be incorporated into both high-spatial-resolution aberration-corrected (S)TEM as well as into high-temporal-resolution DTEM, the potential for future experiments to study dynamics, including those in live biological structures, will also be discussed.

Analysis of Beam-Sensitive Materials by Electrons and X-rays

R.F. Egerton[1], T. Konstantinova[2], Y. Zhu[2]
[1]University of Alberta, Edmonton, Canada
[2]Brookhaven National Laboratory/Stony Brook University, New York, USA

Abstract

Structural and chemical analysis by electron and X-ray beams is compared, with emphasis on organic specimens and the limitations to spatial resolution that are imposed by radiation damage.

Keywords: TEM, X-ray, radiation damage, dose-limited resolution

1. INTRODUCTION

Both electrons and X-rays are widely used for materials characterization, the atomic structure of most crystalline materials having been determined from the diffraction of hard X-rays using laboratory sources or (with higher spatial resolution) synchrotron X-rays. Although X-ray beams cannot be focused down to atomic dimensions, diffractive imaging (recovering the phase of the diffracted electrons) allows the structural and morphological analysis of more complicated objects such as macromolecules. Near-edge (NEXAFS, XANES) and extended (EXAFS) fine structure of X-ray absorption edges helps further to determine the atomic structure of noncrystalline materials. Soft X-rays (often in the water window, with 280–540 eV of photon energy) can be focused by a zone plate, allowing chemical and elemental and analysis of light-element materials, including organic structures.

The transmission electron microscope (TEM) enables electron diffraction and direct imaging down to atomic resolution, the de Broglie wavelength being of subatomic dimensions for accelerating voltages above 10 kV. The TEM can also incorporate various forms of spectroscopy, including electron energy-loss spectroscopy (EELS) where ionization edges in the range of 100–2000 eV energy loss are the equivalent of X-ray absorption edges and can be used for elemental quantification or (via their fine structure) the determination atomic and electronic structure.

Various practical considerations influence the choice of electrons or X-rays. Hundreds of TEMs in the USA alone are capable of atomic resolution and many of these are equipped with EELS capability. State-of-the-art

TEMs (with aberration correction and a monochromated electron source) cost several million dollars and tend to be found in regional or national centers. Synchrotron X-ray sources are even more expensive, and there are a few dozen worldwide. X-ray measurements often take several hours, whereas TEM images, diffraction patterns, or spectra are usually recorded in seconds or minutes, in part because the goal of high-spatial resolution makes specimen or beam drift more significant, although this drift can often be compensated electronically.

Soft X-rays can be focused to 20 nm but only with about 5% efficiency, whereas electrons with energy greater than 60 keV can be focused with high efficiency to atomic dimensions, or even down to 50 pm in an aberration-corrected instrument. Because of these small lateral dimensions and the thin specimen required, the TEM is the instrument of choice for analyzing very small volumes (TEM-EELS can detect less than 10^{-19} g of some elements), whereas X-rays are often better at measuring low concentrations. Although focused-ion-beam (FIB) instruments have eased the situation, the requirements for a thin ($<1\ \mu$m) TEM specimen are limiting for some materials and the ability to use a microns-thick specimen in a synchrotron beam line makes the examination of materials in gaseous or liquid environments easier. However, environmental cells are also possible in the TEM and have recently become more practical, thanks to MEMS techniques and the possibility of liquid encapsulation in graphene (Wang et al., 2014).

Although electrons have the advantage in terms of focusing, many specimens are beam-sensitive and the spatial resolution of analysis is determined not by the optics of the system but by radiation damage. This damage can take various forms, depending on the nature of the specimen.

2. RADIATION DAMAGE

X-rays and electrons are both forms of ionizing radiation and give rise to *ionization damage*, also called *radiolysis*. In this process, energy is removed from the incident beam through inelastic interaction and the potential energy of the specimen is increased irreversibly. Incident electrons that are scattered inelastically by valence electrons lose typically 10–50 eV per inelastic event, while inner-shell excitation (important in heavier elements) can absorb hundreds of eV. For organic specimens, the mean energy loss is around 40 eV per inelastic event, with K-shell excitation accounting for around 20% of that value. Valence-electron excitation is largely a collective (plasmon) process but the plasmon decays rapidly, transferring its energy to

single electrons and generating secondary electrons that travel through the specimen and cause further damage through inelastic scattering, accounting for 80% of the damage in polymethyl methacrylate.

In the case of X-rays, the main inelastic process below 10 keV of photon energy is the complete absorption of photons through the photoelectric effect. The absorbing atom or molecule is excited to a higher-energy state and may not return to its original ground state, indicating damage. However, the main radiolysis damage comes from the photoelectrons that are generated, with energies of several eV or even thousands of eV, which travel through the specimen, suffer inelastic scattering, and create further damage.

A common assumption concerning radiolysis is that the amount of damage is proportional to the energy deposited in the specimen through inelastic interaction. This assumption is reflected in the measurement of radiation dose G in Grays (Gy):

$$G = (D/\rho)(E_{av}/\lambda_i),$$
(1)

where D is the fluence (incident electrons or photons per m^2), ρ is the density in kg/m^3, λ_i is the average distance (in meters) that an electron travels before inelastic scattering (or a photon before absorption), and E_{av} is the average energy exchange (in joules) per inelastic or absorption event. For soft X-rays ($E_{av} = 500$ eV), the absorption length λ_i is typically 1 μm in an organic material ($\rho = 1$ $g/cm^3 = 1000$ kg/m^3), giving G (in MGy) = (0.08) D, where the fluence D is in photons/nm^2. Electron microscopists employ a thin specimen and for convenience, they measure the dose as the fluence D. In Eq. (1), E_{av} can be specified in eV if D is expressed in C/m^2. For a typical organic or biological specimen, $E_{av} \approx 40$ eV and $\lambda_i = 100$ nm for 100-keV electrons, giving G(MGy) = (0.4) D(C/m^2).

The dose needed to destroy the molecular structure of an organic specimen (the so-called *critical dose*, G_c) varies from a few MGy for aliphatic amino acids to about 10^5 MGy for halogenated copper phthalocyanine. As a typical value, we will take $G_c = 40$ MGy (corresponding to $D_c \approx 10^2$ C/m^2 for 100-keV electrons), which is also roughly the value for polymethyl methacrylate (PMMA).

In a conducting material, radiolysis is effectively quenched; the high density of free electrons ensures that holes created as a result of electron excitation are filled before the atom or molecule has time to reorganize. Therefore, metals and semiconductors should not be damaged by X-rays. However, high-energy electrons carry appreciable momentum and high-angle

elastic scattering by atomic nuclei can transfer several eV or tens of eV to each nucleus, giving rise to *knock-on displacement damage*. In the interior of a crystal, this damage takes the form of displacement of atoms from lattice sites, producing interstitial atoms and vacancies. At the surface of a specimen, fast electrons can displace atoms into the surrounding vacuum (electron-beam sputtering) or along the surface (radiation-enhanced surface diffusion). The knock-on effect takes place only if the maximum energy transfer (in a 180-degree collision) exceeds the so-called displacement energy, implying a *threshold incident energy* below which displacement does not occur. In organic materials, these thresholds are often below 100 keV, so the TEM does produce knock-on damage but the characteristic dose is of the order of 10^6 MGy. In other words, the rate of knock-on damage is several orders of magnitude below that of radiolysis and can normally be neglected for organic specimens (Egerton, 2013).

3. DOSE-LIMITED RESOLUTION

For robust specimens (metals, some semiconductors, some insulators) the spatial resolution of X-ray or electron-beam analysis is determined by the focusing optics. But for a radiation-sensitive specimen, including most organic and biological specimens, radiation damage imposes a more severe limit, known as the dose-limited resolution (DLR). The dimension δ of the smallest specimen region from which a useful signal can be obtained (ΔN recorded electrons or photons, above to the background level N_b in neighboring pixels) depends on the required signal/noise ratio: $SNR = (DQE)^{1/2}$ $(\Delta N/N_{shot})$, where N_{shot} is the shot-noise component, equal to $(N + N_b)^{1/2}$ according to Poisson statistics, and the detective quantum efficiency DQE takes account of noise added by the detector. The number of recorded particles is $N = F\,D\,\delta^2$, where D is the incident fluence and F is the ratio of recorded to incident particles. Combining these equations, the dose-limited resolution δ is given by

$$\delta^2 = N/(FD) = (SNR)^2\,(DQE)^{-1}\,(FD)^{-1}\,(C^2 + 3C + 2)/C^2, \quad (2)$$

where $C = (N - N_b)/N_b = \Delta N/N_b$ is the contrast between the recorded pixel and its neighbors, which is negative in the case of absorption contrast. Usually, SNR is taken as 3 or 5 (Rose criterion) and for an ideal detector, where DQE = 1, Eq. (2) can be simplified to $\delta = (5/|C|)\,(F\,D/2)^{-1/2}$ for

$C << 1$ (low-contrast image) and to $\delta = 5\,(F\,D)^{-1/2}$ for $C >> 1$ (the feature of interest is absent in adjacent pixels).

In the case of soft X-ray absorption spectroscopy or imaging in the water window ($E_{av} \approx 500$ eV, $\lambda_i \approx 1\,\mu m$), a critical dose of $G_c \approx 40$ MGy translates into about 500 photons/nm^2. Assuming a 1-μm-thick specimen and using data for PMMA at the oxygen K-absorption edge, $C = -0.52$ and $F = 0.19$; then if we take DQE $= 0.5$, Eq. (2) gives $\delta \approx 11.5$ nm for oxygen mapping. This result would indicate that radiation damage is not resolution limiting in scanning-transmission X-ray microscopy (STXM), if the zone plate forms a focused probe of diameter > 20 nm on the specimen. But in a fixed-beam mode, the zone plate is placed between the specimen and detector; if its efficiency is 5%, F is reduced to $(0.19)(5/100) \approx 0.01$, giving $\delta = 52$ nm and indicating that resolution is now dose-limited.

The scanning transmission electron microscope (STEM) employs an annular dark-field detector to record dark-field images from electrons scattered through larger angles, for which the probability is relatively low. Even with an optimized detector, F in Eq. (2) is small, giving typical δ in excess of 4 nm for $G_c \sim 40$ MGy (Egerton, 2013).

The fixed-beam TEM often operates with an objective aperture that gives diffraction contrast by absorbing scattered electrons. With increasing specimen thickness, the DLR improves initially (due to an increase in contrast C) but then gets worse because F falls due to electron absorption at the objective aperture. In the case of a boundary in a polymer ($G_c = 40$ MGy) where the density changes by 10%, for example, low-kV gives better resolution for a very thin specimen, but $\delta < 10$ nm requires a thicker specimen and higher accelerating voltage (Egerton, 2014).

To obtain better resolution from an organic sample, the objective aperture can be replaced by a phase plate that changes the phase of the scattered electrons relative to the unscattered ones. With an ideal phase plate, Eq. (2) predicts near-atomic resolution (for 10% density change) for specimens thicker than 100 nm, even in a beam-sensitive specimen ($G_c = 40$ MGy; Egerton, 2014). Phase plates currently suffer from charging and contamination problems but are gradually being improved (Glaeser, 2013a). It might be possible in the future to extract high-resolution phase information in STEM mode by recording diffraction information from each pixel and using ptychographic processing (Sader et al., 2010; D'Alfonso et al., 2014).

The understanding of many biological processes depends upon knowing the *three-dimensional (3D)* structure of macromolecules such as proteins. Howells et al. (2009) have calculated the dose required for 3D imaging (with

SNR = 5) based on X-ray diffraction and compared this with the dose required for damage at the same resolution. Their data (see Figure 1) showed that 10-nm resolution is obtainable from a single voxel; better resolution requires averaging over many identical units, such as by preparing a crystalline sample of protein.

Figure 1 also shows the required dose of electrons, estimated from Eq. (2), assuming that a fraction δ/λ_e of electrons is diffracted from each voxel (λ_e = elastic MFP = 300 nm) and detected with DQE = 1. Because of the strong diffraction of electrons, the required dose is substantially less than for X-rays (Henderson, 1995) and 1.5-nm resolution becomes possible from measurement on a single molecule. Still better resolution is obtainable from a crystal, which explains the success of cryoelectron microscopy based on phase-contrast imaging of frozen-hydrated materials. Longer-range effects of radiation damage (specimen warping and shrinkage) can be problematic, but fast-readout, direct-recording detectors have helped to alleviate this problem (Glaeser, 2013b).

Atomic resolution by direct imaging is not possible with X-rays because of the focusing problem, so structure must be determined from diffraction
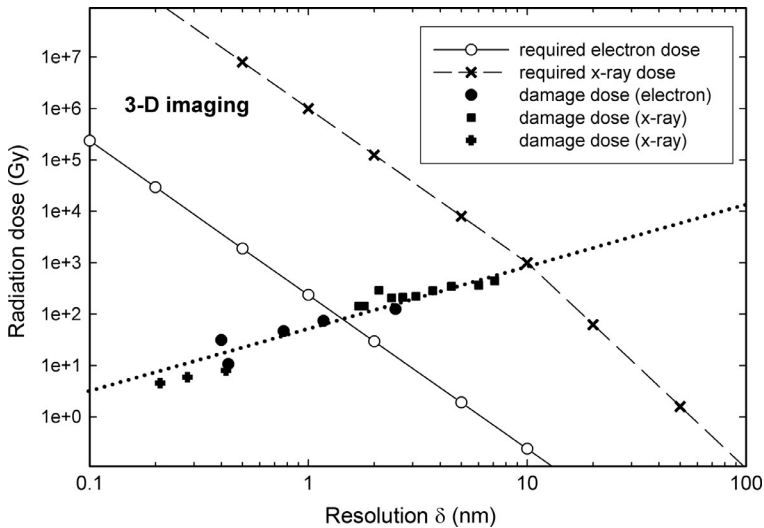
Figure 1 Dose of 1-keV X-rays (crosses, from Howells et al., 2009) and 100-keV electrons (open circles, taking $\lambda_i = 100$ nm, $\lambda_e = 300$ nm) required for SNR = 5 from a voxel of protein ($\rho = 1.35$ g/cm^3) of size δ. The dotted line represents damage doses measured by X-ray and electron diffraction; the best resolution of a single object corresponds to its intersection with the dashed line (for X-rays) or solid line (for electrons).

from a crystalline specimen. But some proteins cannot be crystallized; in response to this problem, very short (<100 fs) spatially coherent pulses generated from a free electron laser have been employed in diffract-before-destroy measurements. A diffraction pattern (sufficient to determine specimen orientation) is obtained from a particle (macromolecule or small crystal) before it is damaged, and then patterns from many orientations are combined to give sufficient resolution (<0.5 nm) to determine protein structure (Spence et al., 2012).

Could a similar diffract-before-destroy technique work with fast electrons? One difference is that electrons have appreciable momentum that can create knock-on damage. But as remarked earlier, such damage may be negligible compared to ionization damage. More serious is the fact that electrons carry electrostatic charge, so Coulomb repulsion within the incident beam limits the current density and provides a trade-off between the number of electrons per pulse and the pulse duration. Radio-frequency (RF) electron sources can produce 100-fs pulses with more than 10^5 electrons (Li et al., 2010; Muro'oka et al., 2011), and at these high-current densities, the primary repulsion comes from a space charge rather than stochastic repulsion. The space-charge effect is reduced at higher electron energy levels because the electrostatic repulsion is largely compensated for by magnetic attraction of the moving electrons. Ideally, the space charge can be compensated by refocusing (Kruit & Jansen, 1997), but solenoid focusing appears to be limited to several μm for 2.5-MeV electrons. If negligible damage occurs within 100 fs and if 10 electrons must be diffracted from a single particle of diameter d = 10 nm, then $10 = (d/D)^2 (10^5)(d/\lambda_e)$ and the beam diameter D needs to be no more than 100 nm. Use of a field-emission electron source, combined with the correction of spherical and chromatic aberration, might make phase-contrast (coherent) imaging possible on a sub-ns timescale (Armstrong et al., 2007; Reed et al., 2009), but this is clearly a major engineering challenge.

4. DIFFRACTIVE IMAGING

For observations of subtle structural changes in nano-objects, in particular aperiodic objects at femtosecond timescales, diffractive imaging is attractive because it requires no imaging lenses. Lens aberrations and beam crossovers (which can degrade temporal resolution) are avoided and the spatial resolution is then diffraction- or dose-limited. In diffractive imaging, a coherent beam of electrons or X-rays strikes an object and generates one or

more diffraction patterns, which are used to reconstruct an image via an iterative feedback algorithm (Weierstall et al., 2002). To achieve reliable reconstruction, a highly coherent incident beam is required because the technique uses wave interference to generate high-contrast interference patterns. Coherent waves must be generated at the source (photocathode, field emitter synchrotron, etc.), and the beam must maintain coherence until diffraction takes place.

Coherence of X-ray or electron waves is usually defined by a temporal (longitudinal) coherence length: $\lambda_L = \lambda^2/\Delta\lambda = vh/\Delta E$ and a spatial (transverse) coherence length: $\lambda_T = \lambda/2\pi\theta$, where λ is the de Broglie wavelength, v is the electron or photon speed, $h =$ the Planck constant; and ΔE and θ are the energy and angular spread of the beam, respectively (De Graef, 2003). It has been shown that the coherence width of the incident beam needs to be approximately twice the lateral width of the object to be imaged (or the unit cell, in the case of a crystal), Shannon sampling having twice the spatial period of Bragg sampling. As the coherence width is reduced, the size of the Bragg peaks in reciprocal space grows until they overlap, leading to a reduced image resolution. The longitudinal coherence length is the distance over which two waves from the same source point with slightly different wavelengths $\Delta\lambda$ will arrive completely out of phase. Small energy spread (small $\Delta\lambda$) is required to minimize loss of interference along the wave propagation direction and the loss of information due to the spread of information on detector pixels, especially when high-energy X-ray or electrons are used to extend the diffraction limit (Spence & Howells, 2002; Spence et al., 2004).

For a third-generation synchrotron X-ray source, such as at the Advanced Photon Source, the typical angular spread of the beam is 2×10^{-6} rad. If we assume a monochromated beam with a wavelength of $\lambda = 0.1$ nm and $\Delta\lambda/\lambda = 10^{-5}$, the longitudinal coherence length is about 5 μm and the transverse coherence length about 25 μm. In comparison, the ultrafast electron diffraction (UED) apparatus at BNL, equipped with an RF gun operated at 2.8 MeV and the best of its kind for time-resolved experiments with electrons, has $\approx 10^5$ electrons per pulse and time resolution ≈ 100 fs (Zhu et al., 2013). With a beam size of 300 μm on the sample, the temporal coherence length of the beam is about 2 nm and the spatial coherence length about 10 nm, likely insufficient for time-resolved diffractive imaging and at least 1000 times poorer than the coherent beams at the third-generation undulator source now routinely used for coherent diffractive imaging. However, future low-emittance photoguns

with pulse shaping and matching of workfunction and laser energy might improve the electron case by a factor of 10–100.

In the case of an ultrafast electron microscopy (UEM) setup with a photocathode replacing the FEG gun in a commercial transmission electron microscope, it was estimated that a spatial coherence length ≈ 1 nm might generate diffraction patterns with sufficient quality to reconstruct an image of a micron-sized protein crystal (Piazza et al., 2014). Again, the damage problem is reduced if the specimen consists of a large crystal (Gao et al., 2013).

5. SECONDARY DAMAGE

Although complete absence of radiation damage is desirable, it may not be essential depending on the resolution required. Secondary damage effects involving atomic motion over more than atomic distances (e.g., diffusion) occur over a longer timescale. Such processes include radical diffusion (taking ns or longer) and conformational or crystal relaxations, often requiring microseconds (Warkentin et al., 2011). They have recently been investigated by X-rays using detectors operating at ms timescales (Warkentin et al., 2013), while for electrons, direct-recording detectors can operate at 400 frames/sec (Li et al., 2013). Therefore, a combination of fast (but not ultrafast) detection and low specimen temperature may allow measurement before complete destruction has occurred, outrunning at least part of the damage. Many conformational changes in biological samples (including proteins) occur in the microsecond to millisecond time domain, suggesting that longer pulses could be used to determine secondary and tertiary structure, even if the primary (atomic) structure of the molecule is damaged.

The existence of secondary damage can give rise to a dose-rate dependence of damage, whenever the timescale of a damage process approaches or exceeds that of the measurement. Dose-rate dependence is commonly observed for *inorganic* materials where the dose rate (electron or X-ray fluence) can be relatively high because of the lower radiation sensitivity. There can even be a dose-rate threshold below which no damage is observable (Salisbury et al., 1984; Jiang & Spence, 2012). Dose-rate dependence is not usually observed for organic materials, except in an aqueous environment where longer-range radical diffusion contributes secondary damage (Cherezov et al., 2002) or at low temperatures where diffusion is slow (Egerton & Rauf, 1999).

Dose-rate effects are designated as *normal* or *inverse*, depending on whether the radiation sensitivity (damage/dose ratio) increases or decreases with increasing dose rate. Both effects may take place in the same specimen; for example, the sensitivity may first decrease as the dose rate increases, due to limited diffusion speed, but then increase at a high dose rate because of specimen heating by the beam (Egerton & Rauf, 1999).

The existence of a dose-rate effect could influence the choice of imaging mode. In fixed-beam microscopy, the dose rate is constant, whereas in scanning microscopy (STEM, STXM), the dose rate within a focused probe is high during the pixel-dwell time but then falls to zero (for that pixel) during the remainder of the frame time. Scanning mode could therefore be advantageous if the specimen shows an *inverse* dose-rate effect.

REFERENCES

Armstrong, M. R., Reed, B. W., Torralva, B. R., & Browning, N. D. (2007). Prospects for electron imaging with ultrafast time resolution. *Applied Physics Letters, 90*, 114101.

Cherezov, V., Riedl, K. M., & Caffrey, M. (2002). Too hot to handle? Synchrotron X-ray damage of lipid membranes and mesophases. *Journal of Synchrotron Radiation, 9*, 333–341.

D'Alfonso, A. J., Morgan, A. J., Yan, A. W. C., Wang, P., Sawada, H., Kirkland, A. I., & Allen, L.J. (2014). Deterministic electron ptychography at atomic resolution. *Physical Review B, 89*, 064101.

De Graef, M. (2003). *Introduction to conventional transmission electron microscopy*. Cambridge, UK: Cambridge University Press.

Egerton, R. F. (2012). Mechanisms of radiation damage in beam-sensitive specimens, for TEM accelerating voltages between 10 and 300 kV. *Microscopy Research and Technique, 75*, 1550–1556.

Egerton, R. F. (2013). Control of radiation damage in the TEM. *Ultramicroscopy, 127*, 100–108.

Egerton, R.F. (2014). Choice of operating voltage for a transmission electron microscope. *Ultramicroscopy, 145*, 85–93.

Egerton, R. F., & Rauf, I. (1999). Dose-rate dependence of electron-induced mass loss from organic specimens. *Ultramicroscopy, 80*, 247–254.

Gao, M., Lu, C., Jean-Ruell, H., Liu, L.C., Marx, A., Onda, K., et al. (2013). Mapping molecular motions leading to charge delocalization with ultrabright electrons. *Nature, 496*, 343–346.

Glaeser, R. M. (2013a). Methods for imaging weak phase objects in electron microscopy. *Review of Scientific Instruments, 84*, 111101.

Glaeser, R. M. (2013b). Stroboscopic imaging of macromolecular complexes. *Nature Methods, 10*, 475–476.

Henderson, R. (1995). The potential and limitations of neutrons, electrons and X-rays for atomic resolution microscopy of unstained biological molecules. *Quarterly Reviews of Biophysics, 2*, 171–193.

Howells, M. R., Beetz, T., Chapman, H. N., Cui, C., Holton, J. M., Jacobsen, C. J., Kirz, J., et al. (2009). An assessment of the resolution limitation due to radiation-damage in X-ray diffraction microscopy. *Journal of Electron Spectroscopy and Related Phenomena, 170*, 4–12.

Jiang, N., & Spence, J. C. H. (2012). On the dose-rate threshold of beam damage in TEM. *Ultramicroscopy, 113*, 77–82.

Kruit, P., & Jansen, G. H. (1997). Space charge and statistical Coulomb effects. Chapter 7 in J. Orloff (Ed.), *Handbook of charged particle optics* (pp. 275–318). New York: Springer.

Li, R., Huang, W., Du, Y., Yan, L., Du, Q., Shi, J., et al. (2010). Single-shot continuously time-resolved MeV ultrafast electron diffraction. *Review of Scientific Instruments, 81*, 036110.

Li, X., Mooney, P., Zheng, S., Booth, C.R., Braunfeld, M.B., Gubbens, S., et al. (2013). Electron counting and beam-induced motion correction enable near-atomic-resolution single-particle cryo-EM. *Nature Methods, 10*, 584–590.

Muro'oka, Y., Naruse, N., Sakakihara, S., Ishimaru, M., Yang, J., & Tanimura, K. (2011). Transmission-electron diffraction by MeV electron pulses. *Applied Physics Letters, 98*, 251903.

Piazza, L., Musumeci, P., Luiten, O. J., & Carbone, F. (2014). A proposal for fs-electron microscopy experiments on high-energy excitations in solids. *Micron, 63*, 40–46.

Reed, B. W., Armstrong, M. R., Browning, N. D., Campbell, G. H., Evans, J. E., LaGrange, T., & Masiel, D. J. (2009). The evolution of ultrafast electron microscope instrumentation. *Microscopy and Microanalysis, 15*, 272–281.

Sader, K., Brown, A., Brydson, R., & Bleloch, A. (2010). Quantitative analysis of image contrast in phase contrast STEM for low-dose imaging. *Ultramicroscopy, 110*, 1324–1331.

Salisbury, I. G., Timsit, R. S., Berger, S. D., & Humphreys, C. J. (1984). Nanometer scale electron beam lithography in inorganic materials. *Applied Physics Letters, 45*, 1289–1291.

Spence, J. C. H., & Howells, M. R. (2002). Synchrotron soft X-ray and field-emission electron sources: A comparison. *Ultramicroscopy, 93*, 213–222.

Spence, J. C. H., Weierstall, U., & Chapman, H. (2012). X-ray lasers for structural and dynamic biology. *Reports on Progress in Physics, 75*, 102601.

Spence, J. C. H., Weierstall, U., & Howells, M. (2004). Coherence and sampling requirements for diffractive imaging. *Ultramicroscopy, 101*, 149–152.

Wang, C., Qiao, Q., Shokuhfar, T., & Klie, R. F. (2014). High-resolution electron microscopy and spectroscopy of ferritin in biocompatible graphene liquid cells and graphene sandwiches. *Advanced Materials, 26*, 3410–3414.

Warkentin, M., Badeau, R., Hopkins, J., & Thorne, R. E. (2011). Dark progression reveals slow timescales for radiation damage between T = 180 and 240 K. *Acta Crystallographica Section D, 67*, 792–803.

Warkentin, M., Hopkins, J. B., Badeau, R., Mulichak, A. M., Keefe, L. J., & Thorne, R. E. (2013). Global radiation damage: Temperature dependence, time dependence, and how to outrun it. *Journal of Synchrotron Radiation, 20*, 7–13.

Weierstall, U., Chen, Q., Spence, J. C. H., Howells, M. R., Isaacson, M., & Panepucci, R. R. (2002). Image reconstruction from electron and X-ray diffraction patterns using iterative algorithms: Experiment and simulation. *Ultramicroscopy, 90*, 171–195.

Zhu, P., Cao, J., Zhu, Y., Geck, J., Hidaka, Y., Pjerov, S., et al. (2013). Dynamic separation of electron excitation and lattice heating during the photoinduced melting of the periodic lattice distortion in 2H-TaSe$_2$. *Applied Physics Letters, 103*, 071914.

Ancillary Ultrafast Electron Microscopy Techniques and Considerations for Studying Nanoscale Specimen Volumes

D.J. Flannigan
University of Minnesota, Minnesota, USA

In the first part of my talk, I will provide an overview of photon–induced near–field electron microscopy and outline practical approaches for in situ pulse characterization. For all methods used to study nonequilibrium processes, deconvolution is critical for isolating intrinsic dynamics that occur on timescales commensurate with the instrument response. In order to accomplish this, one must have a way to precisely measure the instrument response function, ideally at the specimen location. Here, I will describe how the response of the low-loss region of the electron energy spectrum during UEM experiments is caused by varying the temporal overlap of the femtosecond photon and electron pulses at the specimen. Relative temporal variation of the pulses causes a modulation of the partitioning of the electrons into quantized virtual states. Variation in the partitioning causes the zero loss peak intensity to fall and rise, with the curve being a convolution of the two interacting pulses, thus revealing the instrument response function in the low–fluence regime. In this way, intrinsic structural dynamics can be isolated from the overall instrument response.

In the second part of my talk, I will discuss considerations for achieving high spatial resolutions in UEM experiments. Conceptually, UEM can be thought of as consisting of combined ultrafast spectroscopy and electron microscopy laboratories having all the relevant apparatus and support equipment. To date, much attention has been focused on optimization of photoelectron pulse properties. In contrast, little emphasis has been placed on outlining and quantifying limitations imposed by environmental and specimen stability. Here, I will discuss effects of ambient conditions well known to both the ultrafast spectroscopy and electron microscopy communities and the impact on observables will be illustrated. I will describe some of the measures we are taking at Minnesota to identify and mitigate such artifacts. In short, the combination of sophisticated experimental techniques, desired high energy–space–time resolutions, and sensitivities to picometer/millielectron–volt changes requires a detailed, quantitative understanding

of specific environmental and specimen factors on femtosecond electron-based techniques. The magnitudes of these factors are nonuniversal and will vary greatly across labs, thus necessitating individualized efforts in identifying and deconvoluting inevitable artifacts from intrinsic dynamics.

Nonequilibrium Sum Rules for the Holstein Model

J.K. Freericks[1], K. Najafi[1], A.F. Kemper[2], T.P. Devereaux[3]
[1]Georgetown University, Washington D.C., USA
[2]Lawrence Berkeley National Laboratory, California, USA
[3]SLAC National Accelerator Laboratory/Stanford University, California, USA

Abstract

We derive frequency moment sum rules for the retarded electronic Green's function and self-energy of the Holstein model for both equilibrium and nonequilibrium cases. We also derive sum rules for the phonon propagator in equilibrium and nonequilibrium. These sum rules allow one to benchmark nonequilibrium calculations and help with interpreting the behavior of electrons driven out of equilibrium by an applied electric field. We exactly evaluate the sum rules when the system is in the atomic limit. We also discuss the application of these sum rules to pump/probe experiments like time-resolved angle-resolved photoemission spectroscopy.

Keywords: Nonequilibrium, electron-phonon problem, sum rules, Green functions, self-energy

1. INTRODUCTION

In recent years, we have seen significant advances in time–resolved experiments on systems that have strong electron–phonon interactions (Graf et al., 2011; Cortés et al., 2011). These experiments study how energy is transferred between the electronic and phononic parts of the system. One of the interesting effects that has been seen in these experiments is the so–called phonon–window effect (Sentef et al., 2013), where electrons with energies farther than the phonon frequency from the Fermi level relax quickly back to equilibrium after the pulsed field is applied, but those close to the Fermi level relax on a much longer timescale because their relaxation involves multiparticle processes due to a restricted phase space. It is clear that this experimental and theoretical work is just starting to analyze electron–phonon interacting systems in the time domain. Hence, any exact results that can be brought to bear on this problem will be important.

In this work, we derive sum rules for the zeroth and first two moments of the retarded electronic Green's function and for the zeroth moment of the retarded self–energy. The moment sum rules have already been derived in equilibrium (Kornilovitch, 2002; Rösch et al., 2007), but they actually hold

true, unchanged, in nonequilibrium as well (Turkowski & Freericks, 2006; Turkowski & Freericks, 2008; Freericks & Turkowski, 2009; Freericks et al., 2013). With these sum rules, one can understand how the electron–phonon interaction responds to nonequilibrium driving and how different response functions will behave.

We start with the so-called Holstein model (Holstein 1959a, b), given by the following Hamiltonian in the Schroedinger representation:

$$\mathcal{H}(t) = -\sum_{ij\sigma} t_{ij}(t) c_{i\sigma}^{\dagger} c_{j\sigma} + \sum_{i\sigma} \left[g(t)x_i - \mu\right] c_{i\sigma}^{\dagger} c_{i\sigma} + \sum_{i} \frac{p_i^2}{2m} + \frac{1}{2}\kappa \sum_{i} x_i^2, \quad (1)$$

where $c_{i\sigma}^{\dagger}(c_{i\sigma})$ are the fermionic creation (annihilation) operators for an electron at lattice site i with spin σ (with anticommutator $\left\{ c_{i\sigma}, c_{j\sigma'}^{\dagger} \right\}_{+} = \delta_{ij}\delta_{\sigma\sigma'}$), and x_i and p_i are the phonon coordinate and momentum (with commutator $[x_i, p_j]_{-} = i\hbar\delta_{ij}$), respectively. The hopping $-t_{ij}(t)$ between lattice sites i and j can be time dependent [for example, an applied electric field corresponds to the Peierls substitution (Peierls, 1933)], μ is the chemical potential for the electrons, $g(t)$ is the time-dependent electron–phonon interaction, m is the mass of the optical (Einstein) phonon and κ is the corresponding spring constant. The frequency of the phonon is $\omega = \sqrt{\kappa/m}$. It is often convenient to also express the phonon degree of freedom in terms of the raising and lowering operators $a_i^{\dagger}$ and a_i (with commutator $\left[a_i, a_j^{\dagger}\right]_{-} = \delta_{ij}$) with $x_i = \left(a_i^{\dagger} + a_i\right)\sqrt{\hbar/(2m\omega)}$ and $p_i = \left(-a_i^{\dagger} + a_i\right)\sqrt{\hbar m\omega/2}/i$. This Hamiltonian involves electrons that can hop between different sites on a lattice and interact with harmonic Einstein phonons that have the same phonon frequency for every lattice site. The hopping and the electron–phonon coupling are taken to be time dependent for the nonequilibrium case. We are setting $\hbar = 1$ and $k_B = 1$ for the remainder of this work.

2. FORMALISM FOR THE ELECTRONIC SUM RULES

Since we will be working in nonequilibrium, we need to allow the time to lie somewhere on the Kadanoff–Baym–Keldysh contour, which runs in the positive time direction from t_{min} to t_{max}, back to t_{min} and down the imaginary axis to $t_{min} - i\beta$, with $\beta = 1/T$ the inverse temperature (it is assumed that the system is in equilibrium at time t_{min}). Allowing the time

to be chosen anywhere on the contour, the contour-ordered electronic Green's function is defined by

$$G^c_{ij\sigma}(t, t') = -i\mathrm{Tr}\mathcal{T}_c e^{-\beta\mathcal{H}(t_{min})} c_{i\sigma}(t)c^\dagger_{j\sigma}(t')/\mathcal{Z}, \tag{2}$$

where $\mathcal{T}_c$ denotes time ordering along the contour, and $\mathcal{Z} = \mathrm{Tr}\exp[-\beta\mathcal{H}(t_{min})]$, with the system in equilibrium at the initial time t_{min} at a temperature $T = 1/\beta$. The Fermi operators are written in the Heisenberg representation $c_{i\sigma}(t) = U^\dagger(t, t_{min})c_{i\sigma}U(t, t_{min})$, with $U(t, t')$ the evolution operator from time t' to time t. The evolution operator satisfies $idU(t, t')/dt = \mathcal{H}(t)U(t, t')$ and $U(t, t) = 1$. From the contour-ordered Green's function, one can extract all of the needed Green's functions, like the so-called lesser Green's function and the retarded Green's function, which we consider in detail here and which is defined by

$$G^R_{ij\sigma}(t, t') = -i\theta(t - t')\mathrm{Tr}e^{-\beta\mathcal{H}(t_{min})}\left\{c_{i\sigma}(t), c^\dagger_{j\sigma}(t')\right\}_+ /\mathcal{Z}, \tag{3}$$

where $\{.,.\}_+$ denotes the anticommutator. Converting to Wigner's average and relative times $t_{ave} = (t + t')/2$ and $t_{rel} = t - t'$, we can find the frequency-dependent retarded Green's function for each average time via

$$G^R_{ij\sigma}(t_{ave}, \omega) = \int_0^\infty dt_{rel} e^{i\omega t_{rel}} G^R_{ij\sigma}\left(t_{ave} + \frac{1}{2}t_{rel}, t_{ave} - \frac{1}{2}t_{rel}\right). \tag{4}$$

The nth spectral moment in real space is then defined via

$$\mu^{Rn}_{ij\sigma}(t_{ave}) = -\frac{1}{\pi}\int_{-\infty}^\infty d\omega\, \omega^n \mathrm{Im}G^R_{ij\sigma}(t_{ave}, \omega). \tag{5}$$

The moments are more convenient to evaluate as derivatives in time:

$$\mu^{Rn}_{ij\sigma}(t_{ave}) =$$
$$\mathrm{Im}\left\{\frac{i^{n+1}}{\mathcal{Z}}\frac{d^n}{dt^n_{rel}}\mathrm{Tr}e^{-\beta\mathcal{H}(t_{min})}\left\{c_{i\sigma}\left(t_{ave} + \frac{1}{2}t_{rel}\right), c^\dagger_{j\sigma}\left(t_{ave} - \frac{1}{2}t_{rel}\right)\right\}_+ \bigg|_{t_{rel}=0^+}\right\}. \tag{6}$$

These time derivatives can be replaced by partial time derivatives with respect to time-dependent terms in the Hamiltonian plus commutators with the Hamiltonian. In particular, we find that

$$\mu^{R0}_{ij\sigma}(t_{ave}) = \mathrm{Tr}e^{-\beta\mathcal{H}(t_{min})}\left\{c_{i\sigma}(t_{ave}), c^\dagger_{j\sigma}(t_{ave})\right\}_+ /\mathcal{Z} \tag{7}$$

for the zeroth moment, and

$$
\begin{aligned}
\mu_{ij\sigma}^{R1}(t_{ave}) = &-\frac{1}{2}\left\langle \left\{ \left[\mathcal{H}_H(t_{ave}), c_{i\sigma}(t_{ave})\right]_-, c_{j\sigma}^\dagger(t_{ave}) \right\}_+ \right\rangle \\
&+\frac{1}{2}\left\langle \left\{ c_{i\sigma}(t_{ave}), \left[\mathcal{H}_H(t_{ave}), c_{j\sigma}^\dagger(t_{ave})\right]_- \right\}_+ \right\rangle
\end{aligned}
\tag{8}
$$

for the first moment, where the angle brackets denote the trace over all states weighted by the density matrix ($\langle O \rangle = \mathrm{Tr}\exp[-\beta\mathcal{H}(t_{min})]O/\mathcal{Z}$), the symbol $[.,.]_-$ denotes the commutator, and the subscript H on the Hamiltonian indicates that it is in the Heisenberg representation. The second moment is more complicated and satisfies

$$
\begin{aligned}
\mu_{ij\sigma}^{R2}(t_{ave}) = &-\frac{1}{4}\left\langle \left\{ \left[\mathcal{H}_H(t_{ave}), \left[\mathcal{H}_H(t_{ave}), c_{i\sigma}(t_{ave})\right]_-\right]_-, c_{j\sigma}^\dagger(t_{ave}) \right\}_+ \right\rangle \\
&-\frac{1}{2}\left\langle \left\{ \left[\mathcal{H}_H(t_{ave}), c_{i\sigma}(t_{ave})\right]_-, \left[\mathcal{H}_H(t_{ave}), c_{j\sigma}^\dagger(t_{ave})\right]_- \right\}_+ \right\rangle \\
&+\frac{1}{4}\left\langle \left\{ c_{i\sigma}(t_{ave}), \left[\mathcal{H}_H(t_{ave}), \left[\mathcal{H}_H(t_{ave}), c_{j\sigma}^\dagger(t_{ave})\right]_-\right]_- \right\}_+ \right\rangle \\
&+\frac{1}{4}\mathrm{Im}\left\langle \left\{ \left[\mathcal{H}_H'(t_{ave}), c_{i\sigma}(t_{ave})\right]_-, c_{j\sigma}^\dagger(t_{ave}) \right\}_+ \right\rangle \\
&+\frac{1}{4}\mathrm{Im}\left\langle \left\{ c_{i\sigma}(t_{ave}), \left[\mathcal{H}_H'(t_{ave}), c_{j\sigma}^\dagger(t_{ave})\right]_- \right\}_+ \right\rangle,
\end{aligned}
\tag{9}
$$

where the prime indicates that it is the Heisenberg representation of the time derivative of the Schroedinger representation Hamiltonian [i.e., $\mathcal{H}_H'(t_{ave}) = U^\dagger(t_{ave}, -\infty)\partial\mathcal{H}_S(t)/\partial t|_{t=t_{ave}} U(t_{ave}, -\infty)$]. One can directly see that the two terms with the derivative of the Hamiltonian [the last two lines of Eq. (9)] are equal and opposite and hence cancel each other out.

These moments now can be evaluated straightforwardly, although the higher the moment is, the more work it takes. We find the well-known result

$$
\mu_{ij\sigma}^{R0}(t_{ave}) = \delta_{ij}
\tag{10}
$$

for the zeroth moment. The first moment satisfies

$$
\mu_{ij\sigma}^{R1}(t_{ave}) = -t_{ij}(t_{ave}) - \mu\delta_{ij} + g(t_{ave})\langle x_i(t_{ave})\rangle\delta_{ij},
\tag{11}
$$

and the second moment becomes

$$
\begin{aligned}
\mu_{ij\sigma}^{R2}(t_{ave}) = &\sum_k t_{ik}(t_{ave})t_{kj}(t_{ave}) + 2\mu t_{ij}(t_{ave}) + \mu^2 \delta_{ij} \\
&- t_{ij}(t_{ave})g(t_{ave})\langle x_i(t_{ave}) + x_j(t_{ave})\rangle - 2\mu g(t_{ave})\langle x_i(t_{ave})\rangle\delta_{ij} \\
&+ g^2(t_{ave})\langle x_i^2(t_{ave})\rangle\delta_{ij}.
\end{aligned}
\tag{12}
$$

Unlike in the case of the Hubbard or Falicov-Kimball model, where the sum rules relate to constants or simple expectation values (Turkowski & Freericks, 2006; Turkowski & Freericks, 2008; Freericks & Turkowski, 2009), one can see here that one needs to know things like the average phonon coordinate and its fluctuations in order to find the moments. We will discuss this further later in this paper.

Our next step, is to calculate the self-energy moments, which are defined via

$$
C_{ij\sigma}^{Rn}(t_{ave}) = -\frac{1}{\pi}\int d\omega\,\omega^n \mathrm{Im}\Sigma_{ij\sigma}^R(t_{ave}, \omega).
\tag{13}
$$

Note that the self-energy is defined via the Dyson equation

$$
G_{ij\sigma}^R(t, t') = G_{ij\sigma}^{R0}(t, t') + \sum_{kl}\int d\bar{t}\int d\overline{t'}\, G_{ik\sigma}^{R0}(t, \bar{t})\Sigma_{kl\sigma}^R(\bar{t}, \overline{t'})G_{lj\sigma}^R(\overline{t'}, t'),
\tag{14}
$$

where G^{R0} is the noninteracting Green's function and the time integrals run from $-\infty$ to ∞. The strategy for evaluating the self-energy moments is rather simple. First, one writes the Green's function and self-energy in terms of the respective spectral functions:

$$
G_{ij\sigma}^R(t_{ave}, \omega) = -\frac{1}{\pi}\int \frac{\mathrm{Im}G_{ij\sigma}^R(t_{ave}, \omega')}{\omega - \omega' + i0^+}d\omega'
\tag{15}
$$

and

$$
\Sigma_{ij\sigma}^R(t_{ave}, \omega) = \Sigma_{ij\sigma}^R(t_{ave}, \infty) - \frac{1}{\pi}\int \frac{\mathrm{Im}\Sigma_{ij\sigma}^R(t_{ave}, \omega')}{\omega - \omega' + i0^+}d\omega'.
\tag{16}
$$

Next, one substitutes those spectral representations into the Dyson equation that relates the Green's function and self-energy to the noninteracting Green's function. By expanding all functions in a series in $1/\omega$ for large ω, one finds the spectral formulas involve summations over the moments. By employing the exact values for the Green's function moments, one can extract the moments for the self-energy. Details for the formulas appear elsewhere (Turkowski & Freericks, 2008). The result is

$$\Sigma^R_{ij\sigma}(t_{ave}, \infty) = g(t_{ave})\langle x_i(t_{ave})\rangle\delta_{ij} \tag{17}$$

and

$$C^{R0}_{ij\sigma}(t_{ave}) = g^2(t_{ave})\left[\langle x_i^2(t_{ave})\rangle - \langle x_i(t_{ave})\rangle^2\right]. \tag{18}$$

Therefore, the total strength (integrated weight) of the self-energy depends on the fluctuations of the phonon field.

3. FORMALISM FOR THE PHONONIC SUM RULES

The retarded phonon Green's function is defined in a similar way, via

$$D^R_{ij}(t, t') = -i\theta(t - t')\text{Tr}e^{-\beta\mathcal{H}(t_{min})}\left[x_i(t), x_j(t')\right]_-/\mathcal{Z}, \tag{19}$$

with the operators in the Heisenberg representation. The moments are defined in the same way as before. First, one converts to the average and relative time coordinates and Fourier transforms with respect to the relative coordinate:

$$D^R_{ij}(t_{ave}, \omega) = \int_0^\infty dt_{rel}e^{i\omega t_{rel}}D^R_{ij}\left(t_{ave} + \frac{1}{2}t_{rel}, t_{ave} - \frac{1}{2}t_{rel}\right), \tag{20}$$

and then one computes the moments via

$$m^{Rn}_{ij}(t_{ave}) = -\frac{1}{\pi}\int_{-\infty}^\infty d\omega\,\omega^n\text{Im}D^R_{ij}(t_{ave}, \omega). \tag{21}$$

The zeroth moment vanishes because x_i commutes with itself at equal times. For the higher moments, we also derive a formula similar to what was used for the electronic Green's functions. In particular, we have

$$m^{R1}_{ij}(t_{ave}) = -\frac{1}{2}\text{Im}\left\{\left\langle\left[x_i'(t_{ave}), x_j(t_{ave})\right]_-\right\rangle - \left\langle\left[x_i(t_{ave}), x_j'(t_{ave})\right]_-\right\rangle\right\} \tag{22}$$

for the first moment. But $x_i'(t_{ave}) = -i[x_i(t_{ave}), \mathcal{H}_H(t_{ave})]_- = p_i(t_{ave})/m$, so we find

$$m^{R1}_{ij}(t_{ave}) = \frac{1}{m}\delta_{ij}. \tag{23}$$

Similarly,

$$m_{ij}^{R2}(t_{ave}) = -\frac{1}{4}\text{Im}\,i\left\{\left\langle\left[x_i''(t_{ave}), x_j(t_{ave})\right]_-\right\rangle - 2\left\langle\left[x_j'(t_{ave}), x_j'(t_{ave})\right]_-\right\rangle\right.$$
$$\left. + \left\langle\left[x_i(t_{ave}), x_j''(t_{ave})\right]_-\right\rangle\right\}. \tag{24}$$

Using the fact that $x_i''(t_{ave}) = -i[p_i(t_{ave}), \mathcal{H}_H(t_{ave})]_- = -g(t_{ave})$ $\left(n_{i\uparrow}(t_{ave}) + n_{i\downarrow}(t_{ave})\right) - \kappa x_i(t_{ave})$, it can be shown that $m_{ij}^{R2}(t_{ave}) = 0$, since all the commutators vanish. We will not analyze the phonon self-energy in this discussion. Unlike the electronic moments, the phononic moments are much simpler and do not require any expectation values to evaluate them.

We end this section by showing that the imaginary part of the retarded phonon Green's function is an odd function of ω, which explains why all the even moments vanish. If one evaluates the complex conjugate of the retarded phonon Green's function, one finds

$$D_{ij}^R(t, t')^* = i\theta(t - t')\text{Tr}\left[x_j(t'), x_i(t)\right]_- e^{-\beta\mathcal{H}(t_{min})}/\mathcal{Z} = D_{ij}^R(t, t') \tag{25}$$

where the last identity follows by switching the order of the operators in the commutator and using the invariance of the trace under a cyclic permutation. Hence, the phonon propagator in the time representation is real. Evaluating the frequency-dependent propagator then shows that $D_{ij}^{R*}(t_{ave}, \omega) = D_{ij}^R(t_{ave}, -\omega)$ by taking the complex conjugate of Eq. (20). Hence the real part of the retarded phonon propagator in the frequency representation is an even function of frequency, while the imaginary part is an odd function of frequency; therefore, all the even moments vanish.

4. ATOMIC LIMIT OF THE HOLSTEIN MODEL

To get an idea of the phonon expectation values and the fluctuations, we now solve explicitly for the expectation values for the Holstein model in the atomic limit, where $t_{ij}(t) = 0$ and we can drop the site index from all operators. In this limit, one can exactly determine the Heisenberg representation operator $x(t)$ by solving the equation of motion for the Heisenberg representation operators $a(t)$ and $a^\dagger(t)$. This yields

$$x(t) = \frac{a e^{-i\omega t} + a^\dagger e^{i\omega t}}{\sqrt{2m\omega}} = 2\text{Re}\left\{ie^{-i\omega t}\int_0^t dt' e^{i\omega t'} g(t')\right\}\frac{n_\uparrow + n_\downarrow}{2m\omega}, \tag{26}$$

where the electronic number operators commute with $\mathcal{H}$ now, so they have no time dependence. Since the atomic sites are decoupled from one another, we can focus on just a single site. The partition function for a single site can be evaluated directly by employing standard raising and lowering operator identities. To begin, we note that the Hilbert space is composed of a direct product of the harmonic oscillator states

$$|n\rangle = \frac{1}{\sqrt{n!}} \left(a^\dagger\right)^n |0\rangle \tag{27}$$

and the fermionic states

$$|0\rangle, \quad |\uparrow\rangle = c_\uparrow^\dagger |0\rangle, \quad |\downarrow\rangle = c_\downarrow^\dagger |0\rangle, \quad |\uparrow\downarrow\rangle = c_\uparrow^\dagger c_\downarrow^\dagger |0\rangle. \tag{28}$$

The partition function satisfies

$$\mathcal{Z}_{at} = \sum_{0,\uparrow,\downarrow,\uparrow\downarrow} \sum_{n^b=0}^{\infty} \left\langle n^b, n^f \left| \exp\left[-\beta\left\{ (g(t_{min})x - \mu)\left(n_\uparrow^f + n_\downarrow^f\right) + \omega\left(n^b + \frac{1}{2}\right)\right\}\right]\right| n^b, n^f \right\rangle, \tag{29}$$

where n^f denotes the Fermi number operator and n^b the Boson number operator (we will drop the $\exp[-\beta\omega/2]$ term, which provides just a constant). Since the product states are not eigenstates of $\mathcal{H}$, we cannot immediately evaluate the partition function. Instead, we first need to go to the interaction representation with respect to the bosonic Hamiltonian in imaginary time (and drop the constant term from the Hamiltonian), finding that

$$\mathcal{Z}_{at} = \mathrm{Tr}_f \mathrm{Tr}_b e^{-\beta\omega n^b} \mathcal{T}_\tau \exp\left[-\int_0^\beta d\tau' \left\{\frac{e^{-\omega\tau'}a + e^{\omega\tau'}a^\dagger}{\sqrt{2m\omega}} g(t_{min}) - \mu\right\} n^f\right]$$
$$= \mathrm{Tr}_f \mathrm{Tr}_b e^{-\beta\omega n^b} U_I(\beta), \tag{30}$$

where the time-ordering operator $\mathcal{T}_\tau$ is with respect to imaginary time and the time-ordered product $U_I(\tau)$ is the evolution operator in the interaction representation. Because the only operators that don't commute in the evolution operator are a and $a^\dagger$, and their commutator is a c-number, one can get an exact representation for the evolution operator via the Magnus expansion (Magnus, 1954), as worked out by Landau and Lifshitz (1977) and Gottfried (1966). The result for the time-ordered product in Eq. (30) becomes

$$U_I(\beta) = \exp\left[-\frac{g(t_{min})n^f}{\sqrt{2m\omega^3}}\left(1 - e^{-\beta\omega}\right)a\right]\exp\left[-\frac{g(t_{min})n^f}{\sqrt{2m\omega^3}}\left(e^{\beta\omega} - 1\right)a^\dagger\right]$$
$$\times \exp\left[-\frac{g^2(t_{min})n^{f2}}{\sqrt{2n\omega^3}}\left(e^{\beta\omega} - 1 - \beta\omega + \mu n^f\right)\right], \tag{31}$$

which used the Campbell-Baker-Hausdorff theorem

$$e^{A+B} = e^B e^A e^{\frac{1}{2}[A,\,B]_-}, \tag{32}$$

for the case when the commutator $[A, B]_-$ is a number, not an operator, that can be used to get the final expression. We substitute this result for the evolution operator into the trace over the bosonic states, expand the exponentials of the a and $a^\dagger$ operators in a power series, and evaluate the bosonic expectation value to find

$$\mathcal{Z}_{at} = \mathrm{Tr}_f \sum_{m=0}^{\infty}\sum_{n=0}^{\infty}\frac{(n+m)!}{n!m!m!}\left(\frac{g^2(t_{min})n^{f2}}{2m\omega^3}\left(e^{\beta\omega} - 1 + e^{-\beta\omega} - 1\right)\right)^m$$
$$\times \exp\left[-\beta\omega n + \beta\mu n^f - \frac{g^2(t_{min})n^{f2}}{2m\omega^3}\left(e^{\beta\omega} - 1 - \beta\omega\right)\right]. \tag{33}$$

Next, we use Newton's generalized binomial theorem:

$$\sum_{n=0}^{\infty}\frac{(n+m)!}{n!m!}z^n = \frac{1}{(1-z)^{m+1}}, \tag{34}$$

to simplify the expression for the partition function to

$$\mathcal{Z}_{at} = \mathrm{Tr}_f \exp\left[\frac{\beta g^2(t_{min})n^{f2}}{2m\omega^2} + \beta\mu n^f\right]\frac{1}{1 - e^{-\beta\omega}}. \tag{35}$$

Performing the trace over the fermionic states then yields

$$\mathcal{Z}_{at} = \frac{1}{1 - e^{-\beta\omega}}\left\{1 + 2e^{\beta\mu}\exp\left[\frac{\beta g^2(t_{min})}{2m\omega^2}\right] + e^{2\beta\mu}\exp\left[\frac{2\beta g^2(t_{min})}{m\omega^2}\right]\right\}. \tag{36}$$

We calculate expectation values following the same procedure, but inserting the relevant operators into the Heisenberg representation at the appropriate place, and carrying out the remainder of the derivation as done for the partition function. For example, since the Fermi number operators commute with the atomic Hamiltonian, they are the same operator in the

Heisenberg and Schroedinger representations, and we immediately find that the electron density is a constant in time and is given by

$$\langle n_\uparrow + n_\downarrow \rangle = \frac{2e^{\beta\mu}\exp\left[\frac{\beta g^2(t_{min})}{2m\omega^2}\right] + 2e^{2\beta\mu}\exp\left[\frac{2\beta g^2(t_{min})}{m\omega^2}\right]}{1 + 2e^{\beta\mu}\exp\left[\frac{\beta g^2(t_{min})}{2m\omega^2}\right] + e^{2\beta\mu}\exp\left[\frac{2\beta g^2(t_{min})}{m\omega^2}\right]}. \tag{37}$$

We next want to calculate $\langle x(t) \rangle$ and $\langle x^2(t) \rangle - \langle x(t) \rangle^2$, where the operator is in the Heisenberg representation, and given in Eq. (26). It is straightforward, but tedious, to calculate the averages. After much algebra, we find

$$\langle x(t) \rangle = \langle n_\uparrow + n_\downarrow \rangle \left(-\frac{g(t_{min})}{m\omega^2}\cos\omega t - \mathrm{Re}\left\{ ie^{-i\omega t}\int_0^t dt'\, e^{i\omega t'}\frac{g(t')}{m\omega} \right\} \right). \tag{38}$$

Note that if we are in equilibrium, so that $g(t) = g$ is a constant, then one finds $\langle x(t) \rangle = -\langle n_\uparrow + n_\downarrow \rangle g/m\omega^2$, which has no time dependence, as expected. The fluctuation satisfies

$$\langle x^2(t) \rangle - \langle x(t) \rangle^2 = \left[\langle n_\uparrow \rangle(1 - \langle n_\uparrow \rangle) + \langle n_\downarrow \rangle(1 - \langle n_\downarrow \rangle) + 2\langle n_\uparrow n_\downarrow \rangle - 2\langle n_\uparrow \rangle\langle n_\downarrow \rangle \right]$$

$$\times \left[\frac{g(t_{min})}{m\omega^2}\cos\omega t + \mathrm{Re}\left\{ ie^{-i\omega t}\int_0^t dt'\, e^{i\omega t'}\frac{g(t')}{m\omega} \right\} \right]^2 \tag{39}$$

$$+ \frac{1}{2m\omega}\coth\left(\frac{\beta\omega}{2}\right),$$

which consists of two terms: a time-dependent piece (which becomes a constant when g is a constant) that represents the quantum fluctuations due to the electron-phonon interaction and a phonon piece that varies with temperature (and is independent of g). The latter piece becomes large when $T \to \infty$ (being proportional to T at high T), which tells us that fluctuations generically grow with increasing the temperature of the system, so that one expects the zeroth moment of the self-energy to increase as the temperature increases, or if the system is heated up by being driven by a large electric field. Note that if one expands the self-energy perturbatively, as in Migdal-Eliashberg theory, then only the term independent of g survives, as the other term is higher order in g and lies outside the Migdal-Eliashberg result (Kemper et al., 2014).

5. DISCUSSION AND APPLICATIONS OF THE SUM RULES

One of the most important recent experiments in electron–phonon interacting systems involves time-resolved angle-resolved photoemission (tr-ARPES), which can be analyzed in such a way that one can extract information about the electronic self-energy (Sentef et al., 2013; Kemper et al., 2014). If one assumes that the phonons form an infinite heat-capacity bath, then they are not changed by the excitation of the electrons, and the fluctuations of the phonon field remain a constant as a function of time. This leads to a self-energy that can transiently change shape as a function of time but does not change its spectral weight. Recent calculations show precisely this behavior (Sentef et al., 2013; Kemper et al., 2014). One can also understand it from the perturbation theory expansion, where a direct evaluation of the diagrams for self-energy and the sum rules for the electronic Green's functions establish that the zeroth moment of the retarded electronic self-energy is a constant (Kemper et al., 2014). What is perhaps more interesting is when one treats a fully self-consistent system where the electrons and phonons both can exchange energy with one another, and the phonon bath properties change transiently. In this case, one has to examine the self-consistency for both the electrons and the phonons within the perturbation theory, and the general form of the sum rules hold. The calculations shown previously in the atomic limit indicate that it is likely that adding energy to the phonon system increases the phonon fluctuations and thereby creates a stronger electronic self-energy. One would expect there to be oscillations of the spectral weight as well. It is also likely that these ideas can be incorporated into the quantitative analysis of experiments that we expect to see occur over the next few years.

6. CONCLUSIONS AND FUTURE WORK

In this work, we have shown the simplest sum rules for electrons interacting with phonons. These sum rules have been established in equilibrium for some time now, but our work shows that they directly extend to nonequilibrium as well. We also established new sum rules for the phonon propagator. In general, these rules are complicated to use because they require one to determine both the average phonon expectation value and its fluctuations, so they might find their most important application to numerics as benchmarking, assuming that one can calculate the relevant

expectation values with the numerical techniques employed to solve the problem. But they also allow us to examine the physical behavior we expect to see if we look at how the moments might change in time due to the effect of a transient light pump applied to the system. For example, we expect that as energy is exchanged from electrons to phonons, the electron self-energy should increase its spectral weight, with the opposite occurring as the phonons transfer energy back to the electrons. This result is not one that could have been easily predicted without the sum rules.

In the future, there are a number of ways that these sum rules can be extended. One can examine more realistic models, like the Hubbard-Holstein model, and find those sum rules. One can look into the effects of anharmonicity on the sum rules, and finally, one can carry out the calculations to a higher order to examine more moments. We plan to work on a number of these problems in the future.

ACKNOWLEDGMENTS

REFERENCES

Cortés, R., Rettig, L., Yoshida, Y., Eisaki, H., Wolf, M., & Bovensiepen, U. (2011). Momentum resolved ultrafast electron dynamics in superconducting $Bi_2Sr_2CaCu_2O_{8+\delta}$. *Physical Review Letters, 107*, 097002.

Freericks, J., & Turkowski, V. (2009). Inhomogeneous spectral moment sum rules for the retarded Green's function and self-energy of strongly correlated electrons or ultracold fermionic atoms in optical lattices. *Physical Review B, 80*, 115119.

Freericks, J., Turkowski, V., Krishnamurthy, H., & Knap, M. (2013). Spectral moment sum rules for the retarded Green's function and self-energy of the inhomogeneous Bose-Hubbard model in equilibrium and nonequilibrium. *Physical Review A, 87,* 013628.

Gottfried, K. (1966). *Quantum mechanics. Vol. 1: Fundamentals*. Reading, Mass: W. A. Benjamin.

Graf, J., Jozwiak, C., Smallwood, C. L., Eisaki, H., Kaindl, R., Lee, D., & Lanzara, A. (2011). Nodal quasiparticle meltdown in ultrahigh resolution pump-probe angle resolved photoemission. *Nature Physics, 7*, 805.

Holstein, T. (1959a). Studies of polaron motion. Part 1: The molecular-crystal model. *Annals of Physics (New York), 8*, 325.

Holstein, T. (1959b). Studies of polaron motion. Part 2: The "small polaron." *Annals of Physics (New York), 8*, 343.

Kemper, A., Sentef, M., Moritz, B., Freericks, J., & Devereaux, T. (2014). Effect of dynamical spectral weight redistribution on effective interactions in time-resolved spectroscopy. *Physical Review B*, *90*, 075126. http://dx.doi.org/10.1103/PhysRevB.90.075126.

Kornilovitch, P. (2002). Photoemission spectroscopy and sum rules in dilute electron-phonon systems. *Europhysics Letters, 59*, 735.

Landau, L., & Lifshitz, L. (1977). *Quantum mechanics (nonrelativistic theory)*. 3rd. Ed. Burlington, Mass: Elsevier Butterworth-Heinemann.

Magnus, W. (1954). On the exponential solution of differential equations for a linear operator. *Communications on Pure and Applied Mathematics, 7*, 649.

Peierls, R. (1933). Theory of diamagnetism of conduction electrons. *Zeitschrift für Physik, 80*, 763.

Rösch, O., Sangiovanni, G., & Gunnarsson, O. (2007). Sum rules and vertex corrections for electron–phonon interactions. *Physical Review B, 75*, 035119.

Sentef, M., Kemper, A., Moritz, B., Freericks, J., Shen, Z., & Devereaux, T. (2013). Examining electron-boson coupling using time-resolved spectroscopy. *Physical Review X, 3*, 041033.

Turkowski, V., & Freericks, J. (2006). Spectral moment sum rules for strongly correlated electrons in time-dependent electric fields. *Physical Review B, 73*, 075108.

Turkowski, V., & Freericks, J. (2008). Nonequilibrium sum rules for the retarded self-energy of strongly correlated electrons. *Physical Review B, 77*, 205102.

Molecular Structural Dynamics Unveiled by Time-Resolved X-ray Solution Scattering

H. Ihee

Korea Advanced Institute of Science & Technology (KAIST) and Institute for Basic Science (IBS), Daejeon, South Korea

Time-resolved X-ray solution scattering (liquidography) is an excellent tool for directly probing the structural dynamics of chemical and biological reactions occurring in solution phase. A unique combination of structural sensitivity and superb time resolution of this technique enables characterization of transient structures of reacting molecules in solution. Over the last decade, we have applied this technique to various molecular systems in solution phase and have successfully elucidated the dynamics and structural details of those reactions (Ihee, 2009; Ihee et al., 2005; Cammarata et al., 2008a,b; Lee et al., 2013; Kim et al., 2013). TRXL (time-resolved X-ray liquidography) can provide direct structural information that is generally difficult to extract from ultrafast optical spectroscopy, such as the temporal progression of bond lengths and angles of all molecular species, including short-lived intermediates over a wide range of times, from picoseconds to milliseconds. TRXL elegantly complements ultrafast optical spectroscopy because diffraction signals are sensitive to all chemical species simultaneously and the diffraction signal from each chemical species can be quantitatively calculated from its three-dimensional atomic coordinates and compared with experimental TRXL data. Representative application examples, including spatiotemporal kinetics and structural dynamics of small molecules and proteins, will be presented.

REFERENCES

Cammarata, M., Levantino, M., Schotte, F., Anfinrud, P. A., Ewald, F., Choi, J., et al. (2008a). Erratum: Tracking the structural dynamics of proteins in solution using time-resolved wide-angle X-ray scattering. *Nature Methods, 5*, 988.

Cammarata, M., Levantino, M., Schotte, F., Anfinrud, P. A., Ewald, F., Choi, J., et al. (2008b). Tracking the structural dynamics of proteins in solution using time-resolved wide-angle X-ray scattering. *Nature Methods, 5*, 881–886.

Ihee, H. (2009). Visualizing solution-phase reaction dynamics with time-resolved x-ray liquidography. *Accounts of Chemical Research, 42*, 356–366.

Ihee, H., Lorenc, M., Kim, T. K., Kong, Q. Y., Cammarata, M., Lee, J. H., et al. (2005). Ultrafast X-ray diffraction of transient molecular structures in solution. *Science, 309*, 1223–1227.

Kim, K. H., Lee, J. H., Kim, J., Nozawa, S., Sato, T., Tomita, A., et al. (2013). Solvent–dependent molecular structure of ionic species directly measured by ultrafast X–ray solution scattering. *Physical Review Letters, 110*, 165505–165509.

Lee, J. H., Wulff, M., Bratos, S., Petersen, J., Guerin, L., Leicknam, J.–C., et al. (2013). Filming the birth of molecules and accompanying solvent rearrangement. *Journal of the American Chemical Society, 135*, 3255–3261.

An X-Band Photoelectron RF Gun for an Ultrafast Electron Diffraction Source

C. Limborg-Deprey, C. Adolphsen, D. McCormick, M. Dunning, E. Hemsing, K. Jobe, H. Li, T. Raubenheimer, T. Vecchione, A. Vrielink, F. Wang, S. Weathersby
SLAC National Accelerator Laboratory, California, USA

Abstract

The ability to operate X-band radio frequency (RF) photoelectron guns at very high gradients makes them very attractive electron sources for ultrafast electron diffraction (UED) experiments. The X-band (11.4-GHz) injector recently commissioned at SLAC demonstrates 200 MV/m peak cathode field operation in a photoelectron RF gun and confirms that high beam quality is achievable. Bunch lengths as short as 120 fs rms have been measured for charges of 5 pC ($\sim 3.10^7$ electrons) out of the gun, with a normalized transverse emittance of 0.45 mm-mrad. Bunch lengths as short as 400 fs rms have been measured for electron bunches of 100 pC ($\sim 6.10^8$ electrons) with a normalized emittance of 0.8 mm-mrad. In this paper, we discuss how RF photoelectron guns operating at very high gradients can meet the demand for short and well-synchronized electron bunches for UED experiments. In particular, we demonstrate that our gun can produce a 25-fs-rms-long bunch with a 30-fC charge ($\sim 2.10^5$ electrons) synchronized to a pump laser at the 25-fs-rms level to perform UED pump-probe experiments.

Keywords: RF gun, high gradient, photocathode, MeV electron, fs pulse, time of flight, fs synchronization, small electron emittance

1. INTRODUCTION

High-brightness electron sources are being actively developed by the accelerator community to provide electron beams with properties suited to drive linac based free electron lasers (FELs) (Akre et al., 2008; Emma et al., 2010). The preferred choice has been to use RF photoelectron guns as they provide the charge (tens to hundreds of pC per bunch), relatively short electron bunches (on the order of picoseconds), and brightness (100 A/mm–mrad^2) needed to drive an FEL. In an RF photoelectron gun, the spatial–temporal shape of the laser pulse hitting the photocathode is transferred to the emitted electron bunch. This is valid for laser pulses of at least a few hundred fs with a radius of a few hundred μm as is typically used. The emission out of the copper cathode happens on a much shorter timescale (less than a femtosecond) than the laser pulse duration (a few tens to

hundreds of femtoseconds). In the RF photoelectron gun, a high-gradient acceleration field, with tens to hundreds of MV/m electric fields, boosts the electron beam very rapidly to relativistic velocities. At relativistic velocities, the defocusing induced by strong coulomb forces between electrons or space charge forces is countered by the magnetic field induced by the electron bunch current flow. The resulting defocusing force scales as $1/\gamma^2$, where γ is the relativistic Lorentz factor, the ratio of electron energy to rest mass.

The brightness out of a state-of-the-art RF photoelectron gun is 11 orders of magnitude lower than the ultimate quantum limit (Luiten et al., 2007; Zolotorev et al., 2007). However, RF photoelectron guns remain the only electron sources which can provide a very large number of electrons (10^7) for sub-100 fs rms pulse durations. This technology also allows one to control the arrival time of the electron bunch on a sample to within tens of fs after a pump laser has triggered the reaction to be studied dynamically.

The X-band test area (XTA) at SLAC was initially designed to test X-band RF photoelectron guns for compact FELs (Sun et al., 2012), and compact inverse Compton scattering sources (Marsh et al., 2012). In this paper, we discuss its potential as a source for UED experiments. RF photoguns operating at S-band RF frequencies have been commonly used since MeV electron diffraction was first demonstrated experimentally (Hastings et al., 2006). Calculations indicate that the maximum peak brightness from an X-band gun with an RF frequency of 11.424 GHz and a peak acceleration field of 200 MV/m is a factor of 8 larger than that from the standard S-band technology, where the gun typically operates at 2.856 GHz with a peak acceleration field of 120 MV/m. This improvement comes from a reduction of the bunch length by a factor of 3 to 4 and from a reduction in the product of the horizontal and vertical emittances for another factor of about 2. These improvements are the result of the higher peak gradient achievable in higher RF frequency sources and are of major interest to the UED community.

The first part of the paper describes the beam dynamics of electron bunches in an X-band photogun and how it differs from that in an S-band photogun. We quantify how short electron bunch duration can be for different charge levels and the implications for the transverse emittances. Having compared theoretical predictions with measurements for electron bunches in the range of 5 pC ($\sim3.10^7$ electrons) to 300 pC ($\sim1.8.10^9$ electrons), we claim that our gun alone, with no other RF components, can produce bunches with 25 fs rms duration, with as much as 30 fC ($\sim2.10^5$ electrons) for use in single-shot UED experiments.

To take advantage of 25-fs-rms-long electron bunches in single shots, one needs to synchronize the electron bunch arrival time with respect to the pump laser to better than 25 fs. In the second part of the paper, we describe calculations demonstrating how to optimize the gun and the RF system to meet the 25-fs stability requirement. In particular, we report on measurements of electron bunch time-of-flight (TOF) performed on our gun. The present stability of the RF system is such that the arrival time of the electron bunch fluctuates by no more than 50 fs when referenced to the laser that is used on the photocathode for photoemission of electrons. As such, our source can be used as a pump for UED experiments and deliver temporal resolution as good as 50 fs. With some improvements to our klystron modulator stability and on our laser oscillator to operation levels that have already been done elsewhere, our system could reach 25 fs rms.

It had been feared that operation at high gradient would not be compatible with low-charge operation. Indeed, since gradient fields decrease the Schottky barrier, large amounts of undesired electrons are emitted at the cathode in the presence of high fields. This is aptly named *dark current emission,* and its amount increases rapidly with field gradient amplitude. However, at X-band, the RF pulse duration needed to fill the RF cavities is fortunately much shorter than for lower-frequency RF accelerator structures; thus, the amount of dark current generated stays within an acceptable limit that is compatible with operation at low charges. We claim that the levels of dark current measured from our X-band gun are compatible with 30-fC photoelectron bunches. This and the timing stability make our system very competitive with the best instruments available for pump–probe experiments in need of sub–100-fs temporal resolution (Grguras et al., 2012).

The XTA beamline includes an X-band RF photoelectron gun, a 1-m-long X-band linac and diagnostics to measure the brightness of the beam. The beam properties are evaluated at high energy, 75–85 MeV, where the measurements are not affected by space charge effects. A schematic of the beamline is given in Figure 1.

2. GENERATION OF SHORT BUNCH LENGTHS FROM AN X-BAND RF PHOTOELECTRON GUN

The construction of the Linac Coherent Light Source (LCLS) (Emma et al., 2010), the first X-ray laser worldwide, led to the development of high-performance S-band RF photogun electron sources. S-band RF photogun technology had matured after years of combined efforts in multiple
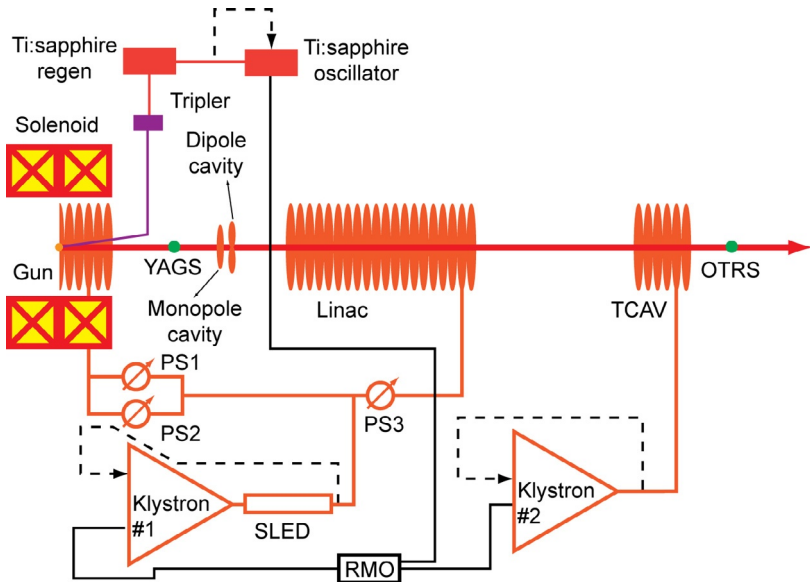
Figure 1 Schematic of the XTA experiment. PS1, 2, and 3 are phase shifters, YAGS is an yttrium aluminum garnet screen, OTRS is an optical transition radiation screen, TCAV is an X-band deflecting cavity, and RMO is the RF master oscillator.

laboratories and countries (Fraser et al., 1985; Limborg et al., 2005; Serafini & Rosenzweig, 1997). The design and fabrication of a first X-band RF photogun was done at SLAC on the same timescale (Vlieks et al., 2006) and benefited from 16 years of development of the X-band technology for the Next Linear Collider (Adolphsen, 2005). The gun presently in operation at the XTA is an upgraded version of the initial design (Vlieks).

2.1 Comparative Study of Longitudinal Beam Properties for S-Band and X-Band Guns

2.1.1 Single Particle Dynamics

Figure 2 shows the calculated increase in electron energy (expressed by γ) during the first 33 ps of acceleration, where the beam travels close to 3 mm after the cathode, for both an S-band gun operated with a 120-MV/m cathode field and an X-band gun operated with a 200-MV/m field, which are near the upper limit for reliable operation at these frequencies. Those field values are used in the following description unless explicitly specified. As described by Kim (1989), the space charge force has a $1/\gamma^2$
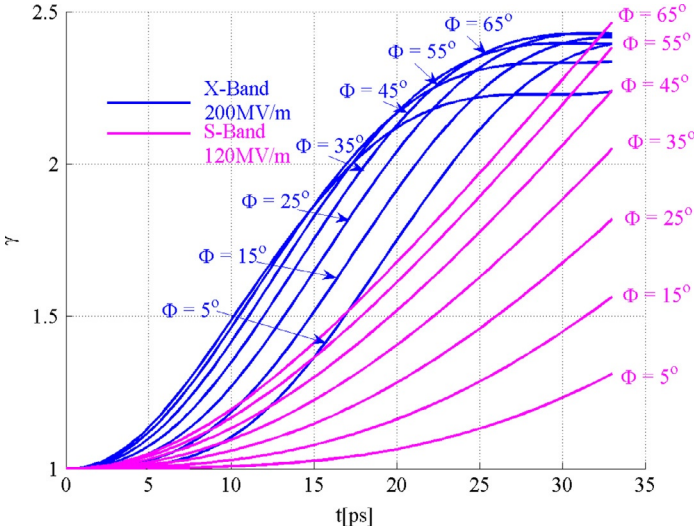
Figure 2 Evolution of γ with time for a single electron in a 200 MV/m X-band gun (blue) and 120 MV/m S-band gun (magenta) for different initial RF phases.

dependency and the primary detrimental space charge effects occur in the region where γ is smaller than 2. For this comparison, γ reaches 2 twice as rapidly in the X–band case.

2.1.2 Bunch Length in the Presence of Space Charge

Due to the rapid increase in γ, the bunch length gets frozen between 1 and 3 mm downstream of the cathode, with the approximate value of 1 mm for the low-space charge and 3 mm for the high-space charge regimes. For negligible or low-space charge, the electron bunch length depends strongly on the initial laser phase and final bunch lengths are similar for X-band and S-band. The electron bunch is compressed with respect to the initial laser pulse length. Stronger compression is obtained for lower phases. Lower phases are defined as closer to the field cancellation phase (i.e., zero-crossing). For intermediate space charge levels, the beam in an X-band gun still behaves similarly as in the low-space charge regime (i.e., with compression but now moderate), whereas the beam in the S-band gun already behaves as in the high-space charge regime. In the high-space charge regime, no more compression is achieved. Higher laser phases now give smaller bunches as the freezing process is more efficient when the cathode field is closer to maximum since higher phases mean closer to crest. Accordingly, the X-band gun is better at fighting space charge early, and we thus obtain

bunch lengths which are 2 to 4 times shorter than for the S–band gun for similar laser spot sizes. Notice that the high field present in the X–band gun also allows beating the space charge limit and operating at higher charges for smaller laser spot sizes. The space charge limit equation, which is the direct description of Gauss's law, is written here as Eq. (1), where E is the cathode field, Q the charge, and r the laser spot radius:

$$E = \frac{\sigma}{\varepsilon_o} = \frac{Q}{\varepsilon_o \pi r^2}. \tag{1}$$

With operation at twice the cathode field, the spot size radius can be reduced by the square root of 2, and thus the emittance can be reduced by the same amount. However, this scaling only applies for small spot sizes. For higher charges and larger spot sizes, nonlinear effects in the X–band gun get stronger than for the S–band gun, which leads to transverse emittance degradation. The emittance then does not scale with r_{laser} anymore.

Note that the straight application of Eq. (1) is valid so long as the aspect ratio of the laser pulse is similar to that of a pancake. For a time-elongated laser profile (the so-called cigar shape), the space charge limit can be violated (Filippetto et al., 2014; Li et al., 2012).

To illustrate how the final bunch length varies with initial laser phase and laser dimensions, calculations were performed using ASTRA (Floettmann, n.d.) for the case of 30 fC. With a goal of 25-fs-rms resolution, the X–band gun performances are better than that out of the S–band gun since a laser spot size as small as 25 μm (equivalent to an 11–nm transverse emittance) can be used. If run for a similar transverse emittance, the S–band gun provides bunch lengths no less than 42 fs rms. The curves in Figure 3 illustrate the three regimes described earlier. The magenta curves correspond to low-space charge, the blue and red to moderate space charge, and the green ones to high-space charge.

2.2 Bunch Length as a Function of Charge

The minimum bunch length as a function of charge for the X–Band gun operated at 200 MV/m has been calculated with the multiparticle tracking codes ASTRA and GPT (Floettmann, n.d.; van der Geer & de Loos, n.d.). In Figure 4, electron bunch lengths are given at 0.2 m from the cathode; i.e., 0.1 m downstream of the gun exit. For each charge, the RF phase was optimized to give the minimum bunch length. As described earlier, the phases are low (near the zero crossing) for the low-space charge regime and high for
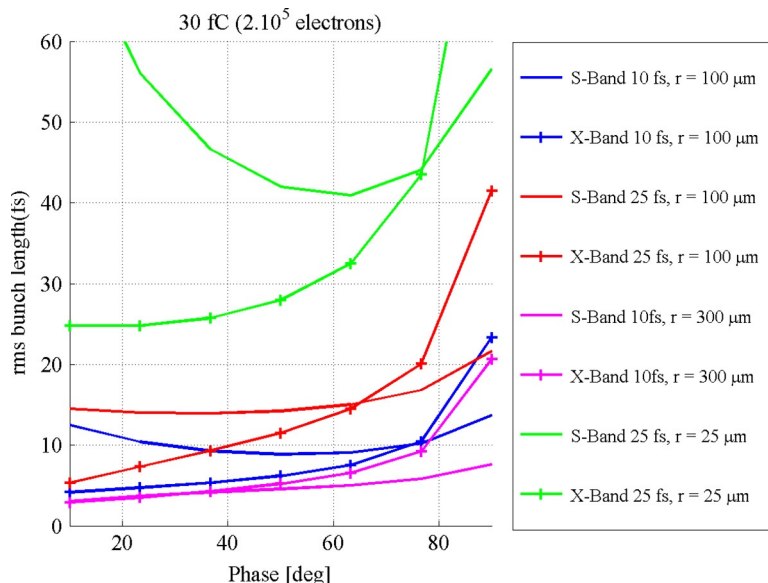
Figure 3 RMS bunch length versus laser-to-RF phase for different laser pulse durations and spot sizes, but a fixed 30-fC charge calculated at 0.2 m from the cathode.
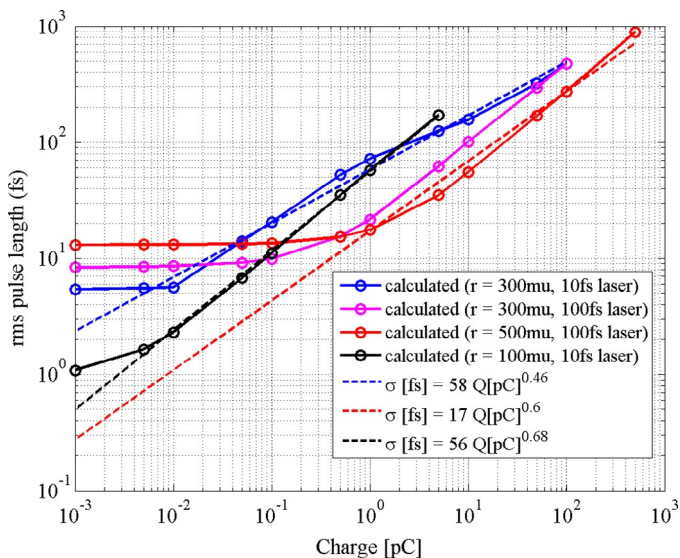

Figure 4 Calculated bunch lengths at a distance of 0.2 m from the cathode for the 5.5-cell X-band gun in operation at the XTA.

the high–space charge regime. The calculation was repeated for different laser pulse lengths and transverse sizes. The high–space charge regime exhibits a strong variation of bunch length with charges as expected. The power law, which fits the bunch length as a function of charge, has coefficients that vary from 1/3 to 2/3 depending on the initial laser pulse dimensions. The scaling law derived in Rosenzweig and Colby (1995) has a 1/3 power dependence when the charge density stays constant. The highest charge that can be accelerated off the cathode depends on the laser spot size, as described in Eq. (1), where E is the cathode gradient.

In low–space charge regimes, the electron bunch length is independent of the charge but is determined by the initial laser pulse. For a larger spot size, and a charge lower than 100 fC, the bunch length is longer for a larger spot size. This comes from the radial dependency of the accelerator field combined with the velocity bunching. For the same spot size, but shorter laser pulse, shorter bunch lengths are obtained due to the smaller velocity spread.

Figure 5 shows the bunch length as a function of charge at a distance of 0.7 m from the cathode, where the solenoid has been set to a value of 5.7 kG, which is appropriate for high charges for transverse emittance
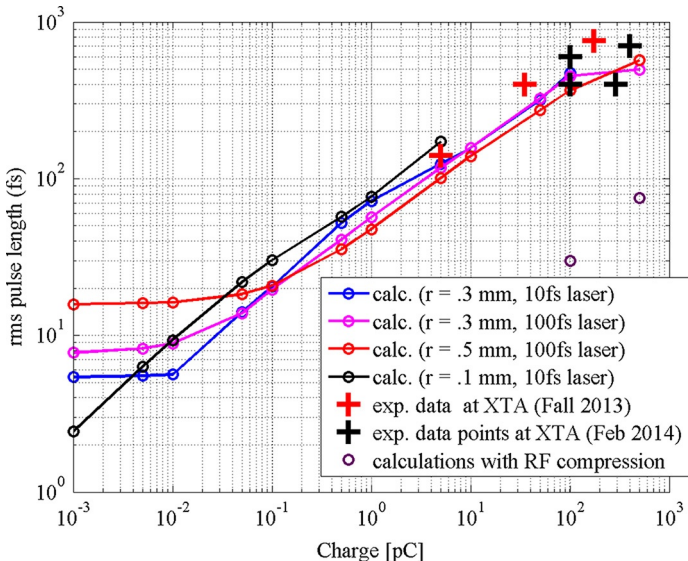
Figure 5 Calculated bunch lengths at 0.7 m from the cathode for the 5.5-cell gun in operation at the XTA.

preservation when accelerated in a linac. This strong transverse focusing induces high–space charge and the bunch starts lengthening again before the bunch reaches the linac.

In the high–space charge regime, the final bunch length becomes quasi-independent of the initial laser pulse dimensions. Bunch length measurements performed at the XTA have been superimposed, which will be presented next.

2.3 Bunch Length Measurements at XTA

These measurements are made using an X-band transverse deflector (TCAV), which is powered by a separate RF station. The deflector gives an angular kick in the vertical plane, which results in a vertical displacement Δy further downstream. This Δy displacement is linear with the electron position, z, along the bunch when the deflector is operated at the zero-crossing phase. This displacement depends on the vertical betatron functions β_{TCAV} at the TCAV and β_{OTR} at the observation point (OTR screen in this case) and on the phase advance between them, ψ.

The beam size at the screen is then

$$\sigma^2_{y,tot} = \varepsilon \beta_{OTR} + \beta_{Tcav} \beta_{OTR} \left[\frac{eVo}{pc} \sin \psi_{Tcav->OTR} \left(\frac{2\pi}{\lambda} \right) \right]^2 \sigma^2_z. \qquad (2)$$

The first term of the r.h.s. of Eq. (2) can be determined by switching the deflector off [as seen in Figure 6(B)]. We then vary the phase of the deflector to calibrate the screen length scale to degrees of X-band, and thus determine the coefficient in factor of z on the r.h.s. of Eq. (2). A calibration example is shown in Figure 6(C). From this information, the "streaked" beam [as shown in Figure 6(A)] can be used to compute the bunch length using Eq. (2).

This procedure was followed to determine the bunch lengths shown in Figure 6. In particular, the red-cross data points were measured for an electron beam generated using a laser pulse with a 60-fs FWHM duration and spot diameter of 2 mm. They agree with simulations fairly well.

A data point in Figure 6 of particular interest for UED is the one at 5 pC ($\sim 3.10^7$ electrons), at which charge a 125-fs-rms-long bunch was measured. S-band injectors can achieve such short bunches using an S-band photocathode RF gun, but they require an additional RF accelerator for compression, as in van Oudheusden et al. (2010). The bunch length measured in van
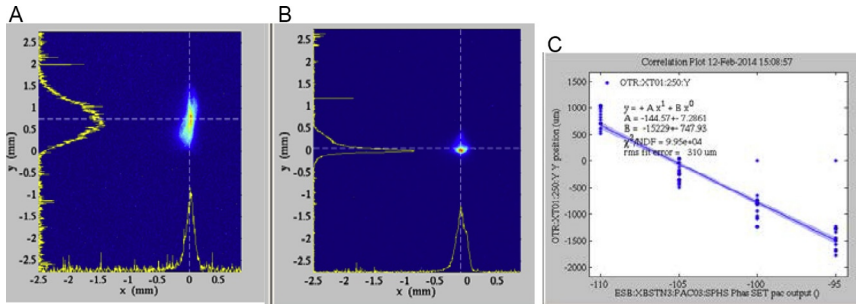
Figure 6 (A) Streaked beam, (B) beam with the deflector off, and (C) calibration curve: position versus TCAV phase.

Oudheusden et al. (2010) also corresponded to a much lower charge of 200 fC. Our 10-cm-long photocathode X-band RF gun alone suffices to reach such performances at 5 pC.

The second series of measurements was performed with the goal of maximizing the peak current (black crosses in Figure 5). Our best result of 270 A with 290 pC in a 460-fs bunch length was reproduced on several occasions. Higher peak currents are expected to be measured for even higher charges. The gun has emitted up to 1 nC ($\sim 6.10^9$) photoelectrons so far despite a quantum efficiency in the low 10^{-5} scale. No attempt to optimize for more than 400 pC has been made yet.

Simulations and experimental data agree well between 5 pC and 300 pC for our X-band gun. We thus anticipate that the 25-fs-rms length for 2.10^5 electrons could be easily achieved with our gun, as predicted with simulations. In the second part of this paper, we study how the arrival time of the short electron bunch can be synchronized to better than 25 fs to the pump laser for a UED experiment.

3. TIME RESOLUTION FOR UED EXPERIMENTS USING AN X-BAND RF PHOTOELECTRON GUN

3.1 Requirements to Achieve Temporal Resolution of 25 fs

For a time-resolved optical/electron pump-probe diffraction experiment to be performed with our X-band gun at XTA, we believe that we can already control the probe electron bunch arrival time with respect to the pump laser pulse to a 50-fs-rms level and reach a $\sim$25-fs-rms level by implementing upgrades already tested in other places at SLAC.

3.1.1 Time-of-Flight Variation with RF Field Fluctuations

A single laser is used for both the electron beam generation on the photo-cathode and the optical pump for the experiment. The arrival time thus does not depend directly on the laser jitter but on the pulse-to-pulse variation of the beam transit time from the cathode to the experiment. This in turn depends on the RF-to-laser timing jitter at the cathode and variations in the RF amplitude. For our klystron, which has modulator voltage fluctuation of 300 ppm rms, the predicted rms amplitude jitter is 0.1% and the rms phase jitter is 0.5 deg relative to the RF master oscillator reference. On the best days, values of 0.05% in rms amplitude and 0.3 deg in rms phase have been measured. Added to this phase jitter is the laser to RF reference jitter, and overall, an RF-to-laser jitter of 0.6 deg (150 fs) has been measured.

In Figure 7, changes in the time of flight (TOF) due to changes in the RF field amplitude as calculated with GPT (van der Geer & de Loos, n.d.) are shown for both 5.5 cell X-band and 1.6 cell S-band guns, respectively, at their nominal operating voltages of 200 MV/m and 120 MV/m and phases Φ_o, relative to zero-crossing, of 50 deg and 30 deg. The TOFs vary by 19.1 fs and 32 fs, respectively, for the X-band and S-band guns for a field variation of 0.1%.
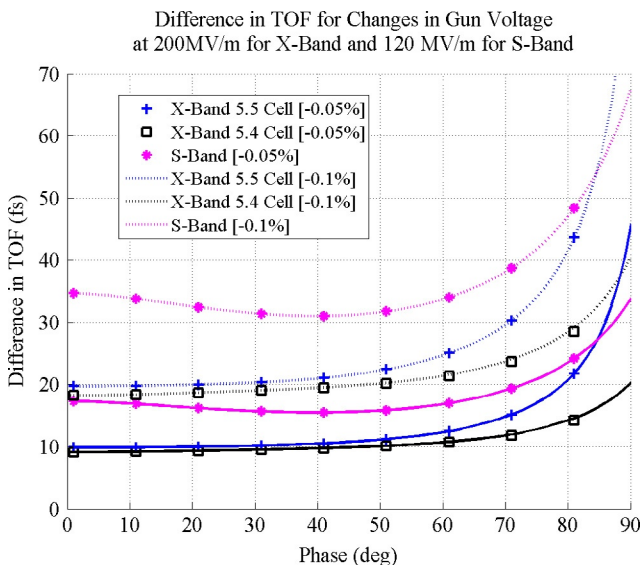
Figure 7 Relative difference of TOF for different changes in the gun gradient (either 0.05% or 0.1%) computed 0.7 m from cathode as a function of the relative laser phase to RF phase.

3.1.2 TOF Variation with Laser-to-RF Timing Jitter

In Figure 8(A), three plots are shown that illustrate the TOF sensitivity to the laser–to–RF timing for different guns and cathode gradients. One can see that the phase Φ_{TOF} at which the TOF is minimal does not automatically coincide with the phase Φ_o, giving the maximum energy as shown in Figure 8(B). One usually operates the RF at maximum energy to minimize the energy spread along the bunch and thus better preserve the transverse emittance. For the 5.5 cell X–band gun operated at 200 MV/m, Φ_{TOF} is
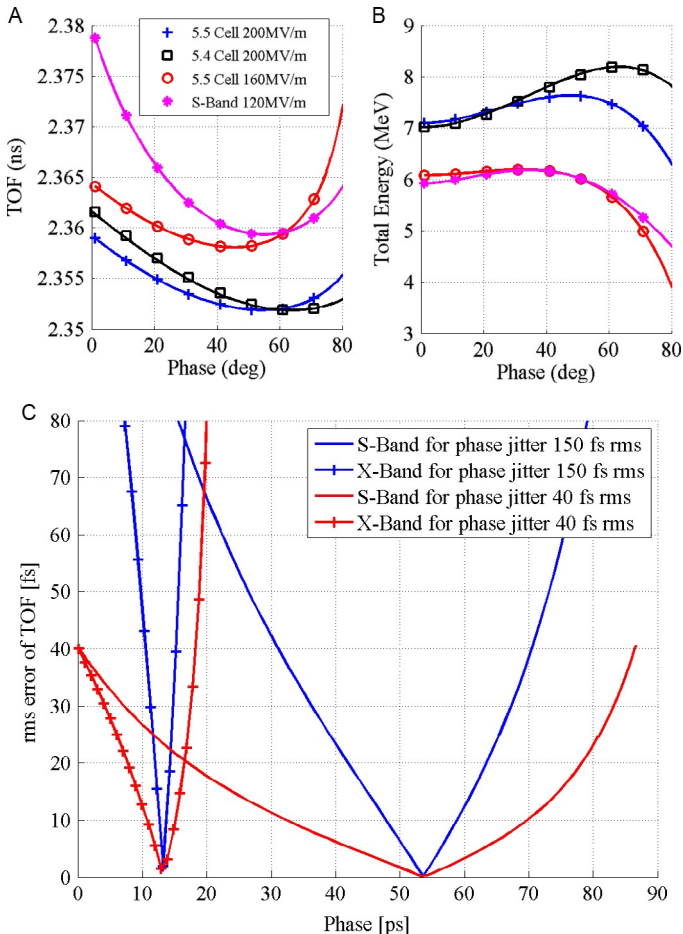
Figure 8 (A) TOF versus the laser to RF phase 0.7 m from cathode for a 0.25 deg for different guns and cathode gradients. (B) beam energy versus the laser to RF phase 0.7 m (C) RMS TOF errors for a laser-to-RF phase jitter of 150 fs and 40 fs for both guns operated at their nominal gradients.

55 deg, as opposed to 50 deg for Φ_o. For the 1.6 cell S–band gun operated at 120 MV/m, Φ_{TOF} is 55 deg, as opposed to 30 deg for Φ_o. Note that a 5.4 cell X–band gun and a 1.4 cell S–band operating at 200 MV/m and 120 MV/m, respectively, have Φ_{TOF} and Φ_o identically high at 65 deg, which is advantageous for high–cathode peak field at emission and good temporal stability. A version of 1.4 cell gun was recently discussed (Li & Musumeci, 2014).

In Figure 8(C), the rms error of the TOF was calculated for the two guns operated at their nominal field and for two different laser to RF rms phase errors over a range of 90 deg. The phase has been converted in absolute time in Figure 8(C). An X–band deg (250 fs) is 4 times shorter than an S–band deg (1 ps). The first set of data corresponds to an rms error of 150 fs, which is typical of a combination of 125 fs measured on our laser oscillator output pulse with a signal source analyzer and 83 fs (0.3 deg) measured for our RF phase jitter. The other two curves correspond to 40 fs, which we consider the best-scenario case, in which the laser oscillator jitter is reduced to 30 fs and the RF phase jitter is reduced to 25 fs (0.1 deg). A laser jitter at that level has been achieved at SLAC by doing the laser phase locking at 3.808 GHz. RMS RF phase jitter of 0.1 deg has been achieved with X–band RF systems operating with solid-state-based modulators. In all cases, less than 5 fs rms error in TOF can be achieved. However, the range of phases for which this condition is met is much wider for the S–band gun and thus more easily reached and maintained.

3.2 Time-of-Flight Measurements at XTA

The TOF is measured using an X–band phase cavity located before the accelerator structure. It is a monopole TM010 mode cavity resonating at 12.85 GHz. The frequency was chosen to be offset from 11.424 GHz so as not to "see" dark current and to allow locking to the master oscillator with "simple" RF multiply/divide steps. The TOF measurements are summarized in Figure 9 and were measured at different output power levels. A single particular measurement performed at 150 MW SLED output power is shown in more details in Figure 10. In each case, the beam–to–RF reference phase difference is plotted as a function of the laser-to-RF phase difference.

TOF measurements to determine the energy of electron beams are usually performed at low energy (i.e. a few hundred keV), but not for MeV beams, as done here. In our case, the energy varies between 4 and 7 MeV depending on power level and injection phase. One can fit the curve with calculated TOF to
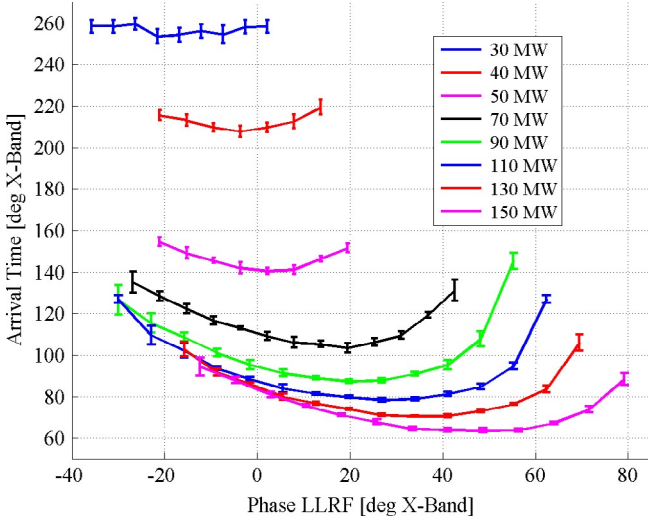
Figure 9 TOF measurements for different RF power levels. The arrival time has been converted from a 12.85-GHz phase to an 11.424-GHz phase. Phases on the left correspond to phases close to the zero crossing. The absolute phase differences have an arbitrary offset for each power.
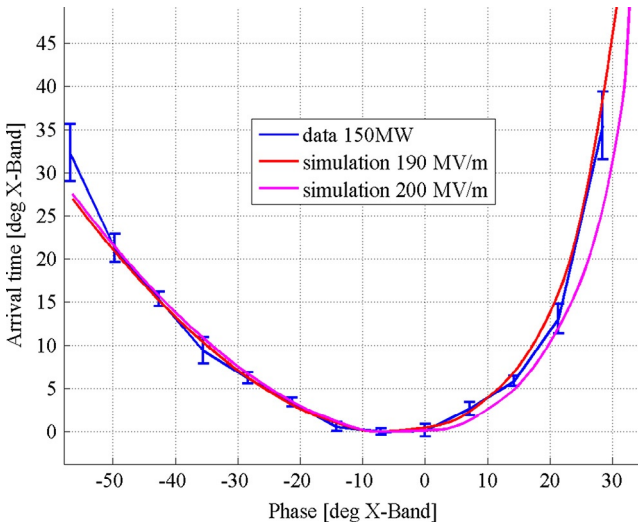

Figure 10 TOF measurements compared with model results for 150 MW.

infer the peak cathode field as presented in Figure 10. The peak field can be determined with 5% accuracy.

The statistics over 50 shots recorded in the error bars show that for the minimum TOF, the fluctuations can be as small as 0.6 X-band deg rms (i.e., 150 fs). This fluctuation is measured with respect to the RF clock and includes noise in the electronics processing the signal. This value is dominated by laser phase jitter of the oscillator output, as already described.

4. CONCLUSION

The X-band photoinjector being commissioned at SLAC has great potential as a source for electron diffraction experiments aimed at solving dynamic problems for timescales below 100 fs. Electron bunch lengths as short as 125 fs rms have been measured for charges of 5 pC ($\sim 3.10^7$ electrons). The system could produce 30 fC ($\sim 2.10^5$ electrons) bunches with pulse duration of 25 fs rms and arrival time stability better than 25 fs rms with respect to a pump laser, exceeding by far the present performances of any instrument designed to perform UED experiments. This could be achieved by reducing the oscillator timing jitter from its present 125 fs to 30 fs, a value already demonstrated on some other laser systems at SLAC. This would also require using a solid-state-based modulator. One such modulator is already present in the building where the X-band test area is located. The best beam performances described in this paper assume operation at a peak field gradient of 200 MV/m. For such high-gun field gradients, the dark current level is large, but we believe that we could collimate and energy filter it by installing a short decelerating cavity. This decelerating cavity would bring the energy down from 7.5 MeV to 5 or 3 MeV. This short linac would act in a similar fashion as our present accelerator structure, which reduces the dark current to 20 pC over the 150-ns-long RF pulse. To detect the 30 fC ($\sim 2.10^5$ electrons) in the UED experiment, we would also use cameras with 200-ps gates for the detection system.

The class of UED experiments in need of very short and intense electron bunches but tolerating a total energy spread as high as 1% could be performed in a facility combining an X-band gun and an X-band RF compressor. Bunches with 1 pC ($\sim 6.10^6$ electrons) charge, 7 fs rms duration, and less than 1% total energy spread at 5 MeV can be achieved according to simulations. Beam performances for such a configuration will be tested experimentally at the XTA.

REFERENCES

Adolphsen, C. (2005). Advances in normal conducting accelerator technology from the X-Band linear collider program. *SLAC-PUB-11224*. http://www.slac.stanford.edu/cgi-wrap/getdoc/slac-pub-11224.pdf.

Akre, R., Dowell, D., Emma, P., Frisch, J., Gilevich, S., Hays, G., et al. (2008). Commissioning the Linac coherent light source injector. *Physical Review Special Topics—Accelerators and Beams, 11*, 030703.

Emma, P., Akre, R., Arthur, J., Bionta, R., Bostedt, C., Bozek, J., et al. (2010). First lasing and operation of an angstrom-wavelength free-electron laser. *Nature Photonics, 4*, 641–647.

Filippetto, D., Musumeci, P., Zolotorev, M., & Stupakov, G. (2014). Maximum current density and beam brightness achievable by laser-driven electron sources. *Physical Review Special Topics—Accelerators and Beams, 17*, 024201.

Floettmann, K. (n.d.). ASTRA. http://www.desy.de/~mpyflo/.

Fraser, J. S., Sheffield, R. L., Gray, E. R., & Rodenz, G. W. (1985). High-brightness photoemitter injector for electron-accelerators. *IEEE Transactions on Nuclear Science, 32*, 1791–1793.

Grguras, I., Maier, A. R., Behrens, C., Mazza, T., Kelly, T. J., Radcliffe, P., et al. (2012). Ultrafast X-ray pulse characterization at free-electron lasers. *Nature Photonics, 6*, 852–857.

Hastings, J. B., Rudakov, F. M., Dowell, D. H., Schmerge, J. F., Cardoza, J. D., Castro, J. M., et al. (2006). Ultrafast time-resolved electron diffraction with megavolt electron beams. *Applied Physics Letters, 89*, 184109.

Kim, K.-J. (1989). RF and space-charge effects in laser-driven RF electron guns. *Nuclear Instruments and Methods in Physics Research Section A: Accelerators, Spectrometers, Detectors and Associated Equipment, 275*, 201–218.

Li, R. K., & Musumeci, P. (2014). Single-shot MeV transmission electron microscopy with picosecond temporal resolution. *Physical Review Applied, 2*, 024003.

Li, R. K., Roberts, K. G., Scoby, C. M., To, H., & Musumeci, P. (2012). Nanometer emittance ultralow charge beams from RF photoinjectors. *Physical Review Special Topics—Accelerators and Beams, 15*, 090702.

Limborg, C., Li, Z., Xiao, L., Schmerge, J. F., Dowell, D., Gierman, S., et al. (2005). RF design of the LCLS gun. *LCLS-TN-05-3*.

Luiten, O. J., Claessens, B. J., van der Geer, S. B., Reunders, M. P., Taban, G., & Vredenbregt, E. J. D. (2007). Ultracold electron sources. *International Journal of Modern Physics A, 22*, 3882–3897.

Marsh, R. A., Albert, F., Anderson, S. G., Beer, G., Chu, T. S., Cross, R. R., et al. (2012). Modeling and design of an X-band RF photoinjector. *Physical Review Special Topics—Accelerators and Beams, 15*, 102001.

Rosenzweig, J., & Colby, E. (1995). Charge and wavelength scaling of RF photoinjector designs. In P. Schoessow (Ed.), *Advanced accelerator concepts: Fontana, WI 1994 (AIP Conference Proceedings 335)* (pp. 724–737). Woodbury, New York: American Institute of Physics Press.

Serafini, L., & Rosenzweig, J. B. (1997). Envelope analysis of intense relativistic quasilaminar beams in RF photoinjectors: mA theory of emittance compensation. *Physical Review E, 55*, 7565–7590.

Sun, Y., Adolphsen, C., Limborg-Deprey, C., Raubenheimer, T., & Wu, J. (2012). Low-charge, hard x-ray free electron laser driven with an X-band injector and accelerator. *Physical Review Special Topics—Accelerators and Beams, 15*, 030703.

van der Geer, S. B., & de Loos, M. J. (n.d.). General Particle Tracer. http://www.pulsar.nl/.

van Oudheusden, T., Pasmans, P. L. E. M., van der Geer, S. B., de Loos, M. J., van der Wiel, M. J., & Luiten, O. J. (2010). Compression of subrelativistic space–charge-dominated electron bunches for single-shot femtosecond electron diffraction. *Physical Review Letters, 105*, 264801.

Vlieks, A. E. X-band RF gun development. *SLAC-PUB-15107*. http://www.slac.stanford.edu/cgi-wrap/getdoc/slac-pub-15107.pdf.

Vlieks, A. E., Akre, R., Caryotakis, G., DeStefano, C., Frederick, W. J., Heritage, J. P., et al. (2006). Recent measurements and plans for the SLAC Compton X-ray source. SLACPUB-11689, 10pp. Published in *AIP Conference Proceedings*, 807, 481–490. http://scitation.aip.org/content/aip/proceeding/aipcp/807.

Zolotorev, M., Commins, E. D., & Sannibale, F. (2007). Proposal for a quantum–degenerate electron source. *Physical Review Letters, 98*, 184801.

Cool Beams for Ultrafast Electron Imaging

O.J. Luiten, M.W. van Mourik, W.J. Engelen, E.J.D. Vredenbregt
Eindhoven University of Technology, Eindhoven, The Netherlands

We have developed a new class of electron source that is based on near-threshold, pulsed photoionization of laser-cooled, trapped rubidium atoms. This allows us to produce intense picosecond electron pulses with large intrinsic coherence length. The ultralow source temperature—three orders of magnitude lower than conventional sources—seems to be in contradiction with the spread in photon energy associated with femtosecond ionization laser pulses. We explain this surprising result by a detailed study of the electron trajectories during photoionization. In addition, we show how laser polarization effects arise and that these can be used to further control the electron beam properties. Recently, we have produced the first diffraction patterns from graphite samples, which show that ultrafast nano-diffraction of solid-state systems is possible with this new source. Our goal is to demonstrate single-shot electron diffraction of macromolecules and thus enable dynamical studies of biomolecules in an ambient environment.

Multi-GeV Electron Radiography for MaRIE

F.E. Merrill, K.N. Borozdin, R.W. Garnett, F.G. Mariam, C.L. Morris,
A. Saunders, P.L. Walstrom
Los Alamos National Laboratory, New Mexico, USA

Charged particle radiography was first investigated in the late 1960s when high-energy proton accelerators (>100 MeV) provided the first charged particle probes capable of penetrating relatively thick objects. Because of the image degradation that results from scattering processes within the object, this technique was abandoned by the community. In the mid 1990s, however, Los Alamos National Laboratory developed a magnetic lens imaging technique that has enabled proton radiography for a wide range of applications. Today, there are four proton radiography facilities operating in the world and two additional facilities are being designed or fabricated. More recently, the technique of charged particle radiography has been extended to utilize high-energy electron probes (demonstrated with 30 MeV electrons) and Los Alamos National Laboratory is developing this technique for applications at the future Materials and Radiation in the Extremes (MaRIE) facility with multi-GeV electrons. The goal for this application is to measure fast dynamic materials properties with spatial resolution of less than 1 micron and temporal resolution of less than 1 ps. Through the collection of radiographic movies of dynamic processes a detailed understanding of dynamic materials can be gained. In this presentation, we will describe this method of charged particle radiography, present some examples of proton and electron radiographic measurements, and summarize our predictions for the performance of a 12-GeV electron radiography facility.

Multiscale Modeling of the Ultrafast Electron Microscope: From the Photocathode to the Sample

J. Portman, H. Zhang, K. Makino, C.-Y. Ruan, M. Berz, P.M. Duxbury
Michigan State University, Michigan, USA

Abstract

By modeling the photoemission process of high-brightness electron beams, we investigate the role of laser fluence and extraction field, as well as virtual cathode physics and the limits to spatiotemporal and spectroscopic resolution originating from the aspect ratio of the exciting laser pulse. We also provide a comparison of our model with experimental images of the photoemission process. We then present our development of a design for the ultrafast electron microscope (UEM) column using the analytic Gaussian model and calculate the achievable temporal and spatial resolutions under different photoemission conditions.

Keywords: Ultrafast electron microscope (UEM), photoemission, analytic Gaussian model

1. INTRODUCTION

The invention and spread of commercially available femtosecond lasers has opened the door for the study of ultrafast nonequilibrium processes in materials, and this field has grown rapidly over the last decade. The term *ultrafast* generally indicates phenomena that take place on ns (10^{-9} s) or faster timescales and, correspondingly, on length scales between μm (10^{-6} m) and Å (10^{-10} m). This broad class spans the fields of biology (Zewail, 2010), material science from ultrafast phase transitions (Ruan et al., 2004) to charge transport at nanointerfaces (Ruan et al., 2009) and dynamics in correlated electron materials (Tao et al., 2012a), chemistry (Zewail, 2000; Nicodemus et al., 2011), and plasma physics (Hau-Riege et al., 2012).

In practice, these systems are best explored by using the well-known pump–probe technique: the sample under consideration is excited by the pump pulse, and its response at various delay times is measured with a probe pulse. By recording the response of the system as a function of delay time, we can obtain a description of its time evolution, provided that both the pump and the probe pulse have sufficient time resolution. While femtosecond lasers have become the tool of choice as pump pulses, the main candidates

for probing the structural response are X-rays and electrons (King et al., 2005; Carbone et al., 2012). X-rays offer angstrom-size wavelengths, high spatial coherence, and short pulse length, but their generation with a high-enough brightness requires large-scale facilities. Electron probes, on the other hand, are easily generated using tabletop scale equipment, inflict less damage on the sample than do X-rays, and have a high-scattering cross section. The drawback is that using a charged particle beam leads to defocusing due to the Coulomb repulsion. Understanding the extent to which this space charge broadening between the electrons can be compensated for by using magnetic lenses and RF cavities is still an open question (Tao et al., 2012; van Oudheusden et al., 2010; Li & Musumeci, 2014).

The focus of this paper is to present an overview of the theoretical work done to guide the development of the ultrafast electron microscope (UEM) system at Michigan State University. In the next section, the photoemission process of high-brightness electron beams is analyzed in detail and optimal pulse generation conditions are discussed, while section 3 focuses on incorporating these results into a mean field model describing the whole microscope column to provide estimates of the achievable resolution in the system for various photoemission conditions. Section 4 offers a brief conclusion.

2. GENERATION OF THE ELECTRON PULSE

The initial photoemission stage is critical for the operation of the UEM as the phase space volume occupied by the pulse sets limits on the achievable temporal and spatial resolutions and depends on the extraction conditions and the initial Coulomb expansion. For this reason, it is necessary to min-imize the increase in beam emittance due to space charge effects while maintaining a high number of electrons. Another issue to take into account is the so called virtual cathode (VC) limit, in which the negative charge of the electrons emitted at earlier times, combined with the attractive surface field, hinders further emission of particles and causes a degradation of the pulse properties. To better understand the nonlinear interplay between the space charge driven expansion, laser properties, photocathode material properties, and virtual cathode physics, we have conducted explicit N-particle simulations of the electron photoemission process using COSY INFINITY, a code designed for high-performance scientific computing and beam dynamics simulations (Makino & Berz, 2006).

The electron bunch is generated through photoemission from a gold photocathode irradiated with a laser pulse. This process can be described using the so-called three-step photoemission model (Berglund & Spicer, 1964; Dowell & Schmerge, 2009) in which each electron is emitted independently as a result of absorbing a photon of energy $\hbar\omega$, diffusing to the surface and escaping to the vacuum. The initial velocities are calculated taking into account that in order to escape the photocathode, the electrons need to overcome the work function of the material. Taking z as the direction perpendicular to the photocathode surface, the following equations result for the initial velocities:

$$v_{x\,out} = v\sin\theta\cos\phi, \tag{1}$$

$$v_{y\,out} = v\sin\theta\sin\phi, \tag{2}$$

$$v_{z\,out} = \sqrt{(v\cos\theta)^2 - 2(E_F + W)/m_0}, \tag{3}$$

where $v = \sqrt{\frac{2(E_i + \hbar\omega)}{m_0}}$, E_i is the randomly generated initial energy of the electron, E_F is the photocathode Fermi energy, W is its work function, m_0 is the electron rest mass, and $\hbar\omega$ is the laser pulse energy. $\theta \in [0, \theta_{max}]$ and $\phi \in [0, 2\pi]$. θ_{max} is the maximum angle for which the electron can escape with sufficient velocity in the z direction and is given by

$$\cos\theta_{max} = \frac{v_{z\,min}}{v} = \sqrt{\frac{E_F + W}{E_i + \hbar\omega}}. \tag{4}$$

The initial coordinates in directions parallel to the surface (x, y in our notation) are randomly generated given the spatial profile of the laser pulse, and the initial z coordinate is set equal to zero. The time evolution of the emitted electrons is treated by solving their relativistic equations of motion at each time step using a fourth-order Runge-Kutta algorithm. The particles that fall back on the surface ($z < 0$) are removed from the simulation and collisions between electrons are avoided by imposing a maximum force cutoff. The Coulomb forces felt by the electrons are treated through a multiple-level fast multipole method (MLFMM) (Zhang & Berz, 2011; Zhang, 2013), and we use macroparticles to further reduce the computational time and allow simulations with higher numbers of electrons. A more in-depth description of the MLFMM can also be found in Zhang et al. (2015). In addition to the external extraction field F_a, we include the effect of the image charge field generated by the electrons on the cathode surface. Further

details on our implementation can be found in Portman et al. (2013, 2014) and Portman (2014).

Comparing the time-dependent longitudinal density profiles of photoemitted electron bunches extracted from shadow imaging experiments [Figure 1(A), circles at 50 and 80 ps] (Tao et al., 2012) with the simulations under the same conditions (red lines), we observe excellent agreement for the description of the front of the beam. The shaded regions in the figure indicate portions of the beam close to the surface where the charge density is not fully accessible experimentally due to strong surface scattering of the probe beam. Overall, our model accurately captures the propagation of the pulse over tens of picoseconds, indicating that the relevant physics of the process is correctly described.

Experimental data on the longitudinal pulse width σ_z indicated a universal sublinear scaling with the number of electrons N_e^{emit} [Figure 1(B)]. Our simulations show that this is somewhat accidental as it is a result of the linear growth of σ_z in the sub–virtual cathode regime at low values of N_e^{emit} combined with its reduced increase as the VC regime sets in.

In order to use the generated electron bunch for single-shot imaging or diffraction, we require between 10^5 and 10^9 electrons per pulse, so another key quantity of interest is the final number of electrons at the end of the photoemission process. This is shown in Figure 1(C) as a function of the initial number of electrons, N_e^0 for varying extraction fields F_a. For a low number of generated electrons ($N_e < 10^6$), all of the particles escape the surface, creating the linear relationship seen in the first part of the figure. As the initial number of electrons is increased, the space charge effect also increases due to both the electrons and the image charge on the surface until the VC limit is reached.

Increasing the extraction field shifts the onset of this phenomenon, enabling the emission of a higher number of particles from the photocathode. The critical value of extracted charge corresponding to the onset of the VC is plotted in the inset of Figure 1(C) as a function of extraction field F_a, with the dashed line indicating a fit to the analytical model presented in Valfells et al. (2002). This model approximates the pulse as a sheet of charge to derive an equation for the critical charge density in the transverse direction [see Eqs. (3) and (7) in Valfells et al. (2002)]: $\rho_{q,crit} = N_e^{crit}/\left(\pi\sigma_r^2\right) = \epsilon_0 F_a$, where σ_r is the width of the pulse and ϵ_0 is the dielectric permittivity.

To better understand the microscopic dynamics leading to virtual cathode formation, we present snapshots of the time evolution of the pulse in the x-z plane in Figure 2 through a color map of the charge distribution of the
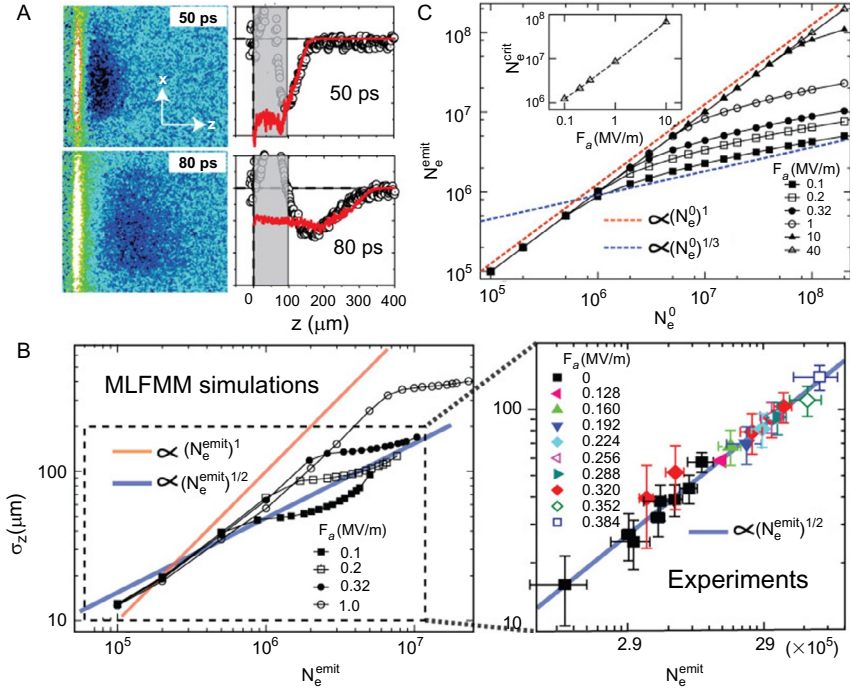
Figure 1 (A) Comparisons of MLFMM simulations of longitudinal charge density profiles (red lines) and data (circles) extracted from the shadow imaging experiments at 50 and 80 ps. (B) Sublinear scaling of longitudinal bunch size σ_z versus number of electrons emitted (N_e^{emit}) taken at 120 ps from MLFMM simulations (left panel), and compared to the shadow imaging data (right panel). (C) N_e^{emit} versus the number of generated electrons (N_e^0) for various extraction fields (F_a), showing evidence of virtual cathode formation. Inset: Threshold number of electrons (N_e^{crit}) for virtual cathode formation as a function of F_a (*Reprinted with permission from Portman et al., 2013; Copyright 2013, AIP Publishing LLC.*).

bunch overlaid with arrows representing the average electron velocity. Also shown are projections of the density onto the *x*- and *z*-axes. For short time-scales, the spatial profile of the pulse retains the Gaussian distribution of the generating laser pulse [Figure 2(A)]. The velocities show a turbulent flow related to the initial thermal distribution from which they were generated and independent of extraction field. At later times, the pulse begins to move away from the surface, and for conditions below the virtual cathode limit, the flow becomes fully laminar [Figure 2(B)]. The pulse evolves into the typical pancake shape, with an ellipsoidal transverse profile and a sharp peak corresponding to the center of the pancake in the longitudinal direction. On the other hand, above the VC limit [Figure 2(C)], the pulse retains some
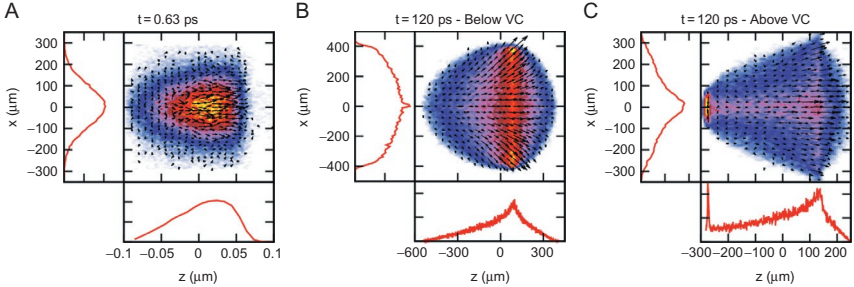
Figure 2 Color map of the charge distribution in the rest frame of the bunch projected onto the x-z plane, overlaid with arrows representing the average electron velocity and projected onto the x- and z-axes. (A) Initial stage of photoemission, which is independent of extraction field. (B), (C) Final stage at $t = 120$ ps for conditions below and above the virtual cathode limit for $N_e^0 = 7 \cdot 10^6$ and extraction fields $F_a = 10$MV/m and $F_a = 0.32$MV/m, respectively.

turbulent flow and does not fully detach from the surface. In the transverse direction, it presents a superposition of ellipsoidal and Gaussian components, while in the longitudinal (z) direction, we observe a peak in the density for values of z close to the surface, which is a typical signature of the virtual cathode limit.

To compare different regimes of pulse generation and find optimal photoemission conditions, both the transverse and longitudinal emittances are of importance as they determine, respectively, the spatial and temporal resolutions achievable. Ideal pulse generation conditions would minimize both the longitudinal (z) and transverse (x) normalized emittances, defined as (Luiten et al., 2004)

$$\epsilon_x = \frac{1}{m_0 c} \sqrt{\langle x^2 \rangle \langle p_x^2 \rangle - \langle x p_x \rangle^2}. \tag{5}$$

It is worth noting here that the quantity ϵ_x defined in Eq. (5) is a statistical approximation of the true 6D emittance, and it assumes that there is little correlation between the x-, y- and z-directions so that the dynamics decouples into three independent 2D cases. We calculate this quantity and parameters derived from it, as traditionally the emittance has been used as a key figure of merit for UEM systems since it provides an easily accessible estimate of the phase space occupied by the pulse (Portman et al., 2013).

When comparing different photoemission conditions, it is also necessary to take into account the aspect ratio of the laser pulse. Our discussion so far has presented results relative to the so-called pancake regime, characterized

by a laser pulse in which the transverse width is greater than the longitudinal one ($\sigma_r \gg \sigma_z$). The cigar regime on the other hand is characterized by an elongated pulse in which $\sigma_z \gg \sigma_r$, and this has been suggested (Filippetto et al., 2014) as a promising choice to improve the extraction efficiency by shifting the onset of the VC at the expense of the temporal resolution.

As shown in Figure 3(A), varying the aspect ratio of the exciting laser pulse from pancake to cigar-like leads to a decrease in the transverse emittance at the expense of an increase in the longitudinal component. Extraction of pulses with a higher charge causes a strong increase in the longitudinal (transverse) emittance for the pancake- (cigar-) shaped pulses, respectively. This can be compensated to some extent by increasing the extraction field F_a. From this, we conclude that for applications requiring both temporal and spatial resolutions, a pancake-like pulse may be more appropriate. On the other hand, if time resolution is not essential and a higher longitudinal emittance is acceptable, one can obtain increased spatial resolution by using an elongated, cigar-like photoemitting laser pulse.

In addition to the emittance, our ability to resolve spatial features can be quantified with the coherence length L_c, which at the beam waist can be expressed as (van Oudheusden et al., 2007)

$$L_c = \frac{h}{2m_0 c} \frac{\sigma_r}{\epsilon_x},\qquad(6)$$

where, as discussed previously, we have assumed that the transverse and longitudinal directions are decoupled, h is Plank's constant, m_0 is the rest
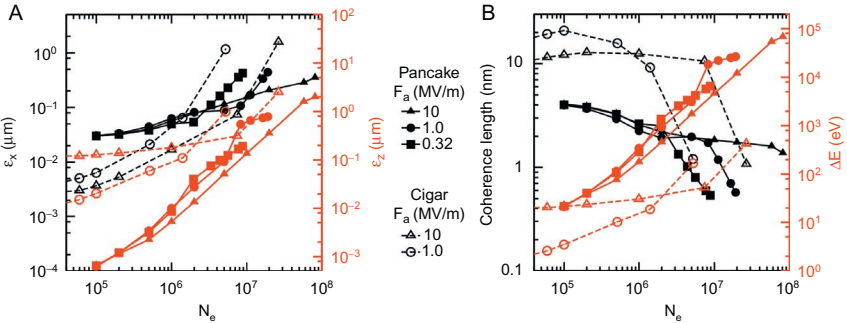
Figure 3 Comparison between pancake-like and cigar-like pulses for increasing values of extraction field F_a and number of electrons in the pulse: (A) transverse (black) and longitudinal emittance (red) and (B) coherence length (black) and energy spread ΔE (red).

mass of the electron, c is the speed of light, σ_r is the beam radius, and ϵ_x is the normalized transverse emittance.

The energy spread, defined as (Portman et al., 2013)

$$\Delta E = \frac{\epsilon_z}{\Delta t} m_0 c, \tag{7}$$

where ϵ_z is the normalized longitudinal emittance and Δt is the temporal resolution, is also a key quantity that should be minimized for optimal operation.

To conclude our discussion, we compare the coherence length and the energy spread for pancake-like and cigar-like pulses in Figure 3(B). The cigar-like pulse presents significantly better coherence length and lower energy spread compared to the pancake-like pulses until the VC limit is reached. As the number of electrons is increased to above the VC, the cigar shape shows a very sharp decrease of the coherence length. In contrast, while the pancake-like pulses display lower coherence lengths and higher energy spreads overall, their dependence on the number of electrons is less critical. Increasing the extraction field F_a significantly increases the energy spread of the cigar-like case while the pancake is unaffected.

3. BUILDING THE ELECTRON MICROSCOPE

During the photoemission process discussed so far, nonlinear effects play a key role in determining the pulse properties. In the first 100 ps, the pulse rapidly expands as a result of the repulsive stochastic Coulomb forces. After this initial stage, the charge density is sufficiently low that a mean field model can be used to describe the dynamics of the electrons inside the microscope. To do so, we adapt the so-called analytic Gaussian model introduced by Michalik and Sipe (2006) and refined by Berger and Schroeder (2010), to be applicable to the UEM system (Portman 2014).

In the analytic Gaussian model, the electron bunch is modeled with a product of Gaussian distributions in both momentum and position:

$$f(\mathbf{r}, \mathbf{p}; t) = C f_T(x, y, p_x, p_y; t) f_z(z, p_z; t), \tag{8}$$

where

$$f_T(x, y, p_x, p_y; t) = \exp\left[-\frac{x^2 + y^2}{2\sigma_T} - \frac{[p_x - (\gamma_T/\sigma_T)x]^2 + [p_y - (\gamma_T/\sigma_T)y]^2}{2\eta_T} \right], \tag{9}$$

$$f_z(z, p_z; t) = \exp\left[-\frac{z^2}{2\sigma_z} - \frac{[p_z - (\gamma_z/\sigma_z)z]^2}{2\eta_z}\right]. \tag{10}$$

Here, $\sigma_{T,z}$, $\eta_{T,z}$, and $\gamma_{T,z}$ are time-dependent parameters that describe, respectively, the spatial width, kinetic energy spread, and chirp of the electron pulse (Figure 4). Equations of motion are derived for these parameters using a mean-field self-similar approximation. By treating the effect of the various optical elements on the pulse properties, we build a model for the UEM that includes the photoemission gun, magnetic lenses, and RF cavity. The strengths of the lenses and of the electric field in the RF cavity were used as variables in an optimization routine to control the position and spot size of the beam waist. The initial pulse parameters (number of electrons, center of mass velocity and analytic Gaussian parameters) were extracted from the simulations of the photoemission process discussed in the previous section. The emittance is a conserved quantity in this model and its value is also determined from the initial photoemission conditions. For this reason, in simulating the microscope design, we will focus on the optimal achievable bunch size for given photoemission conditions.

Results for the column optimized for $N_e = 10^6$ electrons generated with a pancake-like laser pulse and a kinetic energy of 100 keV are shown in Figure 5, where we plot the longitudinal and transverse bunch sizes as a function of position along the microscope. The beam waist is at $\sim$1090 mm, with pulse size 0.92 μm in the transverse and 2.3 μm in the longitudinal direction. Due to the strength of the lens used to focus the pulse, for positions close to the
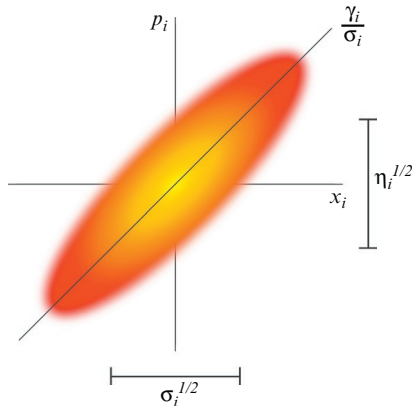
Figure 4 Schematic representation of the pulse parameters used in the analytic Gaussian model in phase space.
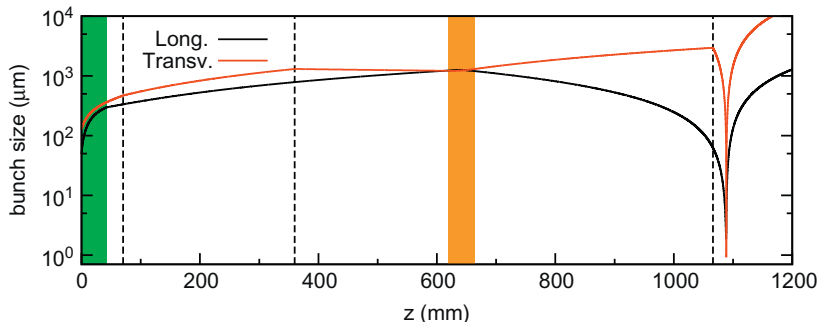
Figure 5 Transverse and longitudinal bunch sizes as a function of position along the column of the UEM. The region corresponding to the photoemission gun is shown in green, while that corresponding to the RF cavity is in yellow. The dashed lines correspond to the magnetic lenses. The electron beam is composed of $N_e = 10^6$ electrons with a kinetic energy of 100 keV emitted with a pancake-like laser pulse with an initial transverse width of 100 μm and a temporal duration of 50 fs.

Table 1 Pulse parameters at the beam waist for a 100-keV electron bunch with varying number of electrons N_e

	Transverse Size (μm)	Transverse emitt. (nm)	Bunch Length (fs)	Energy Spread ($\times\ 10^{-4}$)
$N_e = 10^5$ Pancake	0.98	27	13	3.7
$N_e = 10^6$ Pancake	0.92	75	40	9.3
$N_e = 10^7$ Pancake	0.94	210	290	24
$N_e = 10^6$ Cigar	0.14	21	420	17
Goal: $N_e > 10^6$	~1–10	<20	<100	<10

The pancake-like pulses are generated with a 50-fs laser beam with a transverse width of 100 μm; for the cigar-like pulse, we used a 10-ps laser with a transverse spot size of 10 μm. The reported goal parameters are taken from (van Oudheusden et al., 2007, Berger et al., 2009, van der Geer et al., 2009, Tao et al., 2012).

beam waist, the transverse width diverges rapidly so that accurate positioning of the sample at the beam waist is crucial for good spatial resolution. The divergence of the longitudinal component is less severe.

We perform similar optimizations varying the number of electrons in the pulse and summarize our results in Table 1. The transverse pulse sizes are comparable for all the simulations reported, which is in part due to the lack

of aberrations in the analytic Gaussian model, which would play a role as the width of the pulse is increased. Also not included in the model are stochastic space charge effects, which would lead to an additional broadening of the pulse at the beam waist due to electron–electron repulsion. In any case, the transverse size obtained is well within our requirements for UEM systems. As pointed out in the previous section, spatial resolution also depends on the transverse emittance, and our data for the UEM column confirms the results of our photoemission simulations (namely, that the cigar-shaped pulse offers a lower emittance than the pancake pulse). Shaping the radial profile of the photoemitting laser pulse to generate an ellipsoidal electron bunch allows to reduce the emittance by a factor of 2, bringing the emittance of the pancake-like pulses within our target range as well.

For time-resolved applications, both the bunch length and energy spread are critical parameters. For pancake-like pulses, the bunch length (calculated from the longitudinal size as $\delta t = 2\sqrt{2\sigma_z}/v_0$) is increased from $\delta t = 13$ fs for the 10^5 electron pulse to $\delta t = 290$ fs for the pulse with 10^7 electrons. The energy spread also increases similarly with the pulse charge. For $N_e = 10^6$, these parameters are already within our target range, and further improvement can be obtained by switching to ellipsoidal bunches. On the other hand, while the cigar-like pulse offers good spatial resolution, it is not easily used for time-resolved measurements, as longitudinal focusing to the sizes needed can be challenging due to the length of the pulse.

4. CONCLUSIONS

We have presented our model for simulating the time-dependent evolution of a photoemitted electron pulse and show good agreement with experimental results obtained using the shadow imaging technique. At short timescales, the spatial profile of the emitted electron pulse depends on the laser used to generate it, and the distribution of velocities is indicative of a turbulent flow related to the initial thermal distribution and independent of extraction field, as observed in Figure 2(A). At later times, as the pulse moves away from the surface, its properties display a strong dependence on the extraction conditions: Below the virtual cathode limit, the pulse becomes fully laminar, evolving into the typical ellipsoidal shape, while above the virtual cathode, some turbulent flow is present and the pulse does not fully detach from the surface.

Our investigation of the optimal conditions for pulse generation in terms of laser fluence and extraction field F_a for different experimental realizations

shows evidence of virtual cathode formation as the initial number of electrons is increased as a consequence of space charge effects. We also vary the aspect ratio of the photoemitting laser pulse and show how the emittance, coherence length, and energy spread depend on the number of electrons needed in a single pulse and on the extraction field. Based on the desired resolution, it is possible to find the optimal conditions of pulse generation.

Given these photoemission conditions, we also derive a mean–field formalism to simulate the propagation of an electron pulse through a microscope column. We include a description of the photoemission gun, magnetic lenses, and an RF cavity in our model for the UEM system and give quantitative predictions of the achievable spatial and temporal resolutions both for pancake-like and cigar-like electron pulses. Given the limitations of the analytic Gaussian model, these predictions should be viewed as best-case results since aberrations and deviations of the pulse from the assumed self similar Gaussian profile were neglected. Nevertheless, due to the simplicity of the model and the resulting ease of computation, we believe that our model can offer a valuable tool in understanding the achievable resolution in UEM systems and allow one to search for optimal configurations over a vast range of parameters.

ACKNOWLEDGMENTS

REFERENCES

Berger, J. A., Hogan, J. T., Greco, M. J., Schroeder, W. A., Nicholls, A. W., & Browning, N. D. (2009). DC photoelectron gun parameters for ultrafast electron microscopy. *Microscopy and Microanalysis, 15*, 298–313.

Berger, J. A., & Schroeder, W. A. (2010). Semianalytic model of electron pulse propagation: Magnetic lenses and RF pulse compression cavities. *Journal of Applied Physics, 108*, 124905.

Berglund, C. N., & Spicer, W. E. (1964). Photoemission studies of copper and silver: Theory. *Physical Review, 136*, A1030–A1044.

Carbone, F., Musumeci, P., Luiten, O., & Hebert, C. (2012). A perspective on novel sources of ultrashort electron and x-ray pulses. *Chemical Physics, 392*, 1–9.

Dowell, D. H., & Schmerge, J. F. (2009). Quantum efficiency and thermal emittance of metal photocathodes. *Physical Review Special Topics—Accelerators and Beams, 12*, 074201.

Filippetto, D., Musumeci, P., Zolotorev, M., & Stupakov, G. (2014). Maximum current density and beam brightness achievable by laser-driven electron sources. *Physical Review Special Topics—Accelerators and Beams, 17*, 024201.

Hau-Riege, S. P., Graf, A., Doeppner, T., London, R. A., Krzywinski, J., Fortmann, C., et al. (2012). Ultrafast transitions from solid to liquid and plasma states of graphite induced by x-ray free-electron laser pulses. *Physical Review Letters, 108*, 217402.

King, W. E., Campbell, G. H., Frank, A., Reed, B., Schmerge, J. F., Siwick, B. J., et al. (2005). Ultrafast electron microscopy in materials science, biology, and chemistry. *Journal of Applied Physics, 97*, 111101.

Li, R. K., & Musumeci, P. (2014). Single-shot MeV transmission electron microscopy with picosecond temporal resolution. *Physical Review Applied 2*, 024003.

Luiten, O., van der Geer, S., de Loos, M., Kiewiet, F., & van der Wiel, M. (2004). How to realize uniform three-dimensional ellipsoidal electron bunches. *Physical Review Letters, 93*.

Makino, K., & Berz, M. (2006). COSY INFINITY version 9. *Nuclear Instruments and Methods in Physics Research Section A, 558*, 346–350.

Michalik, A. M., & Sipe, J. E. (2006). Analytic model of electron pulse propagation in ultrafast electron diffraction experiments. *Journal of Applied Physics, 99*, 054908.

Nicodemus, R. A., Corcelli, S. A., Skinner, J. L., & Tokmakoff, A. (2011). Collective hydrogen bond reorganization in water studied with temperature-dependent ultrafast infrared spectroscopy. *Journal of Physical Chemistry B, 115*(18), 5604–5616.

Portman, J. (2014). Ultrafast science: A multiscale modeling approach to femtosecond electron diffraction and its applications. Ph.D. thesis, Michigan State University, East Lansing.

Portman, J., Zhang, H., Makino, K., Ruan, C.-Y., Berz, M., & Duxbury, P. M. (2014). Untangling the contributions of image charge and laser profile for optimal photoemission of high-brightness electron beams. *Journal of Applied Physics, 116*, 174302.

Portman, J., Zhang, H., Tao, Z., Makino, K., Berz, M., Duxbury, P. M., & Ruan, C.-Y. (2013). Computational and experimental characterization of high-brightness beams for femtosecond electron imaging and spectroscopy. *Applied Physics Letters, 103*, 253115.

Ruan, C.-Y., Murooka, Y., Raman, R. K., Murdick, R. A., Worhatch, R. J., & Pell, A. (2009). The development and applications of ultrafast electron nanocrystallography. *Microscopy and Microanalysis, 15*(4), 323–337.

Ruan, C.-Y., Vigliotti, F., Lobastov, V. A., Chen, S., & Zewail, A. H. (2004). Ultrafast electron crystallography: Transient structures of molecules, surfaces, and phase transitions. *Proceedings of the National Academy of Sciences USA, 101*(5), 1123–1128.

Tao, Z., Han, T., Mahanti, S., Duxbury, P., Yuan, F., Ruan, C.-Y., et al. (2012a). Decoupling of structural and electronic phase transitions in VO_2. *Physical Review Letters, 109*, 166406.

Tao, Z., Zhang, H., Duxbury, P. M., Berz, M., & Ruan, C.-Y. (2012). Space charge effects in ultrafast electron diffraction and imaging. *Journal of Applied Physics, 111*(4), 044316.

Valfells, A., Feldman, D. W., Virgo, M., O'Shea, P. G., & Lau, Y. Y. (2002). Effects of pulse-length and emitter area on virtual cathode formation in electron guns. *Physics of Plasmas, 9*, 2377–2382.

van der Geer, S., de Loos, M., Vredenbregt, E., & Luiten, O. (2009). Ultracold electron source for single-shot, ultrafast electron diffraction. *Microscopy and Microanalysis, 15*, 282–289.

van Oudheusden, T., de Jong, E. F., van der Geer, S. B., Root, W. P. E. M. O., Luiten, O. J., & Siwick, B. J. (2007). Electron source concept for single-shot sub-100-fs electron diffraction in the 100-keV range. *Journal of Applied Physics, 102*, 093501.

van Oudheusden, T., Pasmans, P. L. E. M., van der Geer, S. B., de Loos, M. J., van der Wiel, M. J., & Luiten, O. J. (2010). Compression of subrelativistic space-charge-dominated electron bunches for single-shot femtosecond electron diffraction. *Physical Review Letters, 105*, 264801.

Zewail, A. H. (2000). Femtochemistry: Atomic-scale dynamics of the chemical bond. *Journal of Physical Chemistry A, 104*, 5660–5694.

Zewail, A. H. (2010). Four-dimensional electron microscopy. *Science, 328*(5975), 187–193.

Zhang, H. (2013). The fast multipole method in the differential algebra framework for the calculation of 3D space charge fields. Ph.D thesis, Michigan State University, East Lansing.

Zhang, H., & Berz, M. (2011). The fast multipole method in the differential algebra framework. *Nuclear Instruments and Methods in Physics Research Section A, 645*, 338–344.

Zhang, H., Tao, Z., Ruan, C.-Y., & Berz, M. (2015). Space charge simulations of photoemission using the differential algebra-based multiple-level fast multipole algorithm. In *Proceedings of the Conference on Femtosecond Electron Imaging and Spectroscopy, FEIS 2013*. 56–66.

Design of Ultrafast Spin-Polarized Low-Energy Electron Microscopy

W.-X. Tang[1,3], W. Wan[1,2], L. Yu[1], X. Yang[1], S. Wu[1], J. Feng[1,2]
[1]Chongqing University, Chongqing, China
[2]Lawrence Berkeley National Laboratory, California, USA
[3]Monash University, Melbourne, Australia

With the support of Chongqing University, we have procured a state-of-the-art aberration-corrected LEEM/PEEM with high-temperature scanning tunneling microscopy from SPECS. A spatial resolution of 1.7 nm has been achieved in LEEM mode during on-site commissioning in Germany. The main feature of this microscope is that it contains three magnetic prism arrays (MPAs), as oppose to two in their standard configuration, allowing the possibility of adding a second electron gun to the system to achieve spin-polarized LEEM (SPLEEM). With an aberration corrector, the electron transmission flux of AC-SPLEEM is around one order of magnitude higher than the non-AC case, which is critical for developing time-resolved SPLEEM. Therefore, we are currently developing an ultrafast spin-polarized electron gun, ultrafast laser system, and electronics with the support of the National Science Foundation of China (NSFC). Together with the necessary optics, the future electron gun will realize time-resolved aberration-corrected spin-polarized LEEM (TR–AC–SPLEEM) mode at a time resolution of ps. We will report the concept of our electron optical design of the ultrafast spin-polarized electron gun and the whole column leading to the AC-TR-SPLEEM for low-dimensional spin dynamics and ultrafast surface dynamics research.

Environmental Scanning Electron Microscopy: Probing Ultrafast Solvation Dynamics at Interfaces

D.-S. Yang
University of Houston, Texas, USA

Probing interfacial dynamics and heterogeneous catalysis at the nanoscale requires experimental methods that incorporate simultaneous resolutions in both space and time into environmental techniques. However, dynamics investigations of such surface-molecule structures are limited in time resolution, being controlled by the video camera rate of recording at sub-milliseconds. In this talk, I will describe our development of environmental scanning ultrafast electron microscopy, whose orders-of-magnitude improvement in temporal resolution allows in situ detection of solid–gas interaction dynamics at materials surfaces. Using CdSe surfaces as a prototype, we investigated the spatiotemporal characteristics of solvation (by water, ammonia, and acetonitrile) in the recorded images. The ultrafast reorganization and relaxation dynamics of polar molecules in the adsorbate layers, observed on different crystalline surfaces, are striking in their temporal behavior and in the dependence on the surface structure, (0001) versus (101 bar0)/(112 bar0). The present development paves the way to other applications; e.g., those involving charge flow on heterogeneous surfaces and particles, catalysis, and hydration of biological systems.

ACKNOWLEDGMENTS